SEISMIC PERFORMANCE OF SELF-CENTERING FRAMES COMPOSED OF PRECAST POST-TENSIONED CONCRETE ENCASED IN FRP TUBES

By

AHMAD ABDULKAREEM SAKER SHA'LAN

A thesis submitted in partial fulfillment of
the requirements for the degree of

MASTER OF SCIENCE IN CIVIL ENGINEERING

WASHINGTON STATE UNIVERSITY
Department of Civil Engineering

DECEMBER 2009

To the Faculty of Washington State University:

The members of the Committee appointed to examine the dissertation/thesis of AHMAD ABDULKAREEM SAKER SHA'LAN find it satisfactory and recommend that it be accepted.

_____
Mohamed ElGawady, Ph.D., Chair

_____
David McLean, Ph.D.

_____
David Pollock, Ph.D.

_____
William Cofer, Ph. D.

ACKNOWLEDGEMENT

I could not have finished this project without the support and contribution of many people to whom I am deeply thankful.

Initially and most importantly, I would like to thank my parents, Abdulkareem and Wafa', for their unconditional support at all times. You have always been there for me, and I would not have made it without your love, advice, patience, and financial support. Thank you for being the wonderful parents you are and I hope I will make you proud.

Also I would like to thank my brother Mohamed and my sisters Mona, Doa' and Wala' for their love and for continuously trying to call me and setting up internet calls with the family, which made it easier for me to stay all this long time away from you guys.

I would like to thank my committee, Dr. Mohamed ElGawady, Dr. David McLean, Dr. David Pollock, and Dr. William Cofer for providing me with an opportunity to come and learn at Washington State University and for their academic support throughout the time I spent working on this project; Dr. ElGawady for constantly pushing me to the best I could be, Dr. Pollock for being a great source of advice and practical solutions, Dr. Cofer for the important theoretical suggestions, and Dr. McLean for helping me making this project a better and a more professional one.

I would also like to thank the SEED Grant, Washington State University for providing support for this research.

I would like to thank the staff at the Civil Engineering department: Vicki Ruddick, Maureen Clausen, Glenda Rogers, Lola Gillespie, and Tom Weber for their help and support with various aspects throughout my work here at WSU. Also I would like to thank Robert

Duncan and Scott Lewis at the Wood Materials and Engineering Laboratory for helping and guiding me during my work at the lab, which was vital for this project.

I would like to thank the staff of the Graduate School at WSU for all their support. Special thanks to Dr. Debra Sellon who helped me through hard times and provided me with great support and advice. Your thoughts and wisdom made me see the bigger picture, and I deeply respect you.

I would like to thank my professors at the University of Jordan who helped me both academically and professionally and for believing in me: Dr. Abdullah Assaad, Dr. Raed Samra, Dr. Ghaleb Sweis, and Abdelqader Najmi. Special thanks to Dr. Abdulla Assaad for being the great mentor, teacher, and advisor whom I deeply respect. Thank you for your time both at Pullman and Amman, I really enjoyed the time we spent together.

I would like also to thank Robbie Giles at Owen Science and Engineering Library for all the help and for giving me a chance to help support myself financially by working at Fischer Agricultural Sciences Library which I adore working at. Also, I would like to thank Rhonda Gaylord for being a great person and for listening and offering advice throughout my time at AgSci Library. I would like also to thank Katherine Lovrich for giving me the chance to participate in the Peer-Tutoring program where I learned how to be a better teacher, to communicate better, and to have an extra source of financial support.

Last but not least, I would like to thank my Jordanian friends here at Pullman, the great students and workers who continue to prove to me that nothing is impossible. Dr. Hamza Qadiri, I started to like the area after you showed us around. Dr. Hala Abu Taleb, thank you for inviting us to your wonderful home and for the soup during Ramadan. Hamza Bardaweel for being my first friend here in Pullman, I hope you get your PhD very soon. Amer Al Halig for the great

friend you are. Amer Hamdan, you are a brother to me. Thank you for coming every time I needed you at the lab and for the wonderful time we spent here, and I hope your experiments succeed and you get your PhD very soon. Leen Kawas, thank you for being the great friend and neighbor, I consider you part of my family. Thank you for all your support; at the university, the lab, work, home, and all the great time we spent. I hope you succeed in your research and your academic career. I'm positive that you will make us all proud, and I'm looking forward to hearing about your success in your PhD research.

SEISMIC PERFORMANCE OF SELF-CENTERING FRAMES COMPOSED OF PRECAST POST-TENSIONED CONCRETE ENCASED IN FRP TUBES

Abstract

By Ahmad Adulkareem Saker Sha'lan, M.S.
Washington State University
December 2009

Chair: Mohamed ElGawady

This research studied the performance of continuous and segmented precast post-tensioned concrete columns confined by fiber reinforced polymer (FRP) tubes used to construct moment resisting frames that were 60 in. high and 82 in. wide. Four unbonded post-tensioned frames constructed using precast members were designed to re-center in the direction of the original position after lateral loading. The columns were 8 in. in diameter and 45 in. in clear height. The FRP columns were composed of either continuous 45 in. long segments or by stacking three 15 in. long segments on top of each other. A monolithic reinforced concrete moment resisting frame with similar dimensions of the FRP specimens designed according to the provisions of the American Concrete Institute Building Code Requirements for Structural Concrete was constructed as a control specimen. Key parameters were analyzed and compared such as hysteresis, damage, drift, and energy dissipation. SAP2000 was used to construct pushover models of the reinforced concrete specimen and one FRP specimen to predict load-drift response, which were about 95% accurate.

Three FRP specimens were constructed from segmented columns while one was constructed from continuous columns. Neoprene layers were added to the column-beam and

column-base interfaces of one segmented FRP specimen to dissipate energy, reduce damage to the structural members, and to lengthen the period of the frame. External sacrificial energy dissipating devices in the form of modified steel angles were attached to another segmented FRP specimen to dissipate energy when deforming plastically while allowing them to be replaced after testing.

The reinforced concrete specimen was the most damaged in the form of plastic hinge formation, cover spalling, core crushing, as well as rebar fracture. The FRP specimens suffered minor damage with the specimen with neoprene layers the least damaged. The FRP specimen with sacrificial energy dissipaters had the highest amount of energy dissipated followed by the reinforced concrete specimen. The FRP specimen with segmented columns dissipated more energy than the one with continuous columns, while the specimen with neoprene layers dissipated the least amount of energy. Post-tensioning bar yielding only occurred in the specimen with sacrificial energy dissipaters.

TABLE OF CONTENTS

Page

LIST OF TABLES

LIST OF FIGURES

Chapter 1

Introduction

1.1 Introduction and background

Due to increasing traffic flows and the high demand on bridges in transportation systems, methods have been developed to increase the speed of their construction. Construction of bridges with conventional cast-in-place reinforced concrete systems has several disadvantages. It requires a relatively long time for construction. Such time delays lead to traffic congestions. Also, it is highly susceptible to major structural damage after undergoing large seismic loads. Repairing the major structural elements of the bridge after seismic events is usually difficult if not impossible. In addition to that, conventional cast-in-place concrete construction poses negative environmental impacts on local surroundings of the bridge during construction especially for bridges spanning waterways.

As an alternative to the conventional cast-in-place concrete bridge system, a precast system may be used and has several advantages. Using precast components in bridges provides a faster method of construction. It is also favorable since it provides increased work-zone safety and reduces the environmental impacts of constructing bridges. Another advantage is the higher quality structural components of a precast system since they are manufactured in quality controlled plants.

Most applications of precast systems have been in areas of relatively low seismic potential. The behavior of such systems under seismic loading thus needs to be studied further. To improve their behavior under lateral loads, the strength capabilities of post-tensioned concrete columns comprising precast moment resisting frames may be enhanced by confining the columns with external jackets composed of various options of different materials. In this research, tubes composed of fiber reinforced polymers (FRP) were used to confine concrete columns that are parts of precast post-tensioned frames. This thesis presents the experimental results of a study of concrete moment resisting frames. Five 20% (1:5) scale frames consisting of circular columns and beams were tested. All frames had the same dimensions. One frame was designed according to the specifications of ACI 318-05 for special moment resisting frames as a control specimen for comparison with the other four frames.

The second frame consisted of precast concrete components. The columns included central unbonded post-tensioning strands. The third frame consisted of segmented precast column components. The fourth frame is similar to the third frame except it included additional steel angles fixed at corners of the bottom segments of the columns with the footings. The fifth frame included rubber padding between the interfaces of the segmental columns. Except for the frame designed according to ACI 318-05 provisions, no columns included any reinforcement, but were cast inside carbon fiber reinforced polymer (CFRP) composite tubes for shear strengthening and concrete confinement.

All specimens were subjected to pseudo-static, reverse-cyclic loading. The performance of the tested specimens was evaluated based on failure mode, measured displacement ductility, and hysteretic behavior.

1.2 Research objectives

This research was conducted to investigate the performance of bridge frames with post-tensioned concrete columns confined with FRP tubes while undergoing lateral loads and to compare their behavior to the conventional cast-in-place monolithic reinforced concrete bridge frames. The key objectives of this research are:

- Studying the structural characteristics and designing post-tensioned concrete columns confined with FRP tubes with improved strength capabilities when compared to similar sized conventional monolithic concrete columns.
- Evaluating the performance of frame systems with FRP confined columns undergoing lateral loading and comparing several key characteristics with those of a conventional monolithic reinforced concrete frame of similar dimensions.
- Investigating the effect of using multiple FRP-confined column-segments on the behavior of the post-tensioned frame system.
- Investigating the effect of adding energy dissipating mechanisms to the post-tensioned frame system with FRP confined columns and comparing its performance with that of the conventional monolithic reinforced concrete frame. Two methods of energy dissipation were investigated:
    i. Sacrificial modified steel angles attached to the columns.
    ii. Rubber sheets placed at column-beam and column-base interfaces.

- Investigate the control of damage of the structural members of several post-tensioned frame systems with FRP-confined columns undergoing lateral loading and comparing that with the conventional monolithic reinforced concrete frame and also offering the possibility of easy replacement of sacrificial members.

Chapter 2

Literature Review

2.1 Precast concrete components

Constructing bridges with cast-in-place concrete leads to several problems that include:

- Slow rate of construction which obstructs the flow of traffic.
- Relatively lower work-zone safety.
- The environmental impacts where bridges span waterways.

Precast concrete systems, which consist of components fabricated off-site and then connected on-site, offer a convenient method for rapid construction of bridges and hence are favorable over the traditional cast-in-place ones. In addition to that, the concrete components are fabricated in plants where better control environments are established, resulting in higher quality members.

Most applications of precast systems have been in areas of relatively low seismic potential. The behavior of such systems under seismic loading thus needs to be studied further. Several types of precast concrete systems for rapid construction of bridges were used in Washington State. Hieber et al. (2005) summarized the common ones used in non-seismic regions.

2.2 Ductile design

Seismic forces can cause structures to displace beyond their elastic range. Therefore, structural members need to possess adequate ductility to sustain an earthquake event as well as to prevent

brittle failures. According to the provisions of ACI318-05, ductility of reinforced concrete achieved by:

- Appropriate detailing of beam-column joints resulting in ductile connections.
- Applying sufficient transverse reinforcements to prevent shear failure (with the concept of strong shear and weak flexural strength), premature buckling of rebar under compression, or crushing of concrete under compression.
- Maintaining a weak beam – strong column flexural strength ratio preventing the relatively more brittle column failure as well as simultaneous formation of plastic hinges at the top and bottom of a column.

The structure is also required to dissipate seismic energy in order to be able to resist the lateral loading efficiently. Loading beyond the elastic range provides a means to dissipate energy as the members deform. However, such permanent deformations are considered disadvantages since they often require costly methods for repair.

2.3 Re-centering system and damage control

Residual drifts are also a matter of concern, and therefore methods have been developed to minimize that. An idea is to provide a re-centering force to the drifting column. Hieber et al. (2005) introduced a hybrid system; where unbonded prestressing strands, placed at the center of the column cross section, provide a re-centering force. The weight of the structure also works with the re-centering force. Using un-bonded steel strands distributes the additional stress induced by the lateral load over the whole length of the reinforcement, and hence prevents local

yielding. Mild steel reinforcement is provided at the joints of the hybrid column. Their main function is to dissipate energy as the steel yields.

Mander and Cheng (1997) proposed the concept of the control and repairability of damage (CARD) seismic paradigm. In this study, purposely weakened hinge zones are achieved by using machined-down longitudinal reinforcing steel effectively forming a so-called “fuse bar”. In this manner, all damage is focused within the sacrificial repairable hinge zone while all other portions of the structure remain elastic at all times.

Large deformations of the bridge pier must be prevented in order to stay functional after a seismic event. Under this philosophy, using steel reinforcement (as longitudinal bar reinforcement) is not favorable, since they are expected to yield and, hence, deform permanently.

As an alternative to the traditional ductile design philosophy, Mander and Cheng (1997) introduced a design approach of bridge piers based on damage avoidance design. In this design approach, energy is generally dissipated through mechanical dissipating devices such as lead cores within lead-rubber bearings, via friction in sliding bearings, or with special supplemental mechanical energy dissipating devices such as steel, viscous or visco-elastic dampers. In the design of bridge piers, the longitudinal column steel is made discontinuous at the beam-column interface, allowing column rocking. Energy is dissipated through radiation damping. Rocking piers dissipate considerable energy when each leg of the pier slams onto the foundation.

Sakai et al (2006) studied and compared the behavior of conventionally detailed columns with similar columns having various prestressing with the use of unbounded mild bars in some specimens. The results showed that the residual displacements of the proposed columns were about 10% of those of conventionally detailed columns, while the peak responses were almost identical.

Another idea can be implemented by using external steel members fixed at the base of the columns to the footings. The steel members are expected to dissipate seismic energy as they deform after yielding, decreasing the demand on the main structure. The steel members can then be replaced without obstructing the traffic flow. Chou and Chen (2006) applied the use of such a steel member as an energy dissipating device. The result was a higher equivalent viscous damping and hence, higher energy dissipation.

2.4 Segmented Columns

The idea of rocking is developed further to increase the rocking interfaces. This can be done by dividing the columns into segments. Hewes and Priestly (2002) investigated the performance of unbonded post-tensioned precast concrete segmental bridge columns under lateral earthquake loading. Different aspect ratios, initial tendon stress, and thickness of steel jackets (wrapping the bottom segments of the columns) were tested. Low residual drifts resulted from the high total vertical force (prestress force and applied dead load). Inelastic straining of the tendons did not occur. Hysteretic energy dissipation was low. For the design of precast segmental columns; they recommended an initial prestressing steel stress such that an initial load ratio of 0.20 is achieved,

and that the maximum axial load ratio during a seismic event should be less than or equal to 0.30.

Chou and Chen (2006) investigated the behavior of circular precast concrete-filled tube (CFT) segmental bridge columns to evaluate their seismic performance. The segments did not include any transverse or longitudinal reinforcements. The test results showed that the columns rotated about the base and the top interface of the bottom segment.

Chen Ou et al. (2005) investigated the behavior of segmental bridge columns to evaluate their seismic performance. Analytical results were compared with those obtained from three-dimensional (3D) finite element method (FEM). Columns with mild steel reinforcements across the segment joints were compared with ones without reinforcement. They concluded that a limitation on the reinforcement ratio must be applied to enable the prestressing force to re-center the column. They also found that increasing the reinforcement ratio increases the equivalent damping ratio as well as the residual displacements.

2.5 Steel jacketing

Since no reinforcement is to be used, and while the bottom segments of the columns may still need additional shear strength and lateral confinement, a substitute to lateral ties had to be introduced. The idea is to confine the concrete with an external jacket of a stronger material, i.e retrofitting.

Hewes and Priestly (2002) used steel jackets to confine the bottom segments of their column specimens. They concluded that the regions where jacketing is required should be equal to the

section dimension for axial load ratios of 0.30 or less; where the axial load ratio is the ratio of the axial stress to the compressive strength of the cross section. If the axial load ratio is greater than 0.30, then those values are increased by 50%.

Chou and Chen (2006) encased all of their column segments with A36 steel tubes, with higher wall thicknesses for the bottom segments. The steel tube did not extend the height of the segment so that contact between the steel tubes or the footing is prevented. The use of the steel tubes minimized concrete spalling.

Sakai et al (2006) studied the effect of applying steel jackets at expected plastic hinge zones of their column specimens. Applying the steel jackets decreased the peak displacement as well as the residual displacement which was less than a quarter of that measured for a similar specimen but without steel jacketing.

2.6 FRP tubes

Fiber reinforced polymers have undergone a lot of development and they have gained attention from researchers as an alternative retrofitting material. Carbon-fiber-reinforced-polymers (CFRP) can have a high modulus of elasticity, exceeding that of steel, high tensile strength, low density (114 lb/ft$^{3)}$, and high chemical inertness.

Carbon-fiber-reinforced-polymer (CFRP) layers can be used to laminate the exterior face of the bottom column segments (as jackets), satisfying shear and confinement requirements. Compared to steel and concrete jacketing, FRP has the advantage of lower weight to strength ratios, which

results in less seismic forces induced at the structure. It has higher elastic moduli, leading to higher strength under elastic loading. It is more durable because of its resistance to corrosion. ACCT-95/08 guidelines for CFRP retrofitting were applied in this study.

Ye et al. (2003) tested the performance of reinforced concrete columns with wrapped CFRP sheets. The tests also compared the effect of applying the CFRP sheets before and after loading. They concluded that using CFRP sheets improves the ductility of RC columns substantially, when the shear to flexural strength ratio is greater than 1. They also suggested an equivalent transverse reinforcement index to be used for calculating the amount of CFRP needed for seismic strengthening.

Chapter 3

Experimental Testing Program

3.1 Test specimens and parameters

This study involved studying the behavior of five moment resisting frames under cyclic lateral loading. The specimens had 20% (1:5) scale modeling the dimensions as well as reinforcement detailing. All the columns were designed with sufficient shear capacity so that flexural failure is considered in this study. Test objectives include evaluating and comparing the performance of special moment resisting frames under ACI 318-05 recommendations with the other four proposed frame systems. Table 3.1.1 provides a summary of the test specimens.

Specimen Name	Key test parameters	Column Diameter (in)	Number of segments per column	Height of segment (in)	Segment aspect ratio
F-RC	Control	8	1	45	5.625
F-FRP1	Post-tensioned FRP confined columns of single segment	8	1	45	5.625
F-FRP3	- Segmented columns - Segment aspect ratio	8	3	15	1.875
F-FRP3-R	Rubber sheets at column-beam and column-base interfaces	8	3	15	1.875
F-FRP3-S	Energy dissipation devices: modified steel angles	8	3	15	1.875

Table 3.1.1: Summary of test specimens

All the specimens were composed of frames of identical dimensions: 52.5 in. high (to the center of the beam height) and 74 in. (columns center to center) in bay width. All the columns had a clear height of 45 in. In each of the 5 specimens, a beam with a cross section of 8 in. in width and 15 in. in height was used to connect the upper ends of the two columns comprising the frame. Figure 3.1.1 shows the cross sections of the beams used in the specimens. All the specimens are fixed to identical footings 26 in. long, 16 in. wide, and 24 in. deep. The footings were designed to withstand all flexural and shear forces including the ones resulting from the post-tensioning force for specimens F-FRP1, F-FRP3, F-FRP3-R, and F-FRP3-S. Figures 3.1.2 and 3.1.3 show schematic drawings of the footing of specimen F-RC and FRP specimens respectively, along with the reinforcement used.

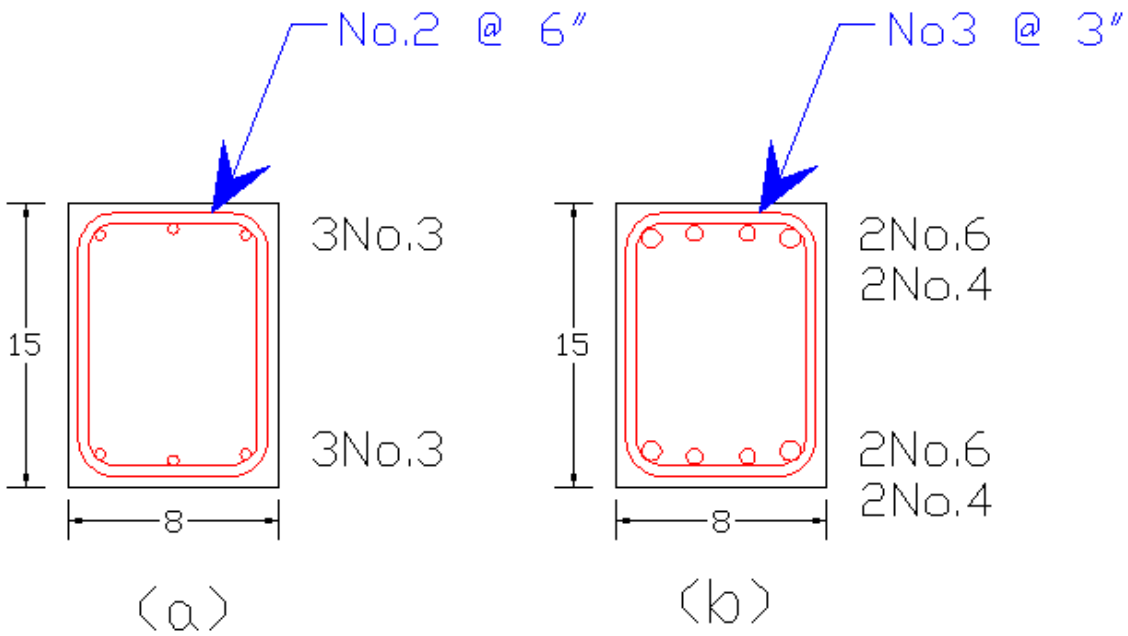

Figure 3.1.1: Beam cross sections: (a) Specimen F-RC. (b) FRP specimens

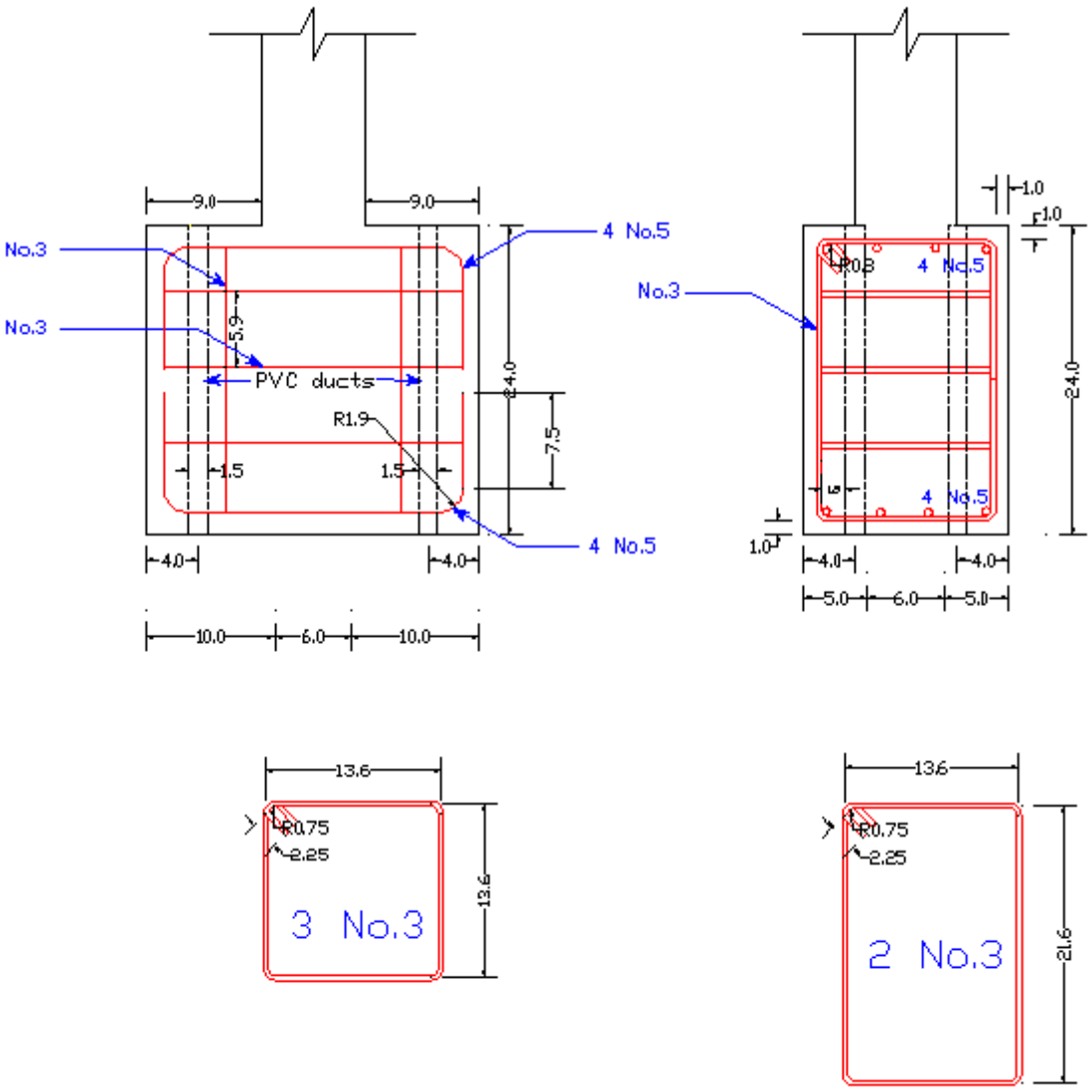

Figure 3.1.2: Schematic drawing of the footings of specimen F-RC

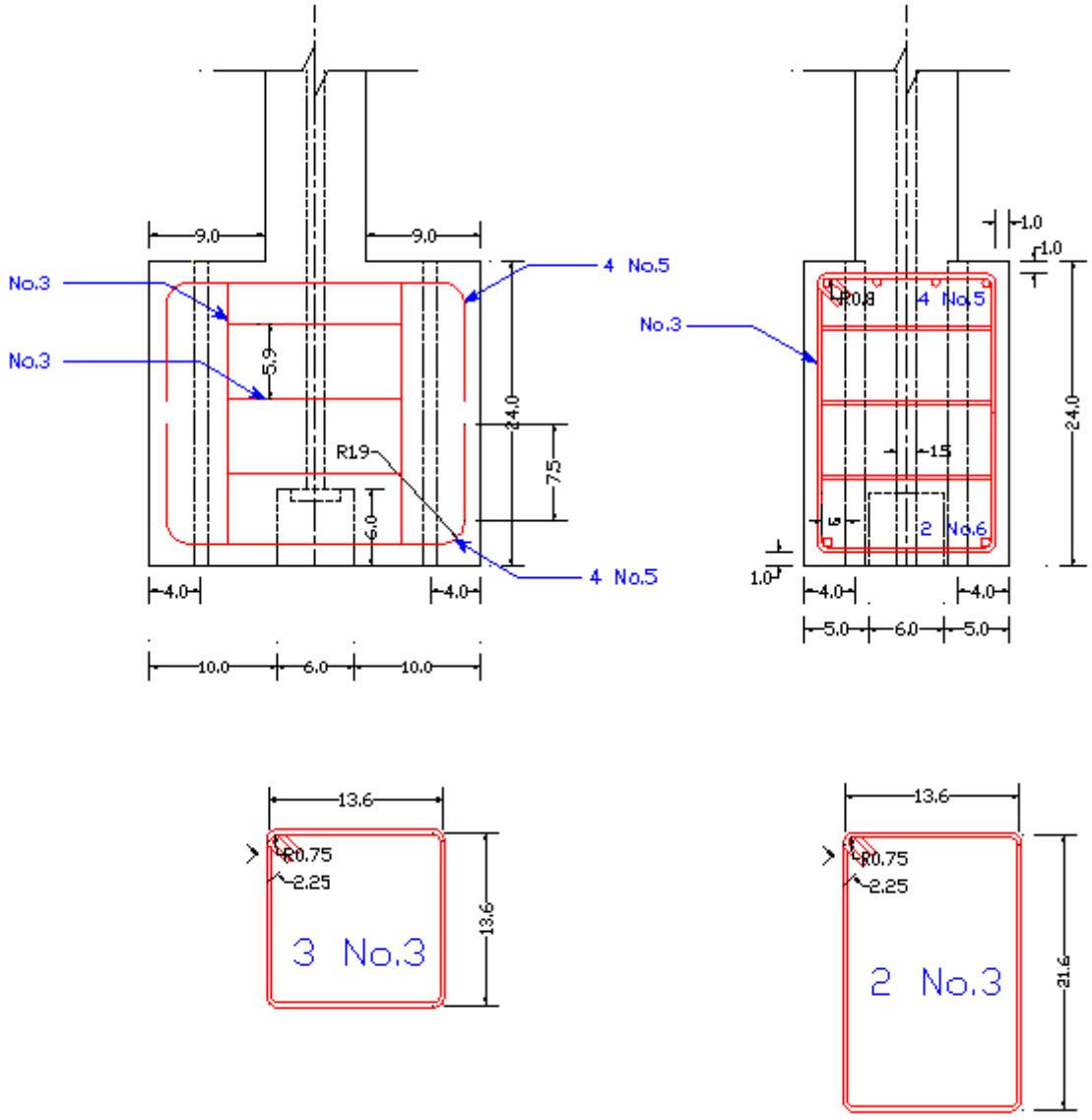

Figure 3.1.3: Schematic drawing of the footing for the FRP specimens

Specimen F-RC was the control specimen, designed according to ACI318-05 recommendations, and was composed of monolithic beam-column connections. Spiral reinforcement was used as shear reinforcement. Figure 3.1.4 shows a drawing of the frame used in specimen F-RC along with its reinforcement.

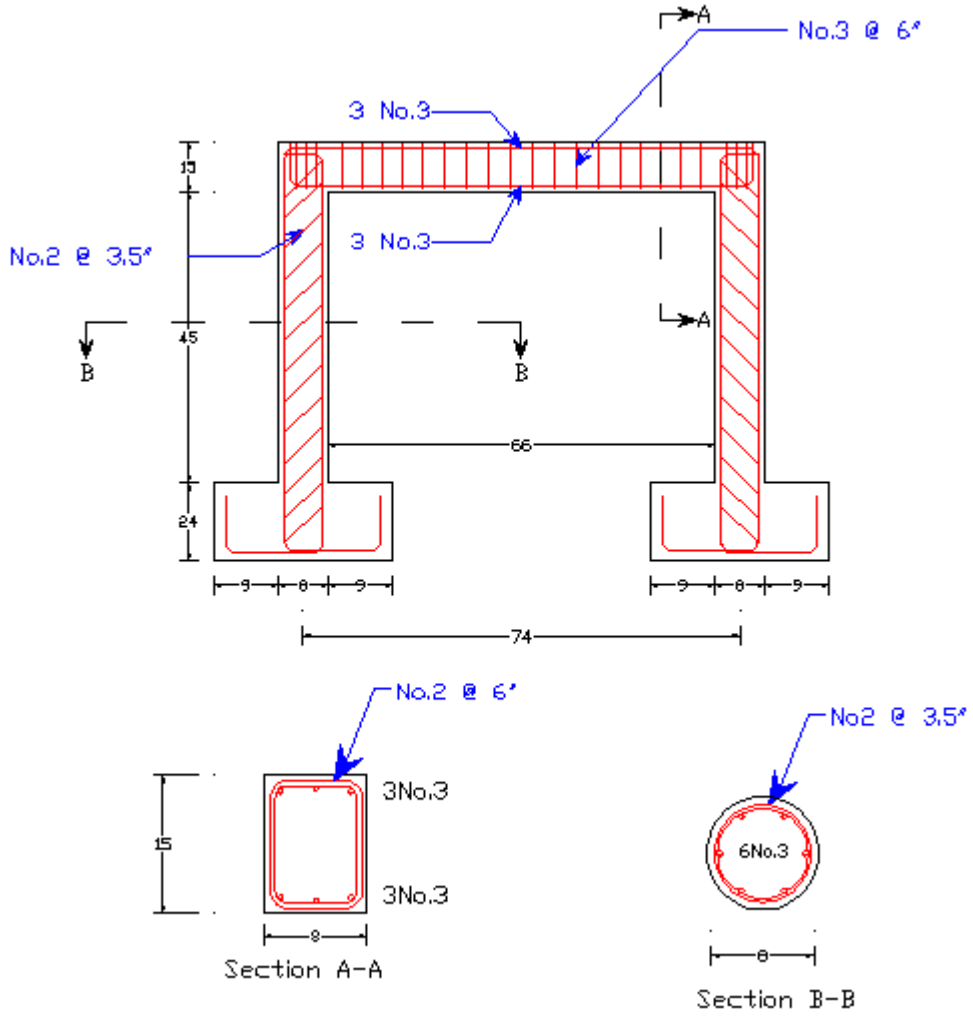

Figure 3.1.4: Reinforcement of specimen F-RC

The longitudinal steel was Grade 60 (with a tested tensile strength of 63 ksi). All reinforcement used in the footings was Grade 60. The spiral reinforcement for the columns in specimen F-RC as well as the stirrups used in all the beams was No.2 Grade 40 (with a tested tensile strength of 54 ksi).

Figure 3.1.5 shows a photo of specimen F-RC prior to testing.

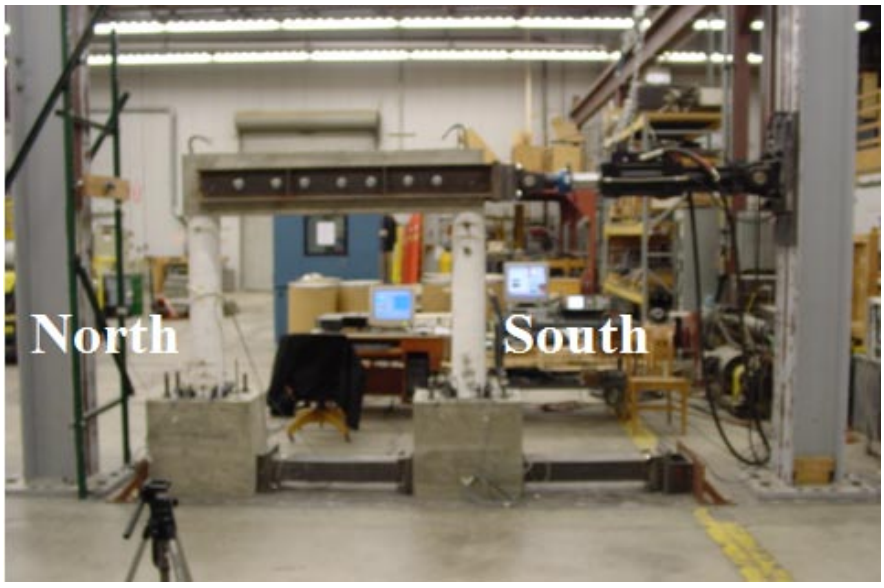

Figure 3.1.5: Specimen F-RC prior to testing

For all FRP specimens, 8 in. diameter GFRP tubes of 0.125 in. thickness were used in the columns. The tubes were “CLEAR FUBERGLASS TUBING” provided by Amalga Composites. Table 3.2.1 shows a summary of the material of the FRP tubes, which were used in the design calculations.

Material Property	Value
Flexural Modulus Longitudinal,	1300 ksi
Flexural Modulus Circumferential	3600 ksi
Tensile Strength Longitudinal	16 ksi
Tensile Strength Circumferential	40 ksi
Compressive Strength Longitudinal	27 ksi
Compressive Strength Circumferential	37 ksi
Shear Modulus	800 ksi
Shear Strength	8 ksi
CTE Circumferential	4.6 in/in/^{o}F x 10^{-6}
CTE Longitudinal	8.8 in/in/^{o}F x 10^{-6}
Poisson's ratio	0.35
Density	0.072 lb/in^{3}

Table 3.1.2: GFRP tube material properties

The concrete and FRP material properties were tested. The measured concrete compressive strength was found to be 2 ksi. Also, the modulus of elasticity of the concrete used was measured and was found to be 1975 ksi. The measured FRP tensile modulus of elasticity was found to be 2008 ksi while the tensile strength was 9.2 ksi. For the FRP tubes, the tests were conducted according to the provisions of ASTM D3039M-08 (ASTM 2008b). The concrete cylinders and FRP tubes were prepared by the author and testing was performed in collaboration with another graduate student (Dawood, Haitham).

Specimens F-FRP1 and F-FRP3 were constructed using the same concrete used for constructing specimen F-RC, and therefore have the same concrete material properties stated above.

Specimens F-FRP3-R and F-FRP3-S were constructed of concrete with an average compressive strength of 3 ksi and a measured modulus of elasticity of 2167 ksi.

Each column of specimen F-FRP1 was composed of 1 segment 45 in. long. Figure 3.1.5 shows a photo of specimen F-FRP1 Each column of specimens F-FRP3, F-FRP3-R and F-FRP3-S were composed of 3 segments 15 in. stacked on top of each other to construct a segmented column 45 in. long. Figures 3.1.6 and 3.1.7 show specimens F-FRP1 and F-FRP3, respectively, prior to testing. Figure 3.1.8 shows a closer focus on the southern column.

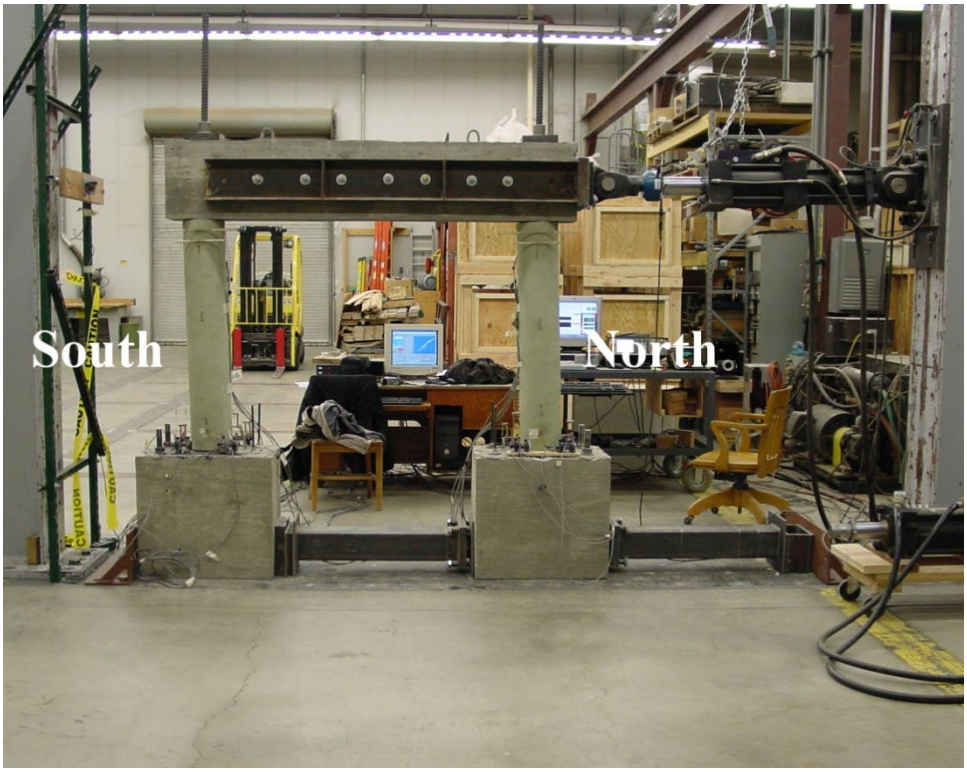

Figure 3.1.6: Specimen F-FRP1

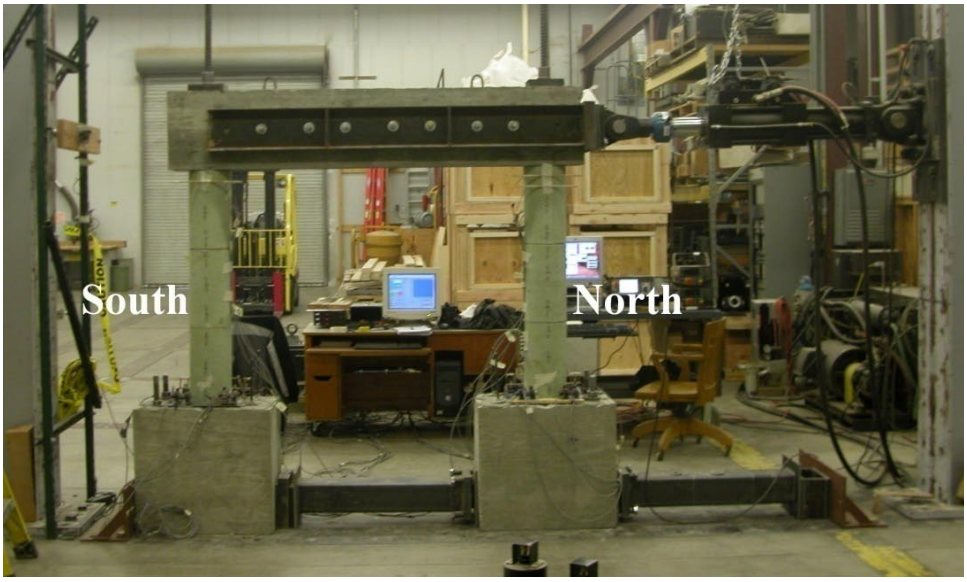

Figure 3.1.7: Specimen F-FRP3

Figure 3.1.8: Southern column of specimen F-FRP3 prior to testing

Specimen F-FRP3-R had a layer of rubber pads placed at the column-base interface as well as the column-beam interface. Each layer was composed of two sheets of rubber pads, each 0.5 in.

thick. Figure 3.1.9 shows the layout of the rubber pads in specimen F-FRP3-R. Figure 3.1.10 shows specimen F-FRP3-R prior to testing. Figure 3.1.11 shows a closer focus on the southern column of specimen F-FRP3-R.

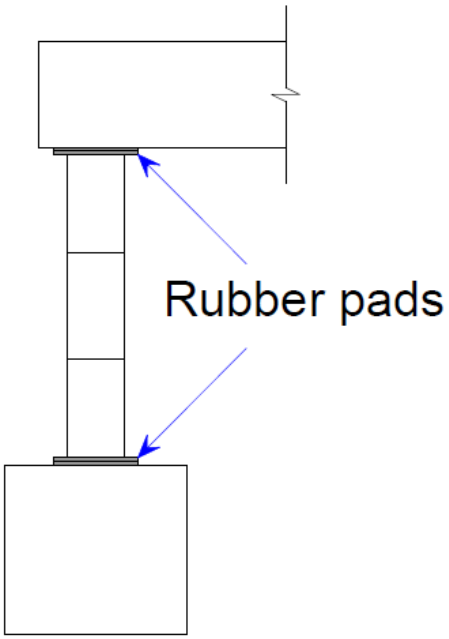

Figure 3.1.9: Rubber layers in specimen F-FRP3-R

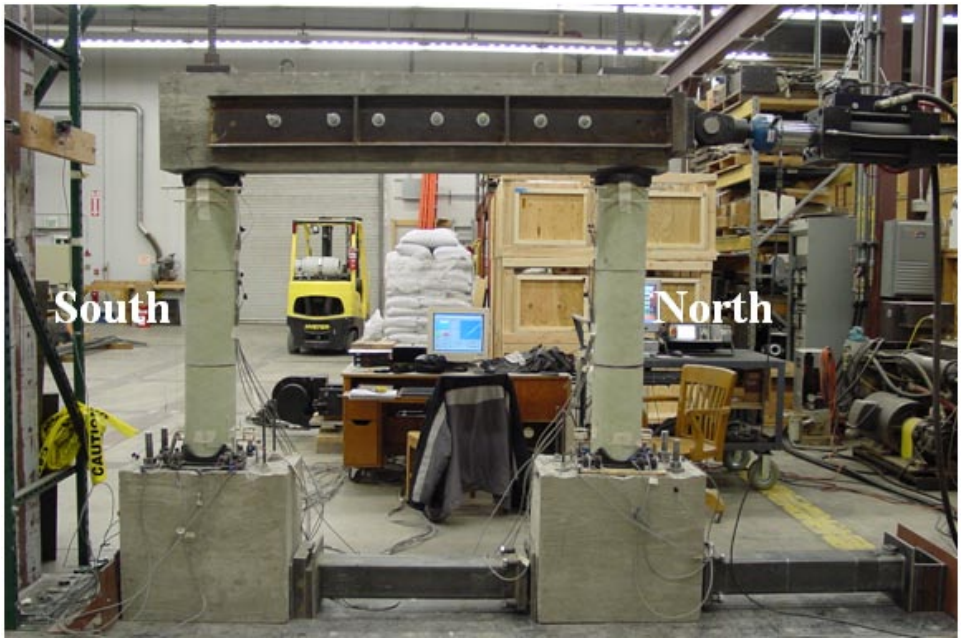

Figure 3.1.10: Specimen F-FRP3-R prior to testing

Figure 3.1.11: Southern column of specimen F-FRP3-R

Specimen F-FRP3-S had external sacrificial modified steel angles attached at four alternating corners of the frame. Each angle was constructed by welding a 0.25 in. thick plate to connect the two legs of a 4 in. long $L5 \times 5 \times \frac{5}{16}$ A36 steel angle. The thin plate was wider at the ends and narrower at the middle to concentrate the tensile stresses at the center of the plate and prevent weld failure. The cross-sectional area of the thin plate was designed so that it yields at a force resulting from a moment 10% of the maximum moment that occurs at the joints. The maximum moment values were determined from the maximum lateral load applied to specimen F-FRP3 since it is similar to specimen F-FRP3-S in everything but the attachment of the sacrificial angles. Figure 3.1.12 shows a drawing of the modified steel angle.

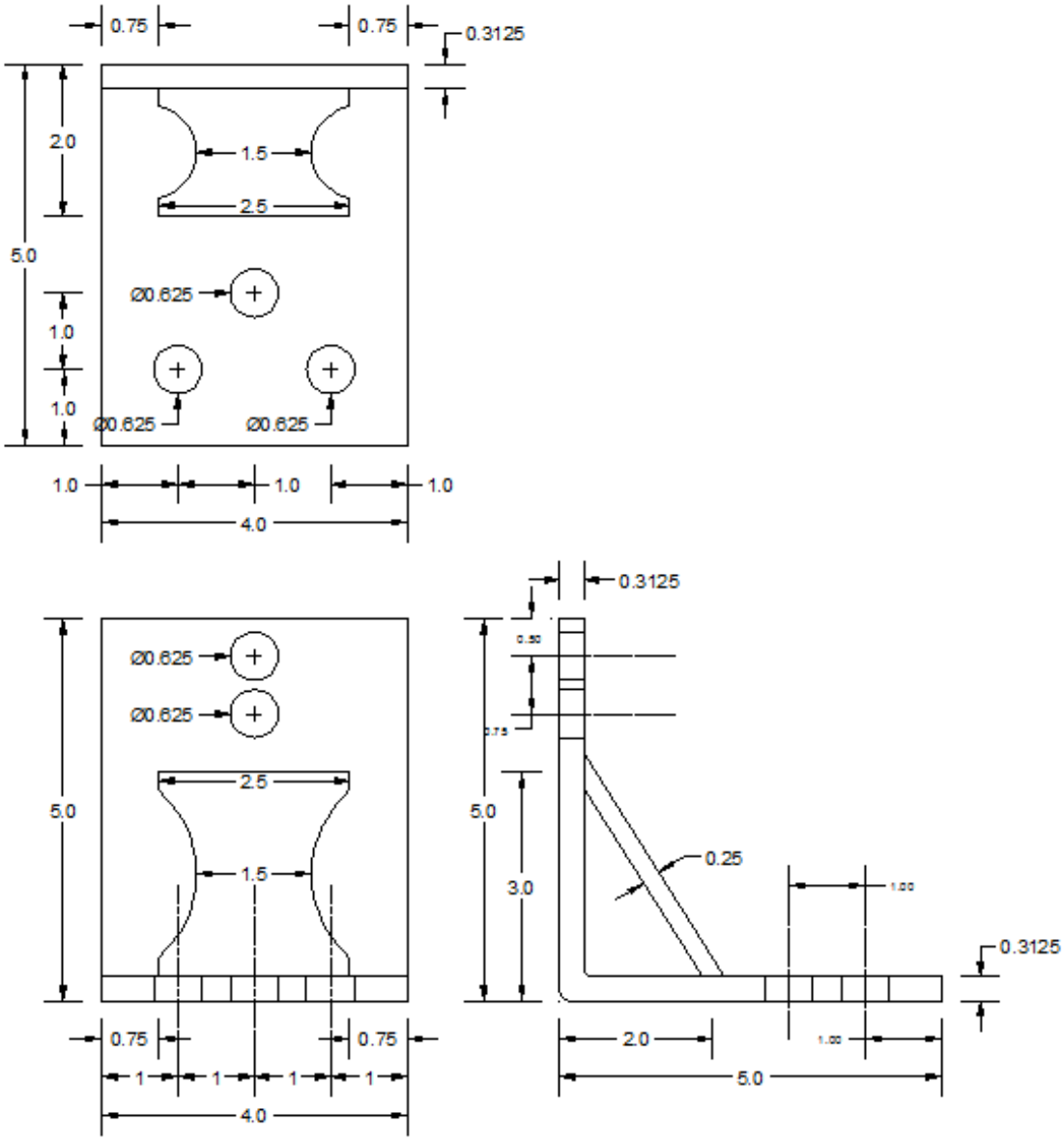

Figure 3.1.12: Sacrificial steel angle used in specimen F-FRP3-S

The sacrificial steel angle was designed with the criterion of dissipating energy by yielding of a thin plate that connects the two legs of the angle. This was implemented by attaching the modified steel angles, i.e. the energy dissipating devices to specimen F-FRP3-S at four alternating corners, as shown in Figure 3.1.13. With that layout, and when the specimen is displaced in the negative direction (south), the energy dissipation devices attached to the

northern column are in tension and therefore dissipate energy by yielding; while the energy dissipating devices attached to the southern column will be under compression, and could therefore buckle. The opposite phenomenon occurs when displacing the specimen in the positive direction (north). Since steel yielding by tension dissipates relatively a larger amount of energy than buckling, the northern column dissipates more energy when the specimen is loaded in the negative direction (south), while the southern column dissipates more energy when the specimen is displaced in the positive direction (north). Figure 3.1.14 shows specimen F-FRP3-S prior to testing. Figures 3.1.15 and 3.1.16 show the modified steel angles attached to the top of the southern column and to the bottom of the northern column, respectively.

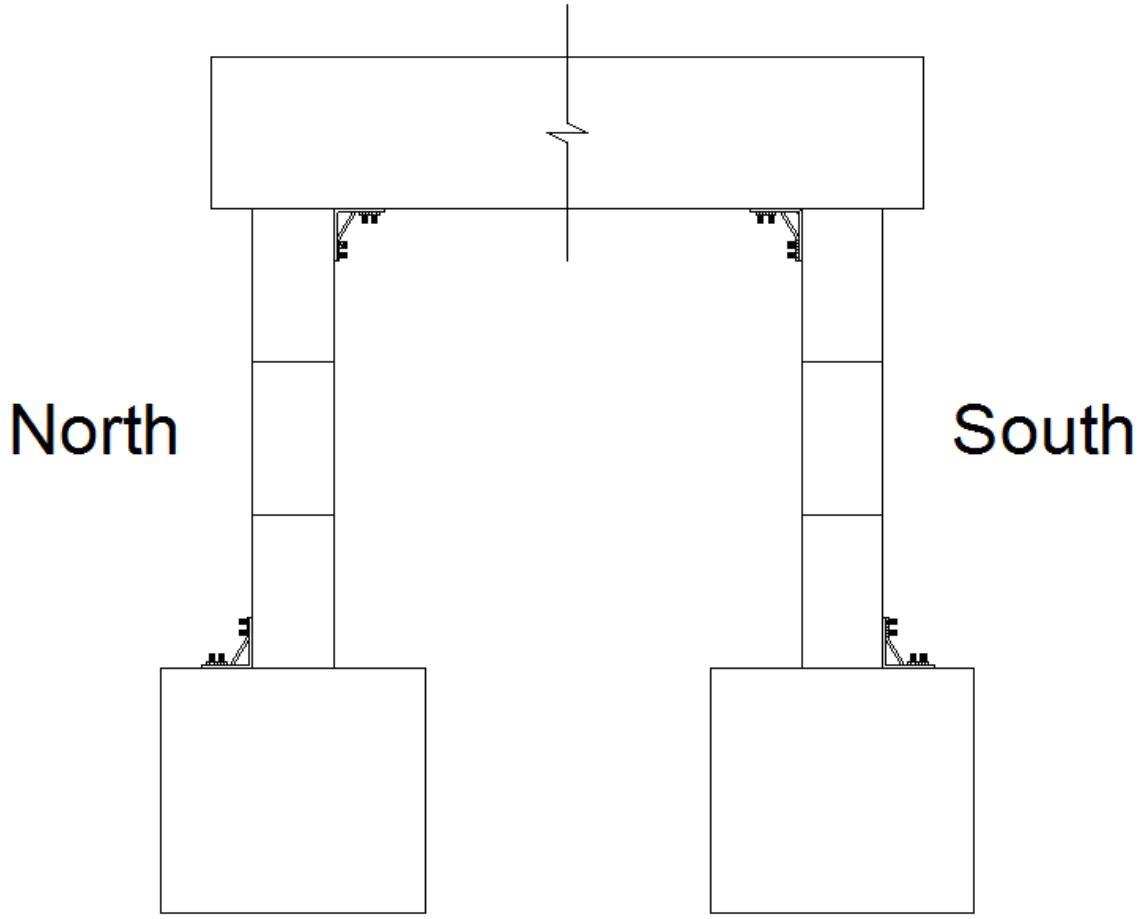

Figure 3.1.13: Layout of sacrificial steel angles in specimen F-FRP3-S

Figure 3.1.14: Specimen F-FRP3-S prior to testing

Figure 3.1.15: Energy dissipating device attached to southern column of specimen F-FRP3-S

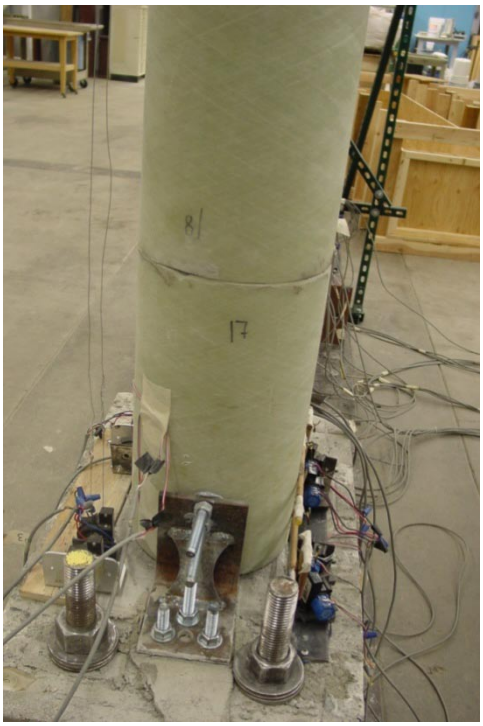

Figure 3.1.16: Energy dissipating device attached to northern column of specimen F-FRP3-S

3.2 Test setup and procedures

Figure 3.2.1 shows the overall test setup. The specimens were subjected to reverse cyclic lateral loading with increasing levels of lateral displacements under no applied external axial load. The lateral load was applied using a horizontally-aligned 50-kip hydraulic actuator.

The lateral loading was applied in a quasi-static manner. Horizontal loads were applied under displacement control. Progressively increasing displacements based on a horizontal displacement causing first yield (Δ_y) were the basis of the displacement control. Failure was defined as 20% drop in peak lateral load for each specimen. Δ_y was theoretically determined from moment curvature analyses.

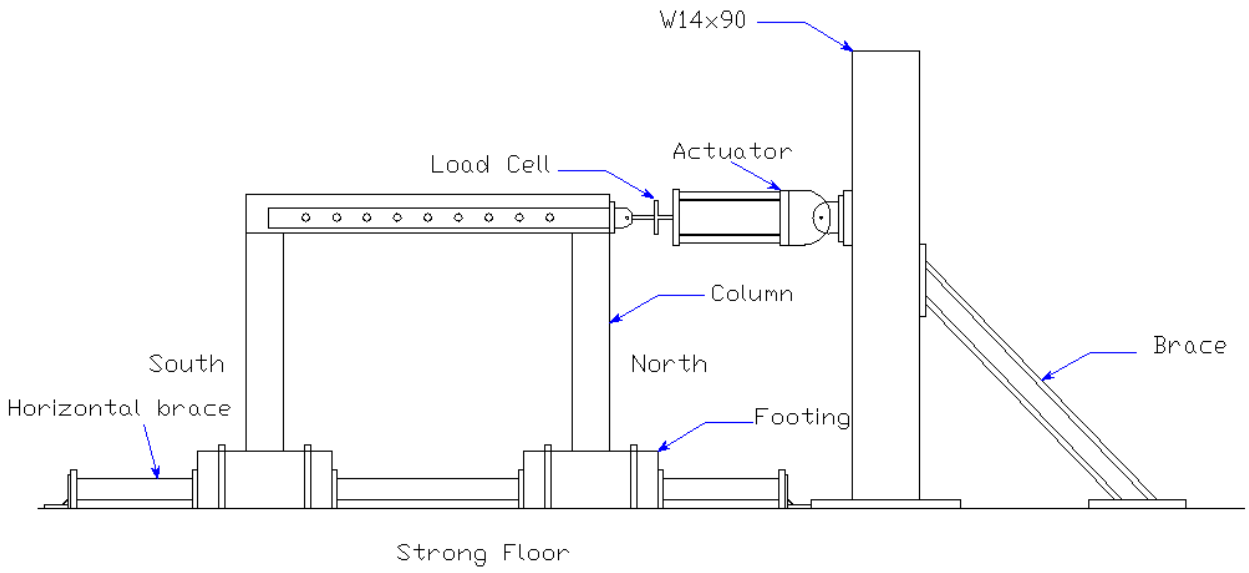

Figure 3.2.1: Test Setup

String potentiometers were used to measure rotations at different sections of each column of every specimen. The section heights were selected based on the theoretical plastic hinge length,

L_p (Equation 4.1.12 for RC columns and 4.1.15 for post-tensioned columns). To measure rotations, horizontal dowels were fixed to the columns using adhesives at heights of L_p and $\frac{L_p}{2}$; and since all of the columns were under double bending, rotations were measured at L_p and $\frac{L_p}{2}$ from the bottom of each column as well as from the top. The equations used for calculating L_p are discussed in Chapter 4. For the columns of specimen F-RC, $L_p$was found to be 5.3 in. while for columns of all of the FRP specimens, L_p was found to be 4 in.

Two string potentiometers are attached at the ends of each horizontal dowel. To calculate at each section, Equation 3.2.1 was used.

$$Rotation = \frac{\Delta_1 - \Delta_2}{I_w} \qquad \text{(Equation 3.2.1)}$$

where:

Δ_1: displacement at first string potentiometer

Δ_2: displacement at second string potentiometer

I_w: horizontal separation between the two string potentiometers

For each column of every specimen, eight string potentiometers were used as described above. Figure 3.2.2 shows the layout of the string potentiometers (SP1 to SP8) on one of the columns of specimen F-RC. Figure 3.2.3 shows the layout of the string potentiometers (SP1 to SP8) on one of the columns of the FRP specimens.

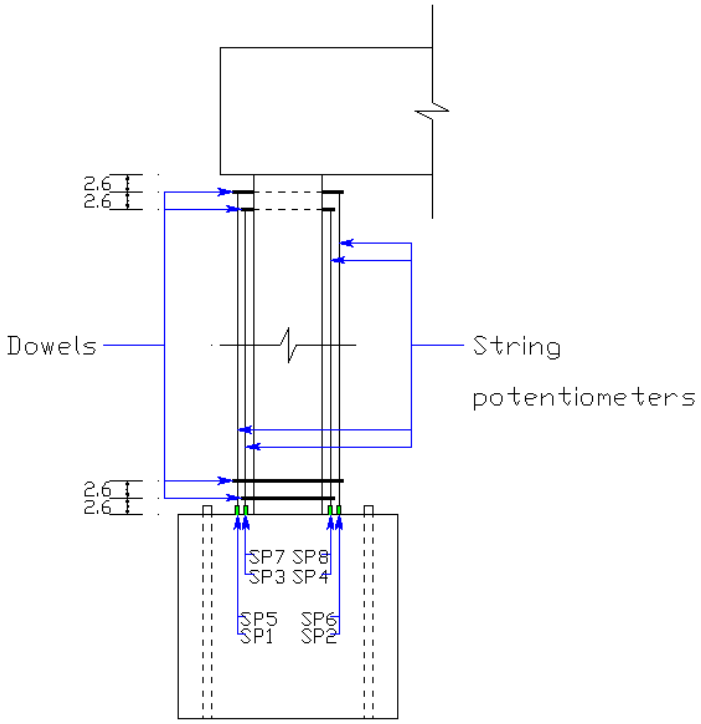

Figure 3.2.2: Layout of string potentiometers for specimen F-RC

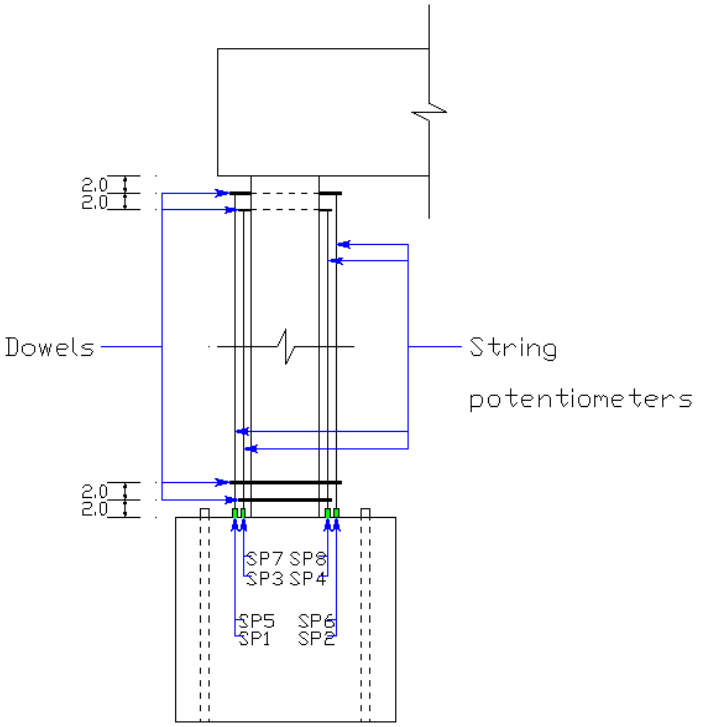

Figure 3.2.3: Layout of string potentiometers for FRP specimens

Curvature was calculated at all the sections at which rotations were measured using equation 3.2.2.

$$\varphi = \frac{\Delta\theta}{h} \qquad \text{(Equation 3.2.2)}$$

where:

φ: curvature of a column section

$\Delta\theta$: difference in rotation between the upper and lower interfaces of the column section

h: height of the column section

The rotation of the footing and beam interfaces are assumed to be zero since they are relatively much stiffer to rotation than the columns. Therefore, for the sections directly above the footings or directly below the beam, $\Delta\theta$ is the measured rotation from Equation 3.2.1 minus zero. For the other sections, $\Delta\theta$ is the rotation of that section minus the rotation of the section closer to the base in lower joints and the section closer to the beam for the upper joints. When the rotations of two successive sections are equal, the curvature between them is zero. Increasing the number of sections at which rotations are measured while simultaneously decreasing the vertical distance h between them provides more accurate curvature measurements and distribution along the column.

Strain gages were used to monitor the strains in the column longitudinal bars for specimen F-RC, the strain in the post-tensioning steel bars in the FRP specimens, and strain of the FRP tubes in the circumferential and longitudinal directions.

For each post-tensioning bar, four strain gages were attached at heights coinciding with the locations of the center of the theoretical plastic hinge L_p (Equation 4.1.15) and $2L_p$, that is at 2

in. and 4 in. above the column-base interface and at 2 in. and 4 in. below the column-beam interface of each column of every FRP specimen. Bar strain readings were collected during the post-tensioning stage of each FRP specimen as well during testing.

Circumferential and longitudinal strain at the FRP tubes was also measured. For each column of every FRP specimen, 6 circumferential and 2 longitudinal strain gages were attached.
For each column of specimens F-FRP1, F-FRP3, F-FRP3-R, and F-FRP3-S; the gages measuring circumferential strain were divided into two groups: one measuring circumferential strain at the north face of the column while the other group was at the south face. The circumferential strain gages were set at three heights: 2 in., 41 in., and 43 in. At each height, two strain gages were used: one at the north face of the column while the other was at the south face of the column. The gages measuring longitudinal strain of every column of specimens F-FRP1, F-FRP3, F-FRP3-R, and F-FRP3-S; were set at the west face of the column and at two heights: 4 in. and 41 in. Figure 3.2.4 shows the layout of the circumferential strain gages (gages C1 to C12) and the longitudinal strain gages (gages L1 to L4) used in the FRP specimens.

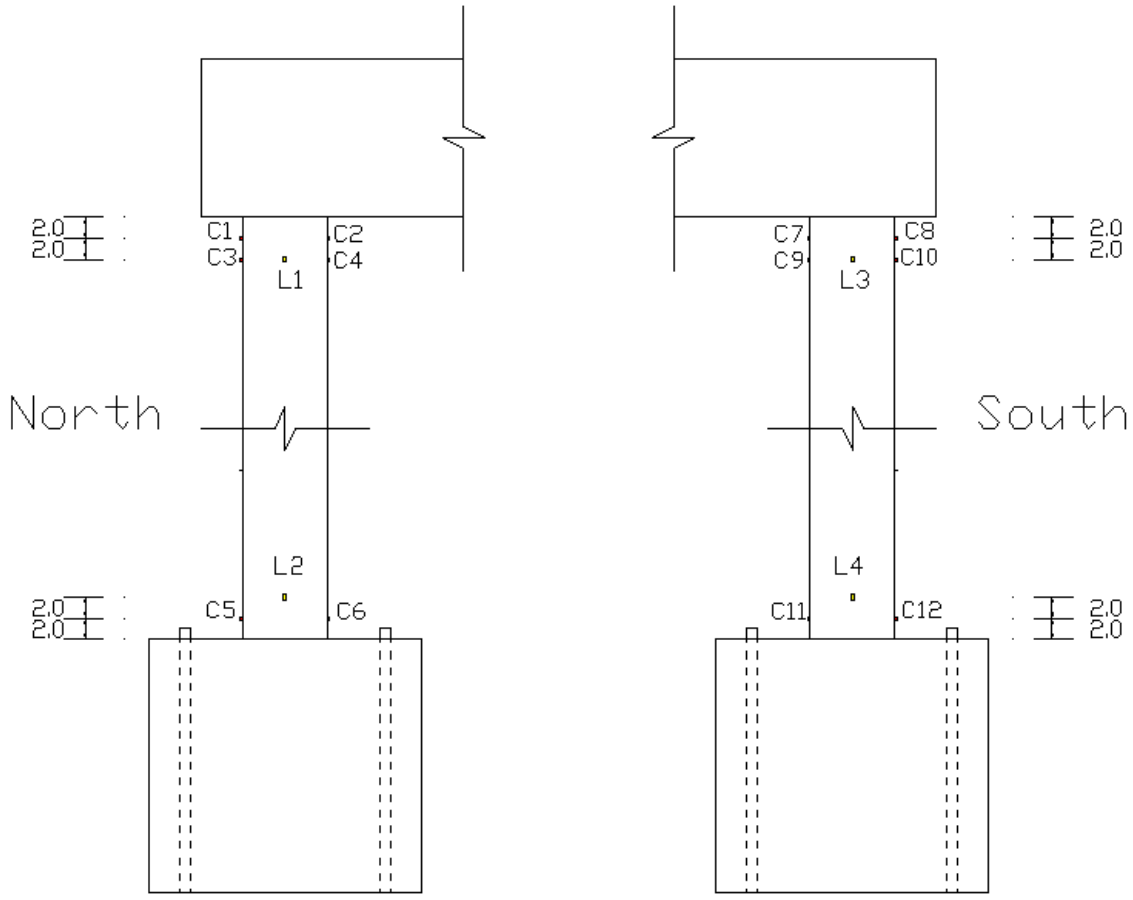

Figure 3.2.4: Layout of circumferential and longitudinal strain gages of FRP specimens

Using the procedure described in Chapter 4, the initial post-tensioning stress was determined, and knowing the post-tensioning bar modulus of elasticity (29700 ksi), the initial post-tensioning bar strain was calculated to be 935 micro-strain. Post-tensioning of the FRP specimens was conducted using hydraulic jacks which were installed at the top of the beam. The nuts were manually tightened after the bar strain reach the target initial strain. Immediate losses occurred as soon as the hydraulic jack was turned off, so the procedure was repeated until the target initial post-tensioning strain is achieved. Figures 3.2.5 and 3.2.6 show the post-tensioning hydraulic jack during the procedure of post-tensioning.

Figure 3.1.5: Post-tensioning specimen F-FRP3

Figure 3.1.6: Post-tensioning hydraulic jack

Chapter 4

Analytical Procedures

4.1 Moment-curvature analysis

Moment curvature analysis was used for determining the deformation response to loads applied on reinforced concrete sections using nonlinear stress-strain relationships, particularly at critical sections of columns where moment is greatest. Moment-curvature analyses were used in this study to generate pushover curves for the specimens.

4.1.1 Moment-curvature analysis for the reinforced concrete column

For the reinforced concrete frame, the cross-section parameters and the material properties were input to XTRACT (XTRACT v3.0.8) to obtain a moment-curvature relationship. XTRACT release notes indicate using Mander's confined reinforced concrete stress strain model (Mander et. al, 1988). The built in steel rebar stress-strain model was used, but with updating the yield strength (f_y) as given below.

The reinforced concrete column cross-section properties were as per table 4.1.1.

Property	Value
Concrete cover	0.5 in.
Unconfined concrete compressive strength	2 ksi
E_c	1975 ksi
Type of lateral reinforcement	Spiral
Spacing of lateral reinforcement	3.5 in.
Yield strength of lateral reinforcement	54 ksi
Longitudinal reinforcement	6#3 Grade 60
Yield strength of longitudinal reinforcement	63 ksi

Table 4.1.1: Specimen F-RC material properties used in XTRACT

The analysis report of XTRACT is available in the Appendix.

4.1.2 Moment-curvature analysis for post-tensioned column

The moment-curvature behavior of the post-tensioned column differs from the reinforced concrete column. The reason is that the post-tensioning tendon stretches at certain stages of lateral loading, leading to a varying axial load. A method for obtaining the moment-curvature curve was proposed by Hewes and Priestly (2002), and it is adopted in this study.

The structural deformations of an unbounded post-tensioned column are due to the rigid rotation of the column (or column segment) about its base. The base of the column exhibits a rocking

effect where it lifts off the ground once the moment due to downward vertical forces is overcome. These vertical forces include the weight of the structure plus the post-tensioning force which is the main moment resistance against overturning.

There are three stages of response under lateral loading of the post-tensioned column, as shown in Figure 4.1.1 (after Hewes and Priestley, 2002).

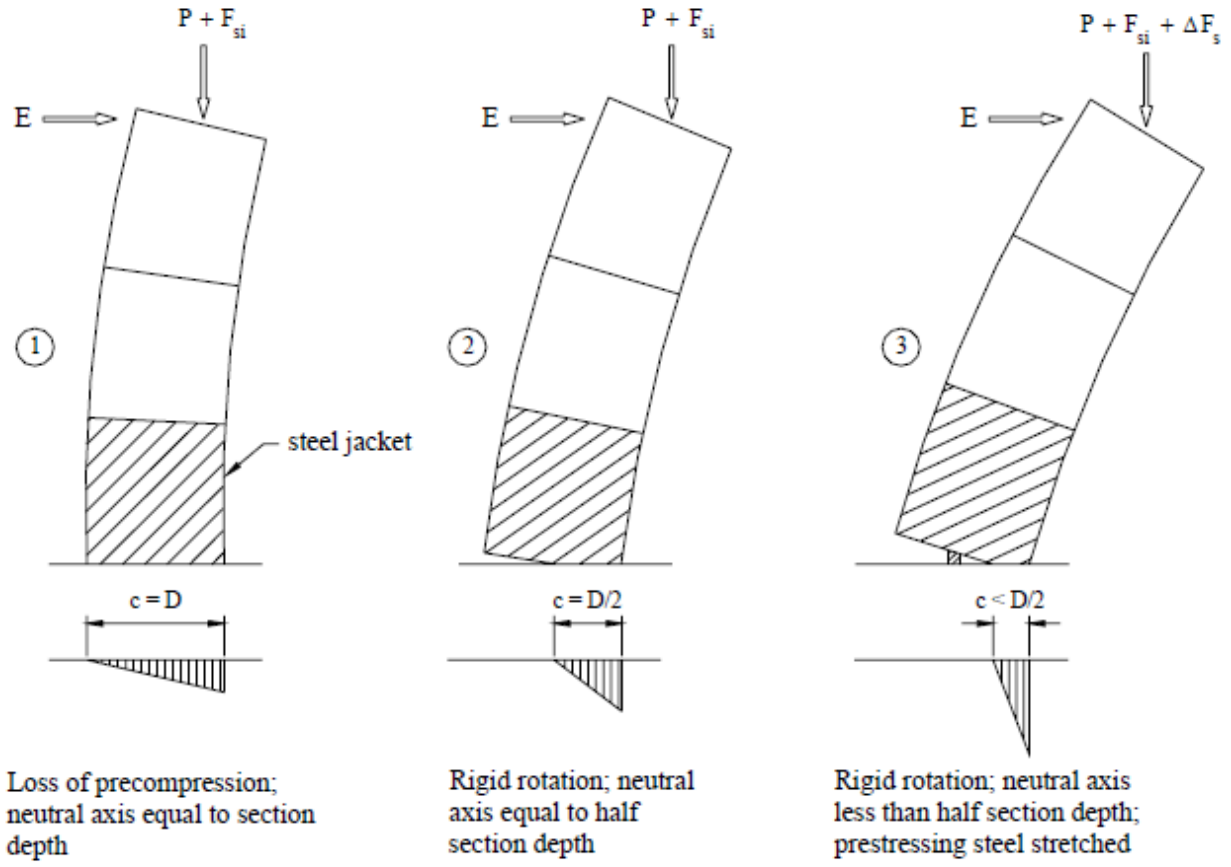

Figure 4.1.1: Post-tensioned column at key stages of response (Hewes and Priestley, 2002)

Initially, the column is stressed with the post-tensioning force (after losses) "F_{si}" and the dead load "P". As the lateral load "E" is increased, compression stresses under the column base will

vary linearly increasing at one side while decreasing at the other until it drops to zero at one side of column base. This defines the first significant point of the column response, first cracking. The behavior is still elastic during this stage. The total vertical force acting on the column is known and equilibrium is achieved by the resultant concrete compression force "*C*". By trial and error, values for the concrete compression strain "ε_c" are assumed, iteration is conducted to find the neutral axis depth "*c*" so that equilibrium of the vertical forces is satisfied on the section:

$$C = P + F_{si} \qquad \text{(Equation 4.1.1)}$$

where:

C: resultant concrete compressive force (Equation 4.1.2)

P: dead load

F_{si}: initial post-tensioning force after losses

The resultant concrete compression force is found by in integrating the stress over the neutral axis depth:

$$C = \int_{\frac{D}{2}-c}^{\frac{D}{2}} f_c \, dA \qquad \text{(Equation 4.1.2)}$$

where:

f_c : compressive stress function with respect to strain distribution

D: diameter of the column

The section moment capacity is then calculated using equation 4.1.3.

$$M = \int_{\frac{D}{2}-c}^{\frac{D}{2}} f_c \cdot x \, dA \qquad \text{(Equation 4.1.3)}$$

where:

M: moment capacity of section

x: centroid of integral area over which the compression function is integrated

Following this stage, and as the lateral load "E" increases, a crack will develop at the column base and will keep propagating until it reaches half the depth of the cross section. This situation defines the second key point of the column response. Elastic behavior is retained up to this point. The beginning of nonlinearity in response begins beyond this stage. The neutral axis depth "c" is at the mid-depth of the column cross section, and the post-tensioning stress is not significantly changed up to this point. The curvature at this point is denoted as "Φ_e" and is calculated using the assumed the value *εc* that causes the 4.1.1 be satisfied when "c" is at mid-depth.

$$\varphi_e = \frac{\varepsilon_c}{c_e} \qquad \text{(Equation 4.1.4)}$$

where:

c_e: neutral axis at stage 2 = $\frac{D}{2}$

The third and final stage of column response follows as the lateral load "E" increases while the neutral axis depth passes the mid-depth causing stretching of the post-tensioning tendon, increasing the steel stress by "Δf_s". The increase in bar strain "$\Delta\varepsilon_s$" is given by:

$$\Delta\varepsilon_s = \frac{\Delta L}{L_t} = \frac{\theta_p(\frac{D}{2}-c)}{L_t} \qquad \text{(Equation 4.1.5)}$$

where:

$\Delta\varepsilon_s$: increase in post-tensioning bar strain

ΔL: increase in post-tensioning bar length

L_t: unbonded tendon lengths

θ_p: plastic rotation (Equation 4.1.9)

The post-tensioning stress increase is calculated using equation 4.1.6.

$$\Delta f_s = \Delta \varepsilon_s \cdot E_s \qquad \text{(Equation 4.1.6)}$$

To complete the calculations for the moment-curvature response, these calculations are performed.

$$\varphi_t = \frac{\varepsilon_c}{c} \qquad \text{(Equation 4.1.7)}$$

$$\varphi_p = \varphi_t - \varphi_e \qquad \text{(Equation 4.1.8)}$$

$$\theta_p = \varphi_p \cdot L_p \qquad \text{(Equation 4.1.9)}$$

$$F_s = F_{si} + \Delta F_s = (f_{si} + \Delta f_s)A_s = (f_{si} + \Delta \varepsilon_s \cdot E_s)A_s \qquad \text{(Equation 4.1.10)}$$

where:

φ_t: total curvature (elastic and inelastic)

φ_p: plastic curvature

L_p: plastic hinge length (Equations 4.1.12 and 4.1.15)

ΔF_s: increase in post-tensioning bar force

A_s: area of post-tensioning bar

E_s: post-tensioning bar modulus of elasticity

Equilibrium of vertical forces on the section should be checked by finding the resultant compressive force on the section "C" using equation 4.1.2 and then checking if "C" is equal to

the sum of the dead load "P" and the increased post-tensioning force "F_s" by satisfying equation 4.1.11.

$$C = \int_{\frac{D}{2}-c}^{\frac{D}{2}} f_c \, dA \qquad \text{(Equation 4.1.2)}$$

$$C = P + F_s \qquad \text{(Equation 4.1.11)}$$

If equilibrium is not satisfied, the assumed neutral axis depth "c" is changed and the calculations repeated until equilibrium is achieved. The moment capacity of the section is calculated using equation 4.1.3.

$$M = \int_{\frac{D}{2}-c}^{\frac{D}{2}} f_c \cdot x \, dA \qquad \text{(Equation 4.1.3)}$$

The above procedure is implemented for values of ε_c ranging up to the ultimate concrete compression strain "ε_{cu}" which depends on the material constitutive behavior discussed in section 4.2.

The post-tensioning stress of the post-tensioning bar at the ultimate stage can be calculated using the above procedure. Therefore, the value of the initial post-tensioning stress should be selected so that the bar stress stays in the elastic region until the column fails. This criterion ensures that the central tendon will provide a re-centering force for the column since the post-tensioning bar will not yield. However, the initial post-tensioning stress should satisfy the required clamping force between the column segments so that shear is transferred across the column segments.

Equation 4.1.12 (Priestley et al., 2007) was used to calculate the plastic hinge length for the columns of specimen F-RC.

$$L_p = kL_c + L_{sp} \geq 2L_{sp} \qquad \text{(Equation 4.1.12)}$$

where:

L_p: plastic hinge length

k: factor related to the ratio of ultimate to yield strength of longitudinal reinforcement (Equation 4.1.13)

L_c: distance from critical section to point of contraflexure

L_{sp}: strain penetration length (Equation 4.1.14)

$$k = 0.2\left(\frac{f_u}{f_y} - 1\right) \leq 0.08 \qquad \text{(Equation 4.1.13)}$$

where:

f_u: ultimate tensile strength of longitudinal reinforcement

f_y: yield strength of longitudinal reinforcement

$$L_{sp} = 0.15 f_y d_l \qquad \text{(Equation 4.1.14)}$$

where:

d_l: diameter of the longitudinal reinforcement

Equation 4.1.15 was used to calculate the plastic hinge length of the post-tensioned columns of the FRP specimens.

$$L_p = \frac{D}{2} \qquad \text{(Equation 4.1.15)}$$

where:

D: core diameter of column

4.2 Material constitutive behavior

Confinement significantly enhances the strength and ductility of concrete, and therefore must be accounted for in stress-strain calculations. The stress-strain relationship of confined concrete is required for moment-curvature as well as pushover analysis (Chapter 6). Confined concrete stress-strain relationships vary depending on the method of confinement such as confinement with lateral reinforcement (ties or spiral) or external jackets or tubes made of different types of materials.

Several models for the stress-strain relationships of confined columns are available. Those relationships depend on the parameters of the encasing tubes and the column cross section, such as: area and material property of the FRP tubes, geometry of the cross section, and the radius of circular sections. As discussed in Section 4.1, XTRACT uses Mander's model for confined reinforced concrete with spiral reinforcement (Mander et al., 1988). In this study, the model presented by Samaan et al. (1998) is used in the calculations for the FRP specimens.

In summary, the concrete stress "f_c" as a function of the concrete compressive strain "ε_c" is modeled as a bilinear relation with the general shape shown in Figure 4.2.1 (Samaan et. al., 1998). The model is computed using Equation 4.2.1.

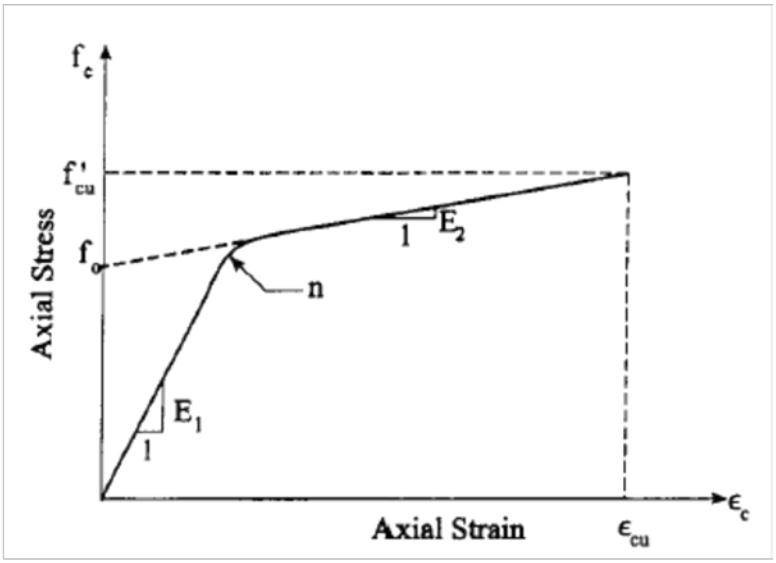

Figure 4.2.1: Parameters of bilinear confinement model (Samaan et al., 1998)

Confined concrete shows two stages of response while undergoing increasing compressive stresses. Initially, as the compressive stresses increase from zero, the behavior of the FRP confined concrete is similar to the behavior of unconfined concrete and has a similar slope (E_c). As the compressive stresses increase, and due to Poisson's effect, the circular column dilates radially, increasing the hoop stress on the FRP tube confining the concrete column. As the compressive stresses in the concrete core approaches f'_c , microcracks propagate to a level where Poisson's ratio does not describe the relation between axial and lateral strains. At this point, the FRP tube is activated and begins to affect the response. The second slope of the model (E_2) depends on the unconfined compressive strength of concrete, the modulus of elasticity of the FRP tube in the hoop direction (E_j), the thickness of the FRP tube (t_j), and the core diameter (D), as shown in Equation 4.2.2.

$$f_c(\varepsilon_c) = \left[\frac{(E_1 - E_2)\varepsilon_c}{\left[1+\left[(E_1-E_2)\cdot\frac{\varepsilon_c}{f_0}\right]^n\right]^{\frac{1}{n}}}\right] + E_2 \cdot \varepsilon_c \qquad \text{(Equation 4.2.1)}$$

where:

E_1: first slope of the stress-strain bilinear confinement model = modulus of elasticity of concrete (ksi)

f'_c: concrete unconfined compressive strength (ksi)

E_2: second slope of the stress-strain bilinear confinement model (Equation 4.2.2)

f_0: the intercept stress of the stress-strain function at which the slop changes (Equation 4.2.3)

n: constant equal to 1.5

$$E_2 = 52.411 f'^{0.2}_c + 1.3456 \frac{E_j t_j}{D} \qquad \text{(Equation 4.2.2)}$$

where:

E_j: modulus of elasticity of FRP tube in the circumferential direction (ksi)

t_j: thickness of FRP tube (in.)

D: core diameter (in.)

$$f_0 = 0.872 f'_c + 0.371 f_r + 0.908 \qquad \text{(Equation 4.2.3)}$$

where:

f_r: confinement pressure (Equation 4.2.4)

$$f_r = \frac{2f_j t_j}{D} \qquad \text{(Equation 4.2.4)}$$

where:

f_j: hoop strength of the tube (ksi)

Other important parameters that are calculated from this relation are ultimate confined stress (f'_{cu}) and the ultimate confined strain (ε_{cu}) using equations 4.2.5 and 4.2.6, respectively.

$$f'_{cu} = f'_c + 3.38 f_r^{0.7} \qquad \text{(Equation 4.2.5)}$$

$$\varepsilon_{cu} = \frac{f'_{cu} - f_0}{E_2} \qquad \text{(Equation 4.2.6)}$$

For modeling the FRP confined columns, the resulting Poisson's ratio also needs to be calculated. Mirmiran and Shahawy (1997) presented a model for describing the Poisson's ratio of the FRP confined concrete columns under increasing axial strains.

For unconfined concrete, the dilation rate (change in radial strain divided by change in axial strain) which is characterized by Poisson's ratio increases as the axial strain increases, reaching a maximum as the micro-cracks propagate leading to failure. For FRP confined concrete, the dilation rate increases with increasing axial strains reaching a maximum (μ_{max}) when the FRP gets activated. At that point, the FRP contains the dilation rate of the concrete core and reduces it to a constant value (μ_u), as shown in Figure 4.2.2 (Samaan et al., 1998). Equations 4.2.7 and 4.2.8 (Mirmiran and Shahawy, 1997) were used to find μ_{max} and μ_u.

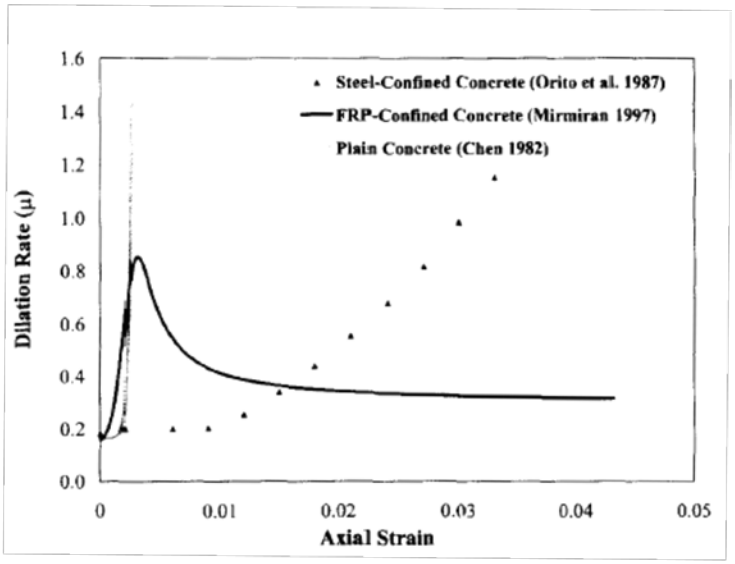

Figure 4.2.2: Dilation curves of FRP confined concrete vs. Axial strain of FRP confined concrete (Samaan et al., 1998)

$$\mu_{max} = -0.977Ln\left(\frac{2E_j t_j}{f'_c D}\right) + 3.938 \qquad \text{(Equation 4.2.7)}$$

$$\mu_u = -0.187Ln\left(\frac{2E_j t_j}{f'_c D}\right) + 0.881 \qquad \text{(Equation 4.2.8)}$$

Chapter 5

Experimental Results

5.1 Introduction

In this chapter, the results of the experimental tests performed on the five specimens are presented. They include:

- Test observations and load-displacement hysteresis figures.
- Backbone curves.
- Secant stiffness curves.
- Energy dissipation curves.
- Equivalent viscous damping curves.
- Post-tensioning bar strain curves.
- FRP strain curves.
- Rotation figures.
- Curvature curves

5.2 Test observations and hysteresis figures

This section presents the experimental tests observations and the load-displacement hysteresis curves for the five specimens. The figures show differences in the behavior of the specimens in regard to the peak loads and permanent deformation after successive loading cycles.

5.2.1 Specimen F-RC

Specimen F-RC was the control specimen and was designed according to the provisions of ACI 318-05 for special moment resisting frames. This specimen is the control specimen with which the other four proposed specimens are to be compared. Figure 5.2.1 shows specimen F-RC while testing.

Figure 5.2.1: Specimen F-RC after testing

Figure 5.2.2 shows the load-displacement hysteresis curve for specimen F-RC. Positive displacements indicate displacement to the "North" direction of the specimen.

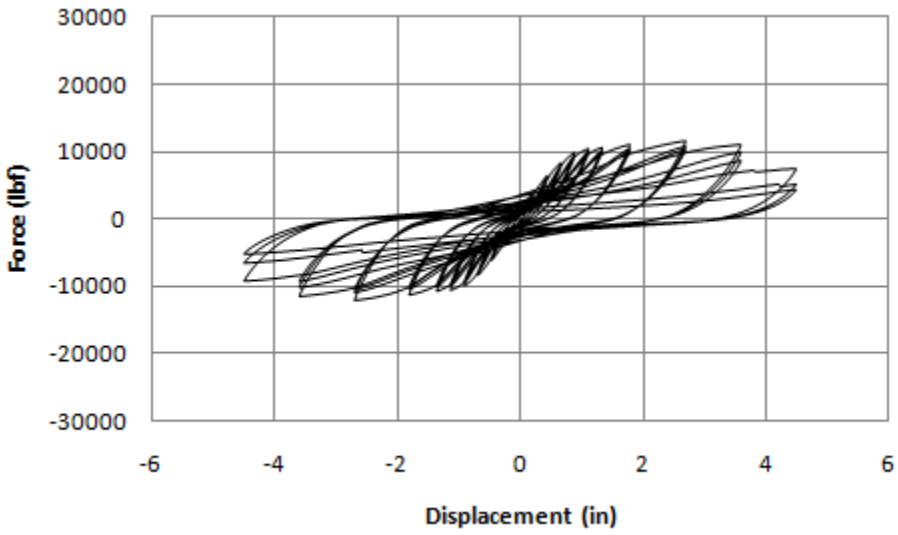

Figure 5.2.2: Specimen F-RC Load-Displacement Hysteresis Curve

The maximum load applied on specimen F-RC in the positive direction was 11840 lb and it occurred at a displacement level of 2.71 in. The maximum load in the negative direction was 11894 lb and occurred at displacement level of -2.69 in. The difference in magnitude of the maximum loads in the two directions is 0.45% which is relatively insignificant.

Minor horizontal cracks in the columns began to appear at a displacement level of 0.40 in., Figure 5.2.3. Cracks, which were at the upper joints, extended to the beam at a lateral displacement level of 1.40 in., as shown in Figure 5.2.4. Significant concrete spalling began to occur at the joints after the 2.70 in. cycle, Figure 5.2.5. Plastic Hinges began to form at all four joints with lengths ranging from 4 in to 7 in. Excessive concrete spalling occurred, the concrete cover was lost and the spiral reinforcement began to appear. Crushing of confined concrete at the joints began to appear at 3.6 in. lateral displacement, Figure 5.2.6. The spiral reinforcement of the northern column fractured at a lateral displacement level of 3.8 in. and a load of 7300 lb.

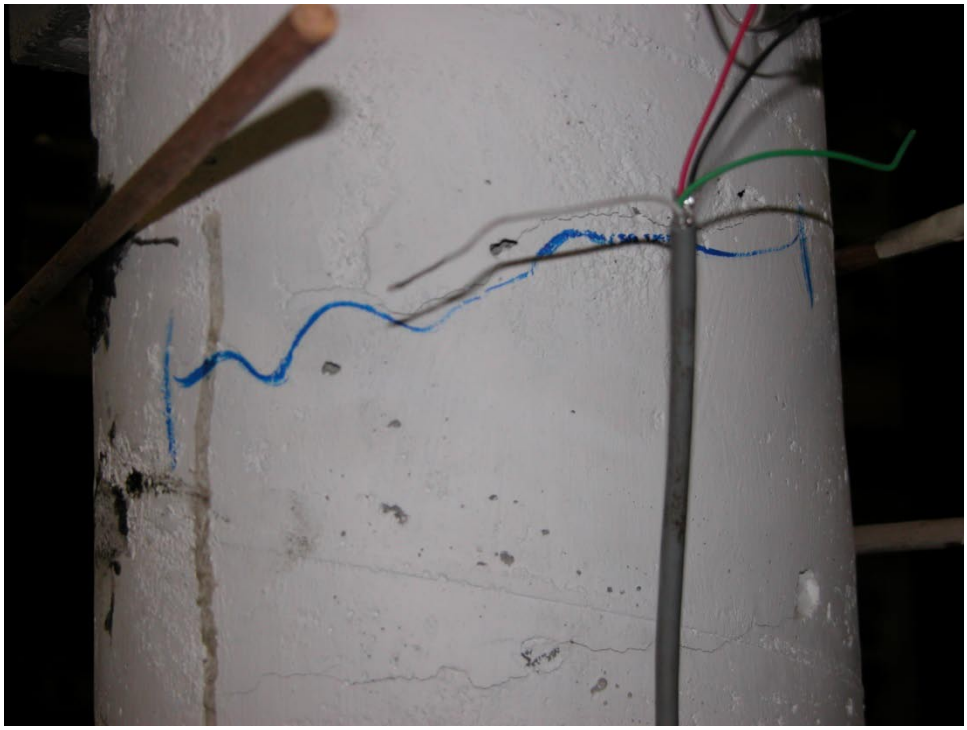

Figure 5.2.3: Horizontal cracks at the top of Column N at 0.40 in. displacement

Figure 5.2.4: Cracks extending to the beam at 1.40 in displacement

Figure 5.2.5: Concrete spalling at 2.7 in. displacement

Figure 5.2.6: Core concrete crushing at 3.6 in. displacement

All four plastic hinges suffered excessive damage by the final loading cycle leading to excessive loss of stiffness where the peak load decreased to 4370 lb (63% lower than maximum load) in the positive direction and 5140 lb (57% lower than the maximum load) in the negative direction. The permanent deformation at the final loading cycle was 3.29 in. Figure 5.2.7 and figure 5.2.8 show plastic hinges at the end of the test. Figure 5.2.9 shows photos of the 4 joints of the frame after the end of the test.

Figure 5.2.7: Plastic Hinge at the top of the southern column

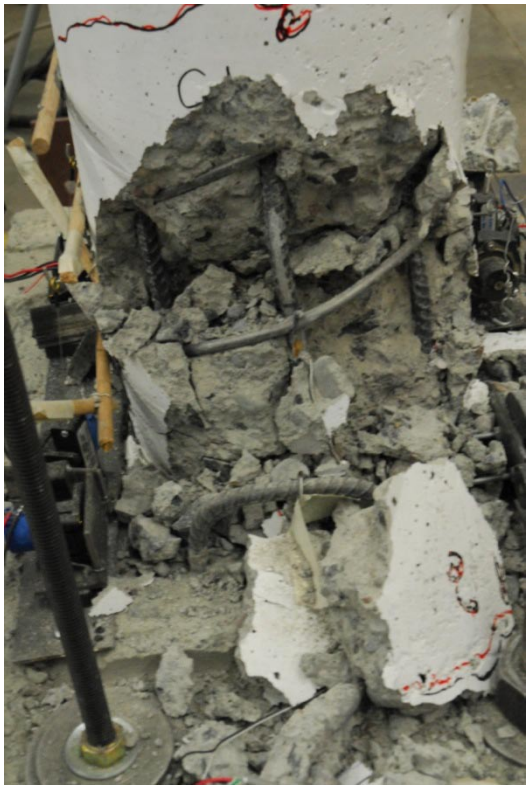

Figure 5.2.8: Plastic hinge at the bottom of the northern column

(a): Bottom of Column N

(b): Top of Column N

(c): Top of Column S

(d): Bottom of Column S

Figure 5.2.9: Joints of specimen F-RC after the end of the test

5.2.2 Specimen F-FRP1

As described in Chapter 3, specimen F-FRP1 had two post-tensioned columns which were 45 in. long and 8 in. diameter FRP tubes filled with concrete, with the target strain for the initial post-tensioning of 0.000935. Figure 5.2.10 shows specimen F-FRP1 during testing.

Figure 5.2.10: Specimen F-FRP1 at the end of the test

Figure 5.2.11 shows the load-displacement hysteresis curve for specimen F-FRP1. Positive displacements indicate displacement to the "North" direction of the specimen.

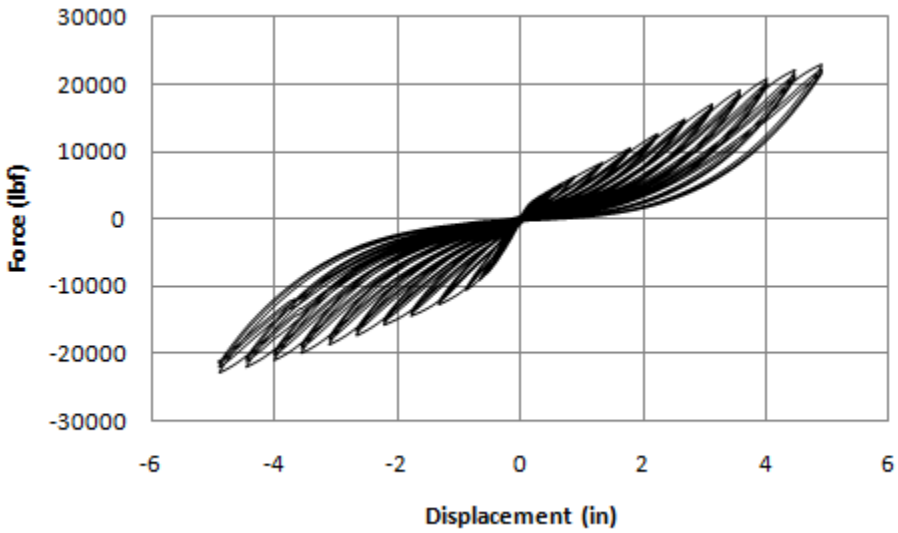

Figure 5.2.11: Specimen F-FRP1 Load-Displacement Hysteresis Curve

The maximum load in the positive direction was 23025 lb and it occurred at a displacement of 4.90 in. The maximum load in the negative direction was 22817 lb and it occurred at a displacement of 4.90 in. The difference in the maximum loads is 0.9% which is insignificant. Compared to specimen F-RC, the average of the maximum loads in the two directions is 93% higher. It should be noted that testing specimen F-FRP1 was limited by the length capacity of jack of the hydraulic actuator (10 in.) and not by a drop in the frame's stiffness.

The two columns developed rocking mechanisms while testing. Figure 5.2.12 shows specimen F-FRP1 at maximum lateral displacement where the rocking mechanism is demonstrated. Figure 5.2.13 shows a closer focus at the northern column undergoing rocking mechanism.

Figure 5.2.12: Specimen F-FRP1 at maximum displacement

Figure 5.2.13: Northern column of specimen F-FRP1 undergoing rocking mechanism

Gaps opened at the column-base interface as well as the column-beam interface. Figure 5.2.14 shows gaps that developed at the column-beam interface and column-base interface of the north and south columns, respectively, during the 3.8 in. displacement cycle.

(a) Gap at column-beam interface of northern column

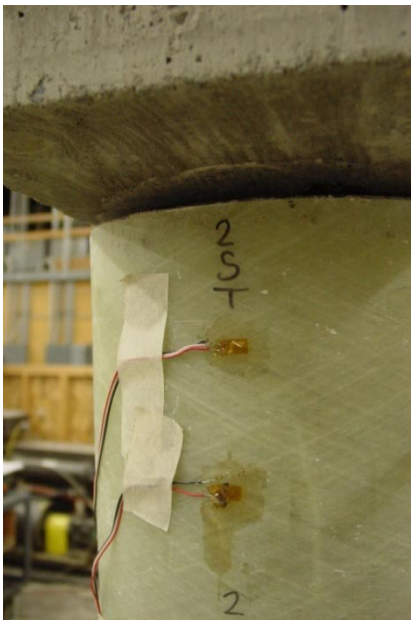

(b) Gap at column-beam interface of southern column

(c) Gap at column-base interface of northern column

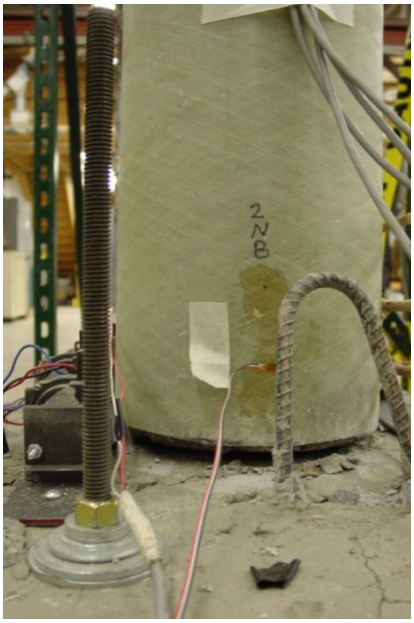

(d) Gap at column-base interface of southern column

Figure 5.2.14: Gaps due to rocking of specimen F-FRP1

The surface of the base was covered with approximately 0.25 in. of mortar to create a flat surface. This layer suffered some cracks by the end of the test, as shown in figure 5.2.14 (c) and (d). As for the columns, neither cracks nor concrete crushing occurred. Due to the presence of the 0.125 in. uncovered extension at the tips of the columns, the FRP tube did not bear against the base or the beam surface during testing, preventing any damage to them. No FRP matrix damage was observed. The permanent deformation at the final loading cycle was 0.56 in. which is 83% less than permanent deformation of specimen F-RC at the final loading cycle. Overall, specimen F-FRP1 showed significantly less damage and permanent deformation than specimen F-RC.

5.2.3 Specimen F-FRP3

Specimen F-FRP3 was similar to specimen F-FRP1 except that each column was formed of three 15 in. long column segments, post-tensioned to the same target initial post-tensioning stress of specimen (steel bar strain = 0.000935). Figure 5.2.15 shows specimen F-FRP3 after testing.

Figure 5.2.15: Specimen F-FRP3 after testing

Figure 5.2.16 shows the load-displacement hysteresis curve for specimen F-FRP3. Positive displacements indicate displacement to the “North” direction of the specimen.

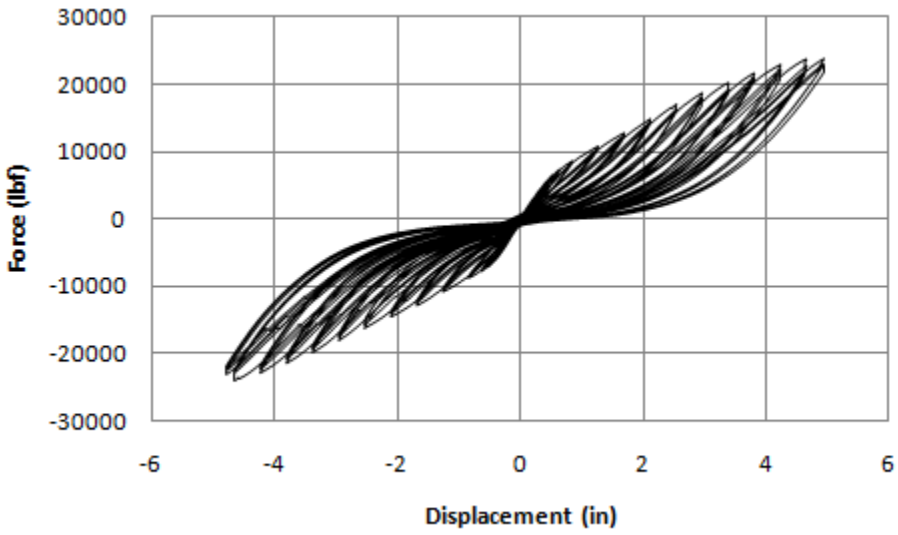

Figure 5.2.16: Specimen F-FRP3 Load-Displacement Hysteresis Curve

The maximum load in the positive direction was 23931 lb and occurred at a displacement level of 4.95 in. The maximum load in the negative direction was 23932 lb and occurred at a displacement level of 4.66 in. The average of the maximum loads of specimen F-FRP3 was higher than that of specimen F-RC by 101%. Compared to specimen F-FRP1, the average of the maximum loads in the two directions for specimen F-FRP3 is 4% higher. Although the peak loads in the positive directions continued to rise at successive displacement levels, the peak loads in the negative direction slightly dropped after the 4.66 in displacement level; reaching 22985 lb at the first loading cycle of the final displacement level, a drop of 4%. It should be noted that as with specimen F-FRP1, testing specimen F-FRP3 was limited by the stroke length of the jack of the hydraulic actuator (±5 in.).

The rocking mechanism occurred at the column-base interfaces as well as at the column-beam interfaces, but not at the column segment-segment interface. Figure 5.2.17 shows specimen F-FRP3 at the maximum lateral displacement where gaps opened at the base and top of the

columns due to rocking mechanism. Figure 5.2.18 shows a more focused view at the northern and southern columns undergoing the rocking mechanism at maximum displacement.

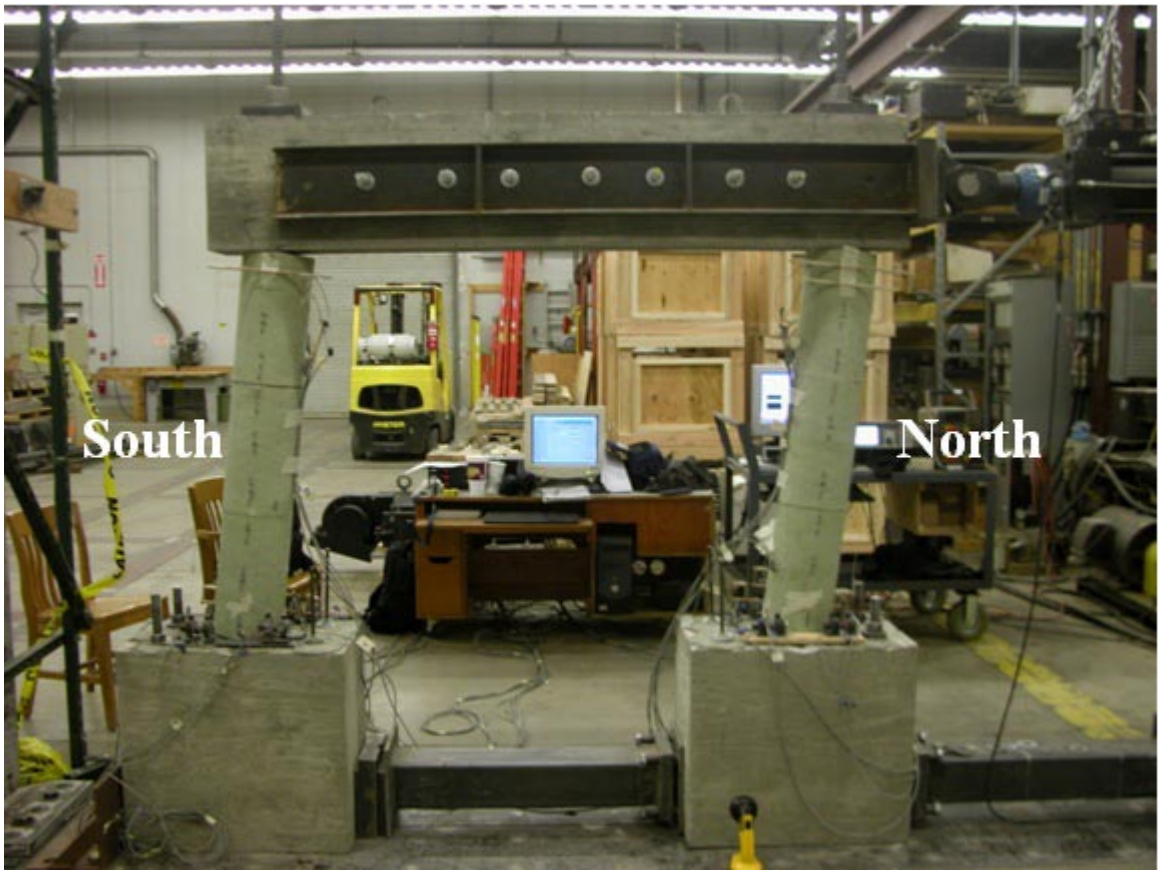

Figure 5.2.17: Specimen F-FRP3 at maximum displacement

(a) Northern column

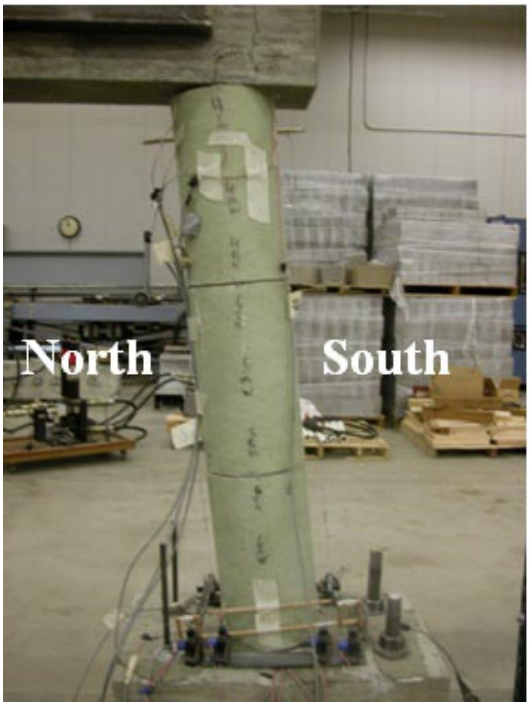

(b) Southern column

Figure 5.2.18: Rocking of the columns of specimens F-FRP3 at maximum displacement

Figure 5.2.19 shows gaps that developed as a result of rocking at the column-beam and column-base interfaces of the north and south columns during the 3.8 in. displacement cycle. The gaps at the column-beam interface opened to a length up to 7/8 in., where as the gaps at the column-base interface opened to a length of 5/8 in.

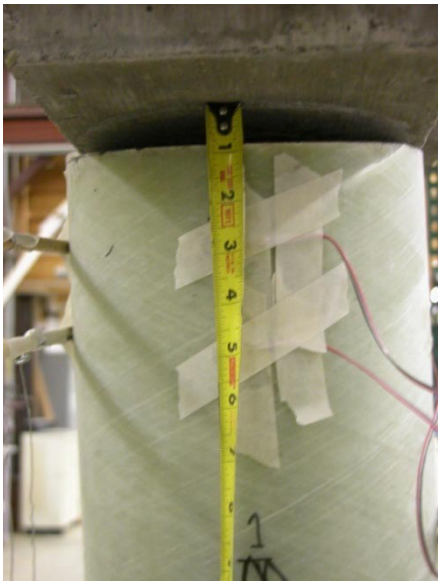

(a) Gap at column-beam interface of northern column

(b) Gap at column-beam interface of southern column

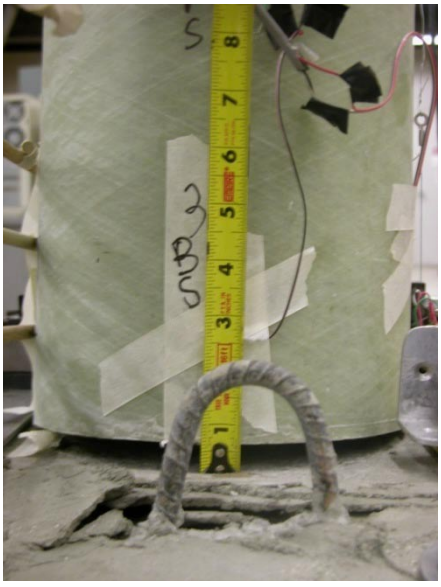

(c) Gap at column-base interface of northern column

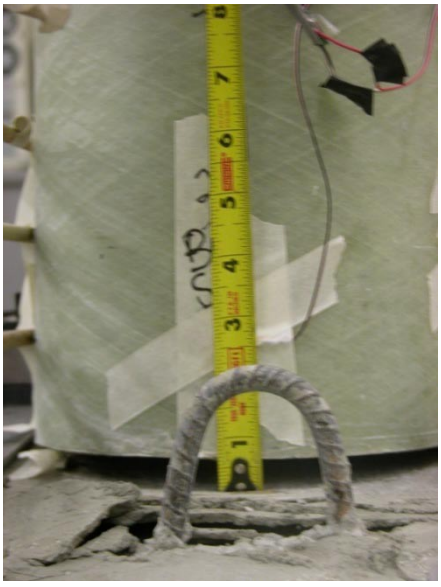

(d) Gap at column-base interface of northern column

Figure 5.2.19: Gaps due to rocking of specimen F-FRP3

The grout layer above the foundation suffered some cracks by the end of the test, as shown in figure 5.2.19 (c) and (d). Due to the absence of the 0.125 in. uncovered extension at the tips of the columns, the FRP tube was locally damaged at the location of contact with the beam surface during testing. A crack about 2 in. long appeared at the FRP tube of the top segment as shown in Figure 5.2.20 (a). Figure 5.2.20 (b) shows damage to the FRP tube at the column-beam interface of the northern column. The permanent deformation at the final loading cycle was 0.72 in. which compared to specimen F-RC is 78% less, and compared to specimen F-FRP1 is 29% higher. For all the columns' segments, no concrete crushing occurred at any point of the test. Overall, specimen F-FRP1 showed significantly less damage and permanent deformation than specimen F-RC, which was similar to the behavior of specimen F-FRP1.

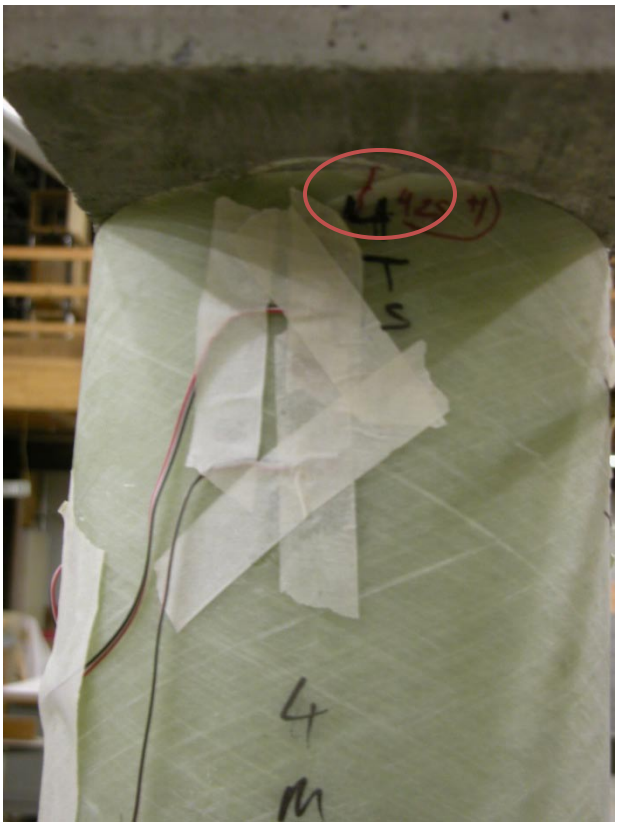

Figure 5.2.20 (a): Damage to FRP tube of specimen F-FRP3 (including crack) at column beam-interface of southern column during the 4.25 in. displacement cycle

Figure 5.2.20 (b): Damage to FRP tube of specimen F-FRP3 at column beam-interface of northern column

5.2.4 Specimen F-FRP3-R

Specimen F-FRP3-R was similar to specimen F-FRP3, but with rubber pads installed at the column-beam interfaces as well as at the column-base interfaces. Each rubber pad was 0.5 in. thick, and two pads were used at each of the interfaces. The target post-tensioning stress for specimen F-FRP3-R was the same as that of specimen F-FRP1 and F-FRP3 (steel bar strain = 0.000935). Figure 5.2.21 shows specimen F-FRP3-R at the end of the test.

Figure 5.2.21: Specimen F-FRP3-R at the end of the test

Figure 5.2.22 shows the load-displacement hysteresis curve for specimen F-FRP3-R. Positive displacements indicate displacement to the “North” direction of the specimen.

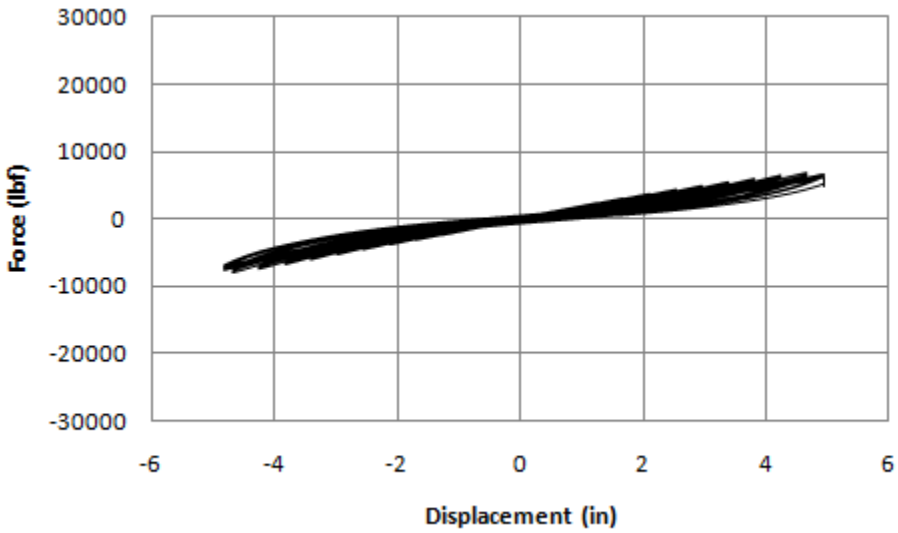

Figure 5.2.22: Specimen F-FRP3-R Load-Displacement Hysteresis Curve

The maximum load in the positive direction was 6813 lb and occurred at a displacement level of 4.67 in. The maximum load in the negative direction was 7939 lb and occurred at a displacement level of 4.67 in. The average of the maximum loads of specimen F-FRP3-R was lower than that of specimen F-RC by 38%. Compared to specimen F-FRP1, the average of the maximum loads in the two directions for specimen F-FRP3 is 69% lower. The peak load at the final loading cycle dropped 10% below the maximum load.

The rocking mechanism did not occur at any column segment-segment interface. The two columns rotated as a whole at the column-beam interface as well as at the column-base interface by compressing the rubber pads present at those interfaces. No gap openings appeared. Figure 5.2.23 shows specimen F-FRP3-R at 4.25 in. displacement where the rocking mechanism is demonstrated. Figure 5.2.24 shows a closer view at the upper column segment of the northern column of specimen F-FRP3-R undergoing rocking mechanism at maximum displacement.

Figure 5.2.23: Specimen F-FRP3-R at 4.25 in. displacement

Figure 5.2.24: Upper column segment of the northern column of specimen F-FRP3-R at maximum displacement

Due to the presence of the rubber pads at the column-base interface, no damage occurred to the grout layer above the foundation.

The column segments of specimen F-FRP3-R were not covered completely with FRP tubes. As with specimen F-FRP1, the column segments of specimen F-FRP3-R had 0.125 in. uncovered extension at the tips of the columns. Due to the presence of those extensions, the FRP tubes suffered no damage.

The permanent deformation at the final loading cycle was 0.92 in. which compared to specimen F-RC is 72% less, compared to specimen F-FRP1 is 64% higher, and compared to specimen F-FRP3 is 28% higher. For all the column segments, no concrete crushing occurred at any point of the test. Some minor rupture occurred to some of the rubber pads; however, this may have happened during the post-tensioning process. Overall, specimen F-FRP1 showed significantly less damage and permanent deformation compared to specimen F-RC, which was similar to the behavior of specimen F-FRP1 and specimen F-FRP3.

5.2.5 Specimen F-FRP3-S

Specimen F-FRP3-S had external energy dissipaters in the form of four steel angles that were modified and attached at alternating corners as described in Chapter 3. With that layout, and when the specimen is displaced in the negative direction (south), the energy dissipation devices attached to the northern column are in tension and therefore dissipate energy by yielding; while the energy dissipating devices attached to the southern column will be under compression, and could therefore buckle. The opposite phenomenon occurs when displacing the specimen in the

positive direction (north). Steel yielding by tension dissipates a relatively larger amount of energy than buckling. Therefore, the northern column dissipates more energy when the specimen is loaded in the negative direction (south), while the southern column dissipates more energy when the specimen is displaced in the positive direction (north).

The target post-tensioning stress for specimen F-FRP3-R was the same as that of specimen F-FRP1, F-FRP3, and F-FRP3-R (steel bar strain = 0.000935). Figure 5.2.25 shows specimen F-FRP3-S after testing.

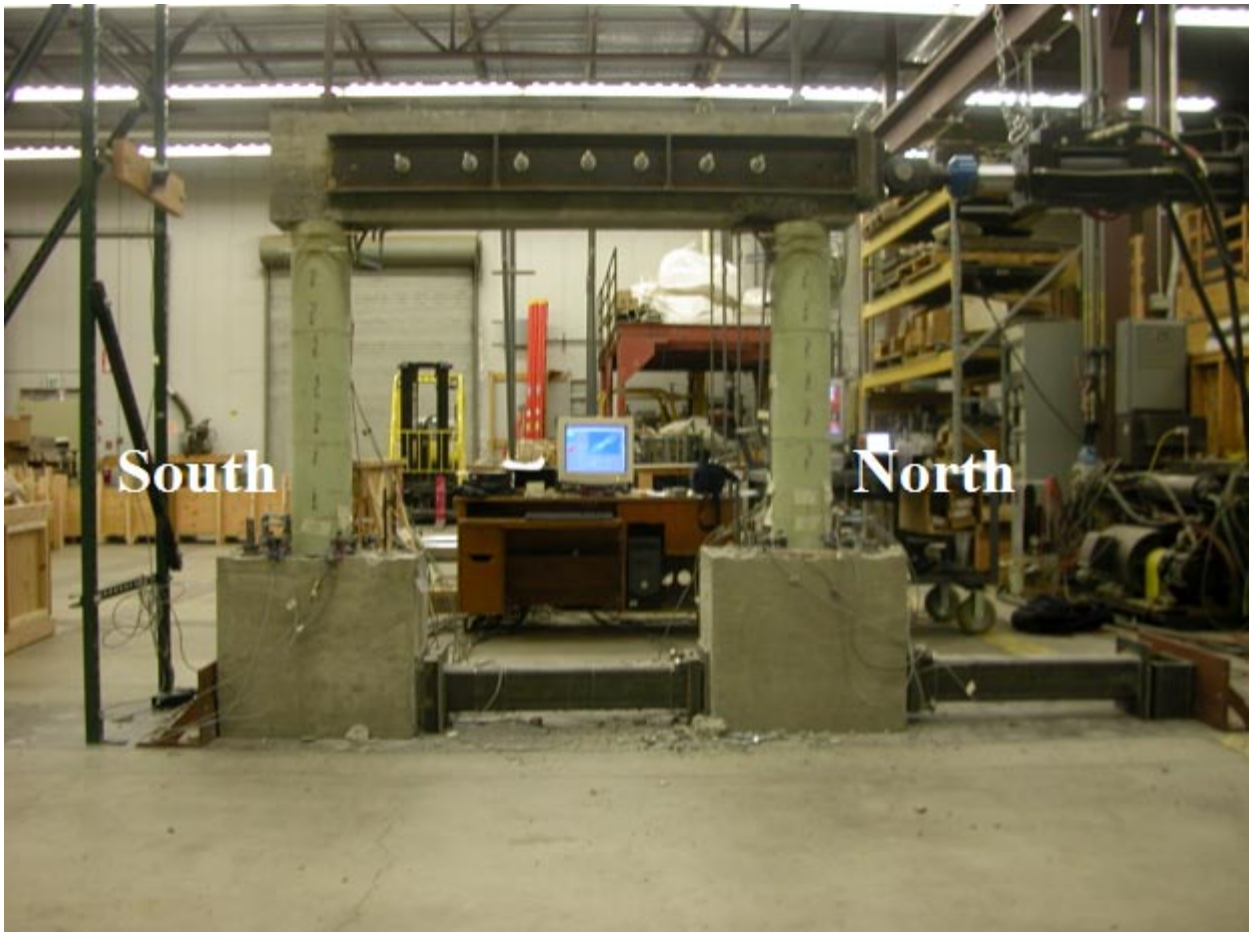

Figure 5.2.25: Specimen F-FRP3-S after testing

Figure 5.2.26 shows the load-displacement hysteresis curve for specimen F-FRP3-S. Positive displacements indicate displacement to the "North" direction of the specimen.

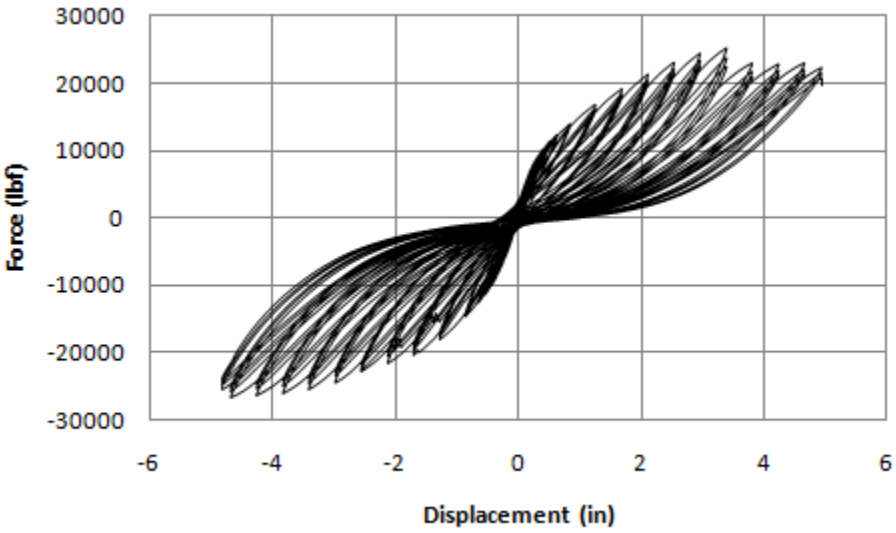

Figure 5.2.26: Specimen F-FRP3-S Load-Displacement Hysteresis Curve

The maximum load in the positive direction was 25205 lb and occurred at a displacement level of 3.34 in. The maximum load in the negative direction was 26647 lb and occurred at a displacement level of 4.66 in. The average of the maximum loads of specimen F-FRP3-R was higher than that of all the other four specimens: specimen F-RC by 118%, specimen F-FRP1 by 13%, specimen F-FRP3 by 8%, and specimen F-FRP3-R by 251%.

Each modified steel angle was fixed into position using five bolts: two planted in the column and three planted into the beam or the base depending on the location of the angle (as explained in chapter 3). However, the angle at the northern corner of the beam was fixed into position with 2 bolts in the beam instead of 3. The reason was the presence of a stirrup that was disoriented while pouring concrete blocking the location of the third bolt.

Cracks (45 degrees) began to appear at the bottom surface of the beam near the anchor bolts while specimen F-FRP3-S was being loaded at the first loading cycle during the 2.12 in. displacement level. Figure 5.2.27 shows the cracks that developed at the northern and southern corners by the end of the first cycle of the 2.12 in. displacement level.

(a) Northern corner (b) Southern corner

Figure 5.2.27: Cracks developing at the corners of the beam of specimen F-FRP3-S after the first cycle of the 2.12 in. displacement level.

By the end of the third cycle of the 2.12 in. displacement level, the cracks at the northern corner of the beam increased in length and thickness, and the concrete cover appeared to begin spalling, as shown in figure 5.2.28, which later developed to pull-out failure.

Figure 5.2.28: Concrete began to spall at the northern corner of the beam of specimen F-FRP3-S after the 3rd cycle of the 2.12 in. displacement level

By the end of the 3.40 in. displacement level, the volume of concrete in the beam holding the two bolts fixing the angle at the northern corner of the beam spalled, the two bolts were pulled out of position, and the longitudinal reinforcement of the beam became visible as shown in figure 5.2.29. Due to the spalling of concrete at the location of the angle fixed to the northern corner of the beam of specimen F-FRP3-S, the stiffness of the frame when displaced in the positive direction (north) suddenly dropped 9% as seen in figure 5.2.26. The peak load at the 3.40 in. displacement level was 25205 lb, while the peak load at the 3.82 in. displacement level was 22952 lb.

Figure 5.2.29: Pull-out of concrete surrounding the bolts fixing the northern modified steel angle to the beam at the 3.40 in. displacement cycle

By the end of the 3.80 in. displacement level, bolts fixing the sacrificial steel angles to the column segments began to get pulled out of position. A crack appeared in the FRP tube of the upper as well as the lower column-segment of the southern column of specimen F-FRP3-S at the location of the bolt holes as they were being pulled out during the second cycle of the 3.80 in. displacement level; as shown in figure 5.2.30. Figure 5.2.31 shows the bolts fixing the angle to the lower column-segment of the northern column of specimen F-FRP3-S as they were pulled out of position after the 3.80 in. displacement level.

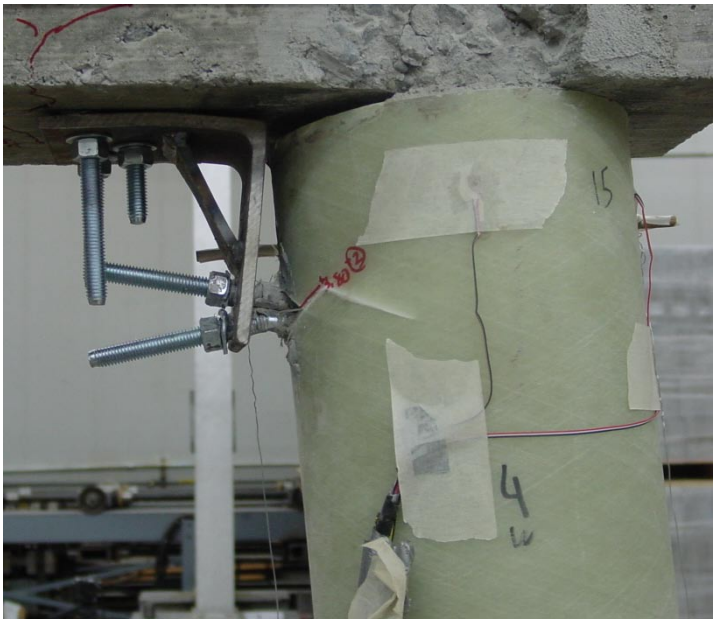

Figure 5.2.30 (a): Crack appeared at FRP tube as bolts fixing the steel angle to the upper column-segment of southern column of specimen F-FRP3-S were pulled out of position after 3.80 in. displacement level

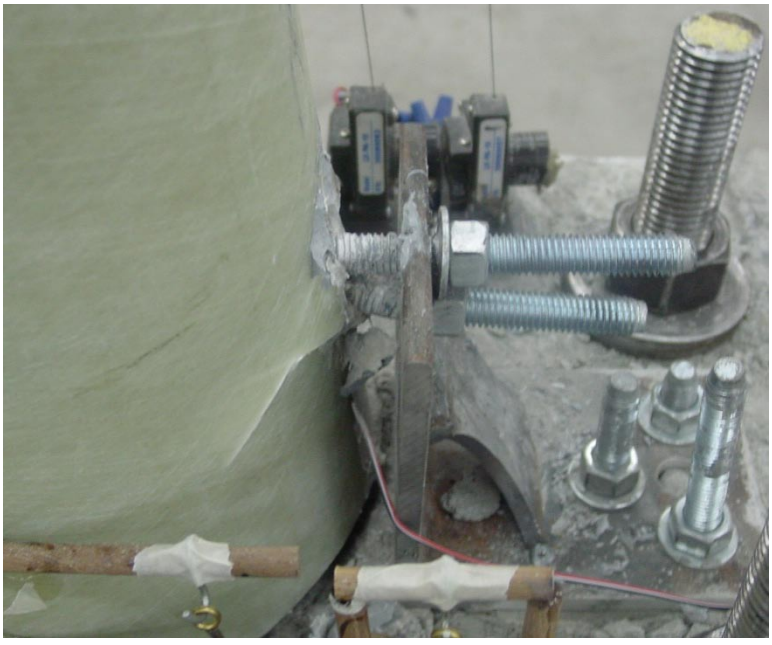

Figure 5.2.30 (b): Crack appeared at FRP tube as bolts fixing the steel angle to the lower column-segment of southern column of specimen F-FRP3-S were pulled out of position after 3.80 in. displacement level

Figure 5.2.31: Bolts fixing angles to lower column-segment of northern column of specimen F-FRP3-S pulled out of position after 3.80 in. displacement level

The rocking mechanism occurred at column-base interfaces as well as column-beam interfaces, but not at column segment-segment interfaces. Figure 5.2.32 shows the upper segments of the northern and southern columns of specimen F-FRP3-S undergoing rocking mechanism during the final loading cycle. Figure 5.2.33 shows the gaps opening at the column-beam and column-base interfaces of the northern and southern columns of specimen F-FRP3-S at maximum displacement (4.95 in.). As a result of rocking, the angles deformed and did not maintain their characteristic right angles. Figure 5.2.34 shows the deformation of the angle at the upper column-segment of the northern column (which was disconnected from the beam as described previously).

(a): Upper column-segment of northern column

(b) Upper column-segment of southern

Figure 5.2.32: Specimen F-FRP3-S undergoing rocking mechanism at maximum displacement (4.95 in.)

(a) Column-beam interface of northern column

(b) Column-base interface of northern column

(c) Column-beam interface of southern column

(d) Column-base interface of southern column

Figure 5.2.33: Gaps at interfaces of specimen F-FRP3-S while rocking at maximum displacement

Figure 5.2.34: Gap opening between steel angle and beam bottom surface at the north corner of the beam during maximum displacement

The peak load at the final loading cycle dropped 18% below the maximum load. The permanent deformation at the final loading cycle was 0.99 in, which is higher than the permanent deformation of all the other FRP specimens. Compared to specimen F-RC, the permanent deformation of specimen F-FRP3-S at the final loading cycle is 70% lower; compared to specimen F-FRP1 is 77% higher, compared to specimen F-FRP3 is 38% higher, and compared to specimen F-FRP3-R is 8% higher. It should be noted that, as with specimens F-FRP1 and F-

FRP3, testing specimen F-FRP3-S was limited by the length capacity of jack of the hydraulic actuator (10 in.).

5.3 Backbone Curves

The backbone curves of the five specimens were constructed by graphing the peak load in each displacement level (ordinate) against the corresponding drift value (abscissa). Figure 5.3.1 shows the backbone curves of the five specimens.

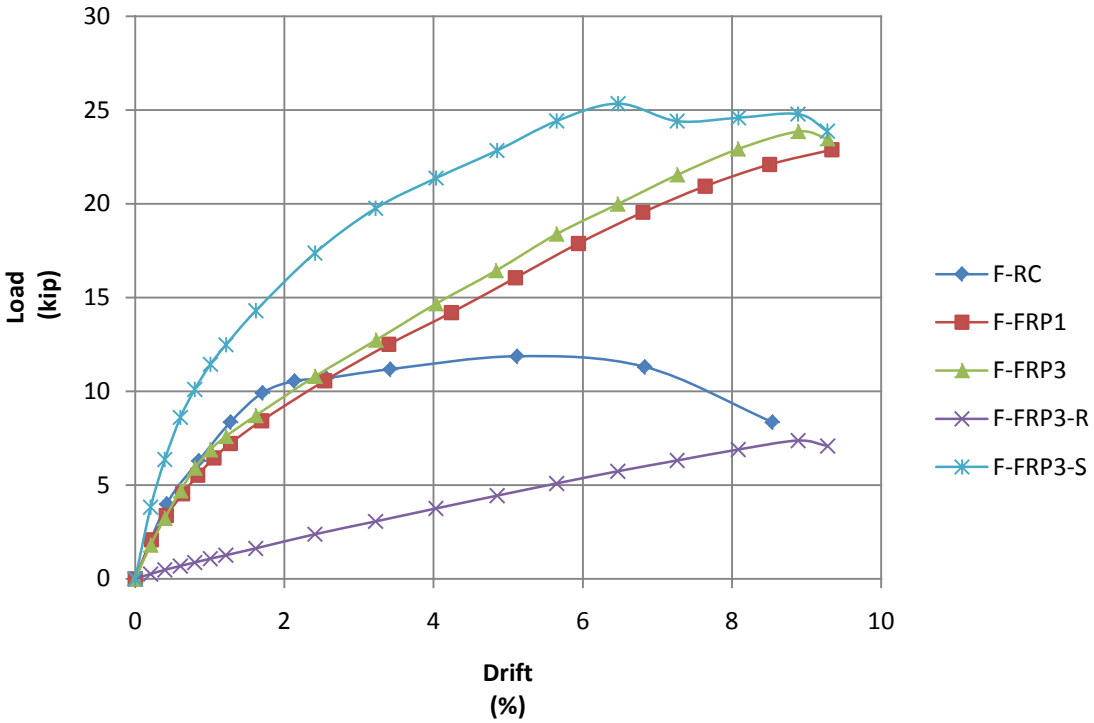

Figure 5.3.1: Backbone curves showing drift vs. load

The initial response of specimens F-RC, F-FRP1, and F-FRP3 was similar up to a drift of about 1.1%. Specimen F-RC yielded at a load of 10 kips and a drift ratio of 1.8% and began to fail after reaching a load of 11.9 kips at a drift of 5%.

Specimen F-FRP1 was losing stiffness from the beginning of the test until reaching a load of 7.2 kips at a drift of 1.2% where the behavior began to follow a linear fashion reaching a maximum load of 22.9 kips at a drift ratio of 9.3% which was the stroke length of the hydraulic actuator. The response of specimen F-FRP3 was similar to the response of specimen F-FRP1, but with 5% higher loads at similar drift ratios. The specimen was losing stiffness from the beginning of the test until reaching a load of 7.6 kips at a drift ratio of 1.2%. The response followed a linear behavior following that, reaching a maximum load of 23.9 kips at a drift ratio of 8.9%, where the load dropped as a result of the loss of stiffness, reaching a load of 23.5 kips at a drift ratio of 9.3%.

Specimen F-FRP3-R followed a linear response from the beginning of the test until reaching a maximum load of 7.4 kips at a drift ratio of 8.9%. Following that point, the stiffness dropped and the load decreased 4% reaching 7.1 kips at a drift of 9.3%.

Specimen F-FRP3-S was losing stiffness throughout the test, leading to a response of a logarithmic form. The failure of the steel angle at the north corner of the beam after the 3.4 in displacement level (described with more details in section 5.2.5) led to a sudden drop of 3.7% in the frame resistance from the maximum load of 25.3 kips at a drift of 6.5% to a load of 24.4 kips at a drift of 7.3%. After that stage, the loads continued to rise as the drift increased, reaching a

load of 24.8 kips (an increase of 1.5%) at a drift of 8.9%. The load dropped again at the final displacement level, decreasing 3.7% from the previous displacement level, reaching a value of 23.9 kips at a drift of 9.3%.

The loss of stiffness can be explained by the decrease in the post-tensioning stress which is a result of losses due to micro-cracks in concrete, shortening of the columns due to permanent expansion in the radial direction as a result of Poisson's effect, and possibly by the permanent elongation of the post-tensioning due to yielding which occurred in specimen F-FRP3-S.

5.4 Stiffness

As mentioned is the previous section, all of the specimens were losing stiffness as the displacement level was increasing. To observe this phenomenon in a more detailed manner, secant stiffness curves were constructed for the five specimens. Figure 5.4.1 shows the secant stiffness curves.

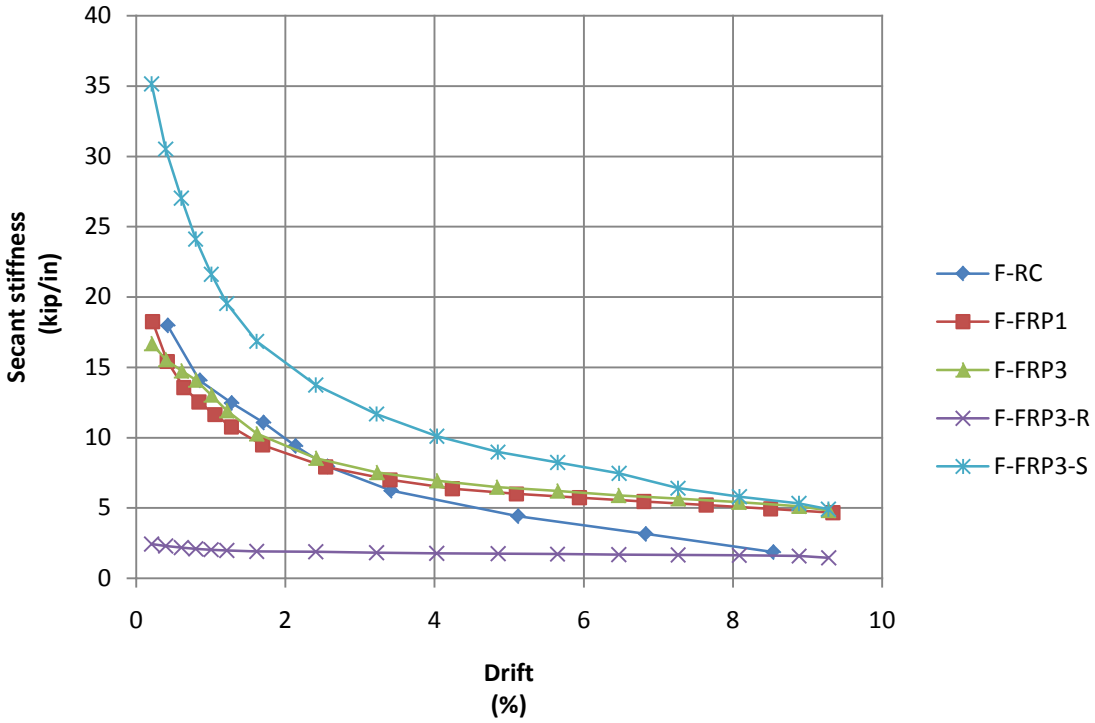

Figure 5.4.1: Secant stiffness curves

Initial stiffness values of specimens F-RC, F-FRP1, and F-FRP3 were relatively close in magnitude. The initial stiffness of specimen F-RC was 15.4 kip/in, of specimen F-FRP1 was 18.3 kip/in, and of specimen F-FRP3 was 16.7 kip/in. Specimen F-FRP3-S had the highest initial stiffness, 35.1 kip/in, whereas specimen F-FRP3-R had the lowest initial stiffness, 2.4 kip/in. Comparing the initial stiffness values to that of specimen F-RC; specimen F-FRP1 was 1.6% higher, specimen F-FRP3 was 7.1% lower, specimen F-FRP3-R was 86.5% lower, and specimen F-FRP3-S was 95% higher.

The stiffness values of specimens F-RC, F-FRP1, F-FRP3, and F-FRP3-S dropped significantly by the end of the test, whereas the stiffness values of specimen F-FRP3-R had an almost constant stiffness throughout the test. The values of the final stiffness of specimens F-FRP1, F-FRP3, and F-FRP3-S were relatively close in magnitude, while the final stiffness of specimen F-RC

dropped to a value relatively close to that of specimen F-FRP3-R, which is significantly lower than the final stiffness values of the other three specimens. The final stiffness of specimen F-RC was 1.9 kip/in, that of specimen F-FRP1 was 4.7 kip/in, that of specimen F-FRP3 was 4.8 kip/in, that of specimen F-FRP3-R was 1.5 kip/in, and that of specimen F-FRP3-S was 4.9 kip/in. Compared to specimen F-RC, the final stiffness of specimen F-FRP1 was 150% higher, that of specimen F-FRP3 was 158% higher, that of specimen F-FRP3-R was 22% lower, and that of specimen F-FRP3-S was 163% higher.

To have a more representative comparison of the drop in stiffness of the five specimens throughout the test when compared to the initial stiffness of each specimen on its own, the normalized secant stiffness was calculated, and a graph of drift vs. the normalized secant stiffness of the five specimens was constructed and is shown in figure 5.4.2. The normalized secant stiffness was computed by calculating the ratio of the current secant stiffness to the initial secant stiffness of each specimen.

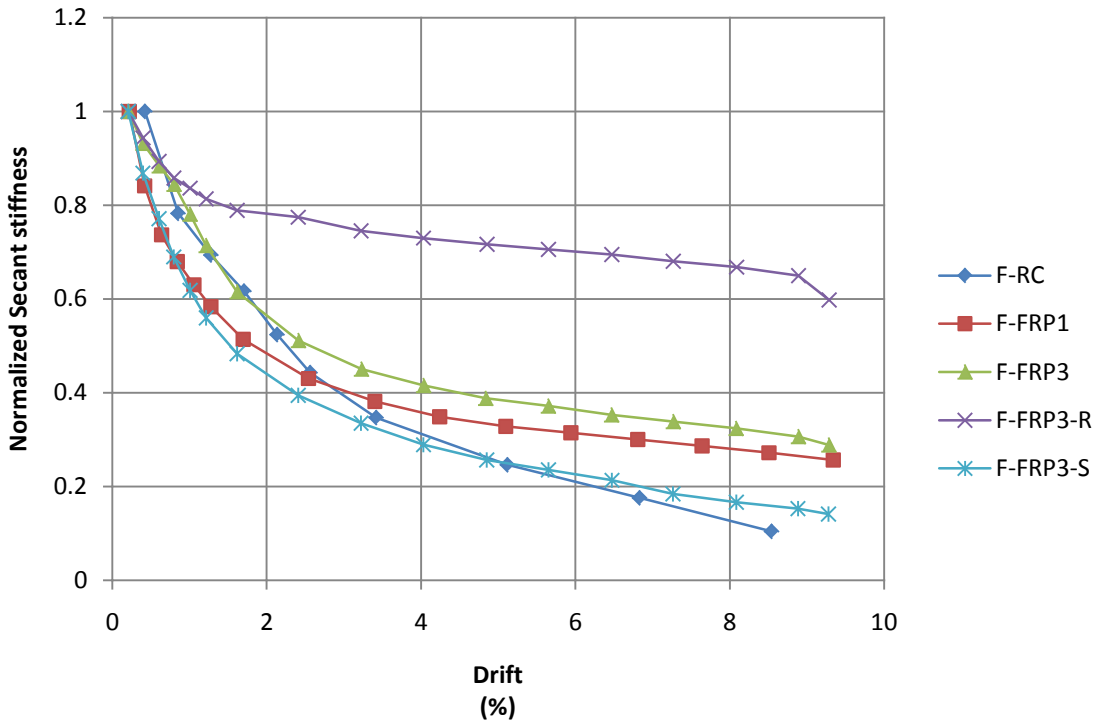

Figure 5.4.2: Drift vs. Normalized secant stiffness

Specimen F-RC had the greatest drop of stiffness, 89.6%. The drop in stiffness of specimens F-FRP1, F-FRP3, F-FRP3-R, and F-FRP3-S were 74.4%, 71.2%, 40.2%, and 85.9%, respectively. Specimen F-FRP3-R had the lowest drop in stiffness.

5.5 Energy dissipation

Comparison of energy dissipation among the five specimens was one of the significant objectives of this study. To quantify energy dissipation, the area inside each loop of the load-displacement hysteresis curves was calculated, which reflects the energy dissipated at that specific loading cycle. To better compare the response of the five specimens, the cumulative

energy dissipated had to be computed. This was calculated by summing up the areas of all the loops in the load-displacement hysteresis curve. Figure 5.5.1 shows drift against cumulative energy dissipated in the first cycle of each drift level.

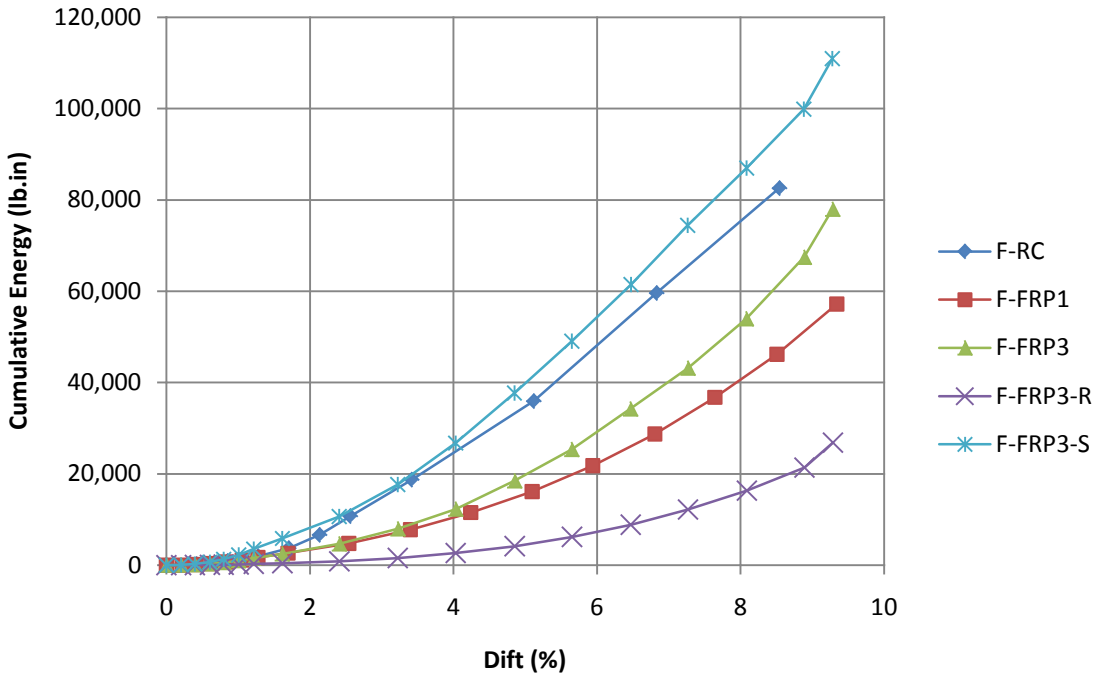

Figure 5.5.1: Drift vs. cumulative energy dissipated in the 1st cycle

All of the five specimens dissipated energy. Specimen F-FRP3-S dissipated the highest total amount of energy, due to permanent deformation in the form of yielding of the sacrificial external steel angles, which is the objective of creating this specimen. As expected, Specimen F-RC had the next highest total energy dissipated, followed by specimen F-FRP3, F-FRP1, and F-FRP3-R. Specimen F-RC dissipated energy due to concrete cover spalling, concrete crushing,

and rebar yielding. Specimens F-FRP1 and F-FRP3 dissipated energy by rocking, micro-cracking and creep of concrete. Specimen F-FRP3 dissipated more energy than specimen F-FRP1 due to the higher number of segments which created more rocking interfaces. Specimen F-FRP3-R was the least to dissipate energy due to the lack of damage or rocking occurance due to the presence of the rubber layers at the interfaces stated previously.

The total amount of energy dissipated by specimen F-RC was 211.1 kip.in., that by specimen F-FRP1 was 119.8 kip.in., that by specimen F-FRP3 was 198.5 kip.in., that by specimen F-FRP3-R was 79.1 kip.in., and that by specimen F-FRP3-S was 299.0 kip.in. Compared to specimen F-RC, the cumulative energy dissipated by specimen F-FRP1 was 43.3% lower, specimen F-FRP3 was 5.9% lower, specimen F-FRP3-R was 62.5% lower, and specimen F-FRP3-S was 41.7% higher. The amount of energy dissipated for each specimen depended primarily on two factors: the drift level and the cycle number of each drift level. Generally, as the drift level increases, the amount of energy dissipated also increases. Given that for each drift level of loading there are three loading cycles; the first cycle of loading dissipates the most amount of energy, followed by the second and third cycle, respectively. However, specimen F-FRP3-R had almost equal magnitudes of energy dissipated in the three loading cycles, as shown in figure 5.5.5. Figures 5.5.2 to 5.5.6 show a comparison of the amount of energy dissipated in each loading cycle for each of the five specimens: F-RC, F-FRP1, F-FRP3, F-FRP3-R, and F-FRP3-S, respectively.

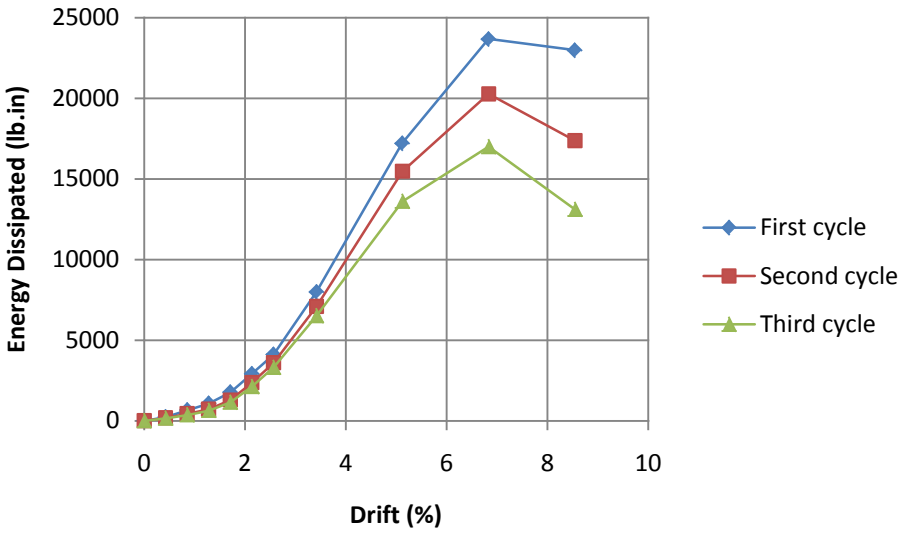

Figure 5.5.2: Energy Dissipation of specimen F-RC

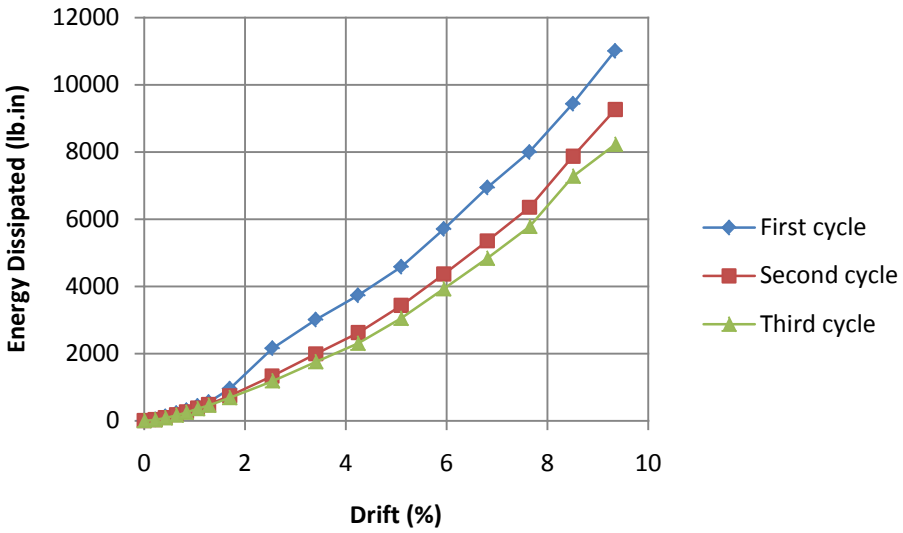

Figure 5.5.3: Energy Dissipation of specimen F-FRP1

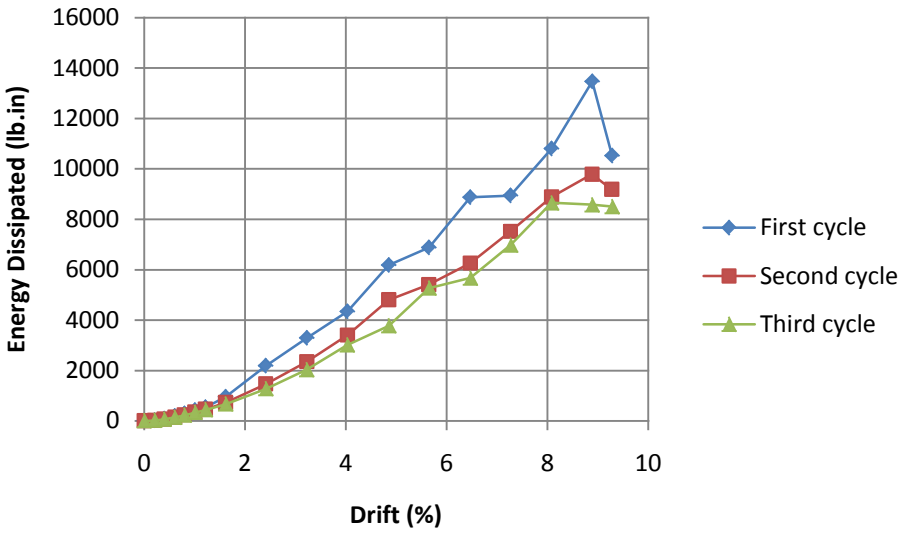

Figure 5.5.4: Energy Dissipation of specimen F-FRP3

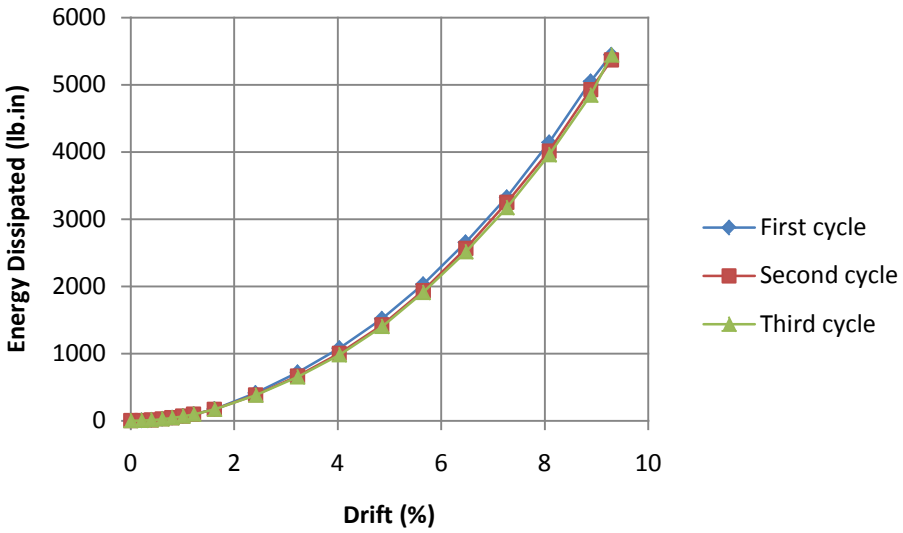

Figure 5.5.5: Energy Dissipation of specimen F-FRP3-R

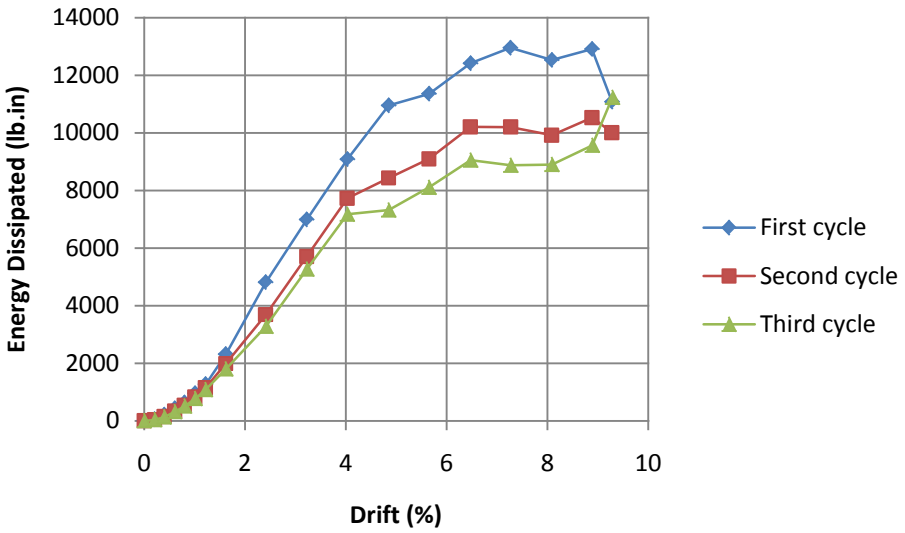

Figure 5.5.6: Energy Dissipation of specimen F-FRP3-S

Using the values of energy dissipated at the first loading cycle; the maximum amount of energy dissipated by specimen F-RC occurred at a drift of 6.8%, by specimen F-FRP1 at a drift of 9.3% (maximum drift capacity of the actuator), by specimen F-FRP3 at a drift of 8.9%, by specimen F-FRP3-R at a drift of 9.3% (maximum drift capacity of the actuator), and by specimen F-FRP3-S at a drift of 7.3%.

The average drop in energy dissipated in the second and third loading cycles, respectively, compared to the first loading cycle of specimen F-RC were 20.8% and 31.0%, by specimen F-FRP1 were 22.3% and 29.2%, by specimen F-FRP3 were 21.3% and 27.9%, by specimen F-FRP3-R were 2.7% and 4.0%, and by specimen F-FRP3-S were 18.2% and 24.6%.

Table 5.5.1 shows a summary of the results presented in this section. Table 5.5.2 compares the total amount of energy dissipation in the first, second, and third loading cycles of each of the five specimens. Table 5.5.3 compares the maximum amounts of energy dissipation in the first,

second, and third loading cycles of the five specimens along with their corresponding drift values.

Specimen	Total energy dissipated in 1st cycle (kip.in)	% Difference in total energy dissipated compared to F-RC	Average drop in energy dissipation of 2nd cycle compared to 1st cycle (%)	Average drop in energy dissipation of 3rd cycle compared to 1st cycle (%)
F-RC	82.6	N/A	20.8	31.0
F-FRP1	57.2	- 43.3	22.3	29.2
F-FRP3	78.0	- 5.9	21.7	27.9
F-FRP3-R	26.8	- 62.5	2.7	4.0
F-FRP3-S	110.9	+ 41.7	18.2	24.6

Table 5.5.1: Comparison of total energy dissipated of specimens and average drop of energy dissipated in 2nd and 3rd loading cycles

5.6 Equivalent viscous damping

The ability of a specimen to dissipate energy can be reflected by calculating the equivalent viscous damping, which was calculated for each specimen at all displacement levels. The equivalent viscous damping was calculated by equation 5.6.1 (Blandon & Priestley, 2005):

$$\zeta_{eq} = \frac{A_{hyst}}{2\pi F_0 u_0} \qquad \text{(Equation 5.6.1)}$$

where:

- ζ_{eq} : equivalent viscous damping
- A_{hyst} : area enclosed one load-displacement hysteresis loop
- F_0 : average peak force during the specific cycle

- u_0 : average peak displacement during the specific cycle

Figure 5.6.1 shows the equivalent viscous damping of the five specimens.

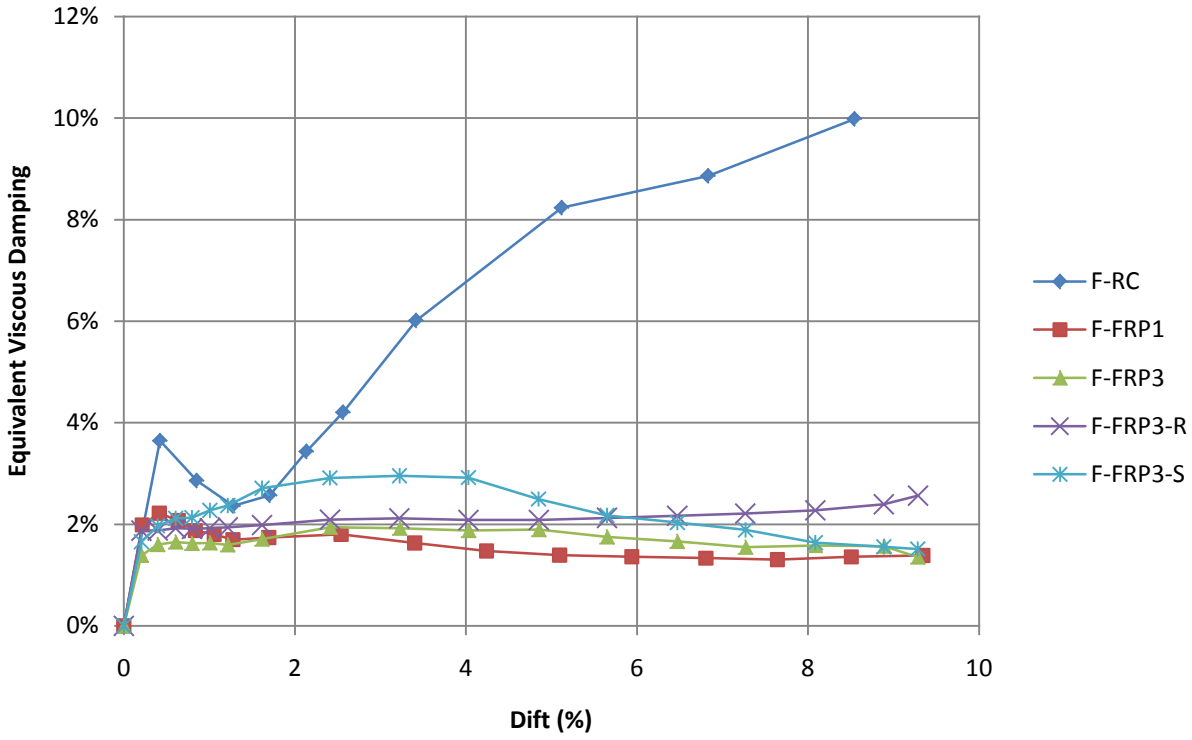

Figure 5.6.1: Drift vs, equivalent viscous damping

The equivalent viscous damping values ζ_{eq} of all specimens were almost equal from the beginning of the tests up to a drift of 0.2%. Specimen F-RC then had the maximum equivalent viscous damping ζ_{eq} throughout the test. However, the values of ζ_{eq} for specimen F-RC were close to those of specimen F-FRP3-S from a drift of 1.3% where the ζ_{eq} for specimen F-RC as well as F-FRP3-S was 0.024, until a drift of 1.6% where the ζ_{eq} of specimen F-RC was 0.026 and the ζ_{eq} of specimen F-FRP3-S was 0.027. Specimen F-FRP3-S had the second highest ζ_{eq} after F-RC until a drift of 6%. After that, the ζ_{eq} of specimen F-FRP3-R had a higher value until the end

of the test. Specimens F-FRP1, F-FRP3, and F-FRP3-R had relatively close values of ζ_{eq} throughout the test, with specimen F-FRP3-R having the second highest ζ_{eq} among the five specimens at the end of the test: 0.0256 at a drift of 9.3%. Table 5.6.1 summarizes the ζ_{eq} results of the five specimens, showing the maximum, minimum (excluding initial value), and final equivalent viscous damping values along with their corresponding drift values.

Specimen	**Maximum Equivalent Viscous Damping**		**Minimum Equivalent Viscous Damping** (excluding initial value)		**Equivalent Viscous Damping at final drift level**	
	Drift (%)	ζ_{eq}	Drift (%)	ζ_{eq}	Drift (%)	ζ_{eq}
F-RC	8.5	0.0998	1.3	0.0236	8.5	0.0998
F-FRP1	0.4	0.0222	7.6	0.0131	9.3	0.0139
F-FRP3	2.4	0.0194	9.3	0.0136	9.3	0.0136
F-FRP3-R	9.3	0.0256	0.2	0.0187	9.3	0.0256
F-FRP3-S	3.2	0.0295	9.3	0.0151	9,3	0.0151

Table 5.6.1: Maximum, minimum (excluding initial value), and final EVD values with corresponding drift

5.7 Post-tensioning steel-bar strain

The steel bars in specimens F-FRP1, F-FRP3, F-FRP3-R, and F-FRP3-S underwent two stages of loading. The first stage was post-tensioning and the second stage was testing of the specimen. The following sub-sections describe results of the two stages with more details.

5.7.1 Bar stress while post-tensioning

As discussed in chapter 4, the initial post-tensioning value determines the yielding moment of the post-tensioned column. Each bar was equipped with strain gages to monitor the bar stress

while post-tensioning. The theoretical initial post-tensioning strain was determined using the procedure described in chapter 4, and was calculated to be 935 micro-strain. Figures 5.7.1 to 5.7.4 show the steel-bar strain values of specimens F-FRP1, F-FRP3, F-FRP3-R, and F-FRP3-S respectively, during the process of post-tensioning.

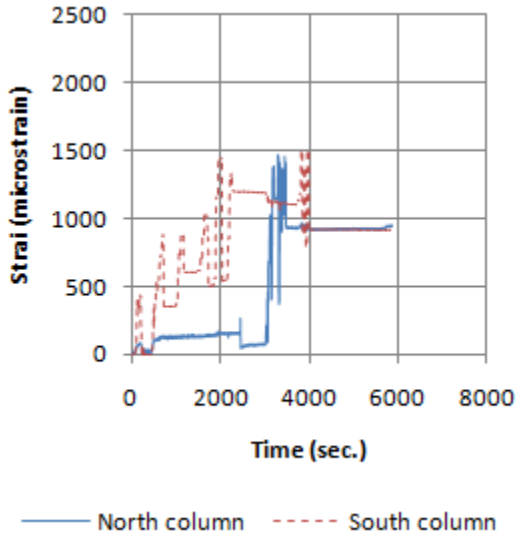

Figure 5.7.1: Post-tensioning specimen F-FRP1

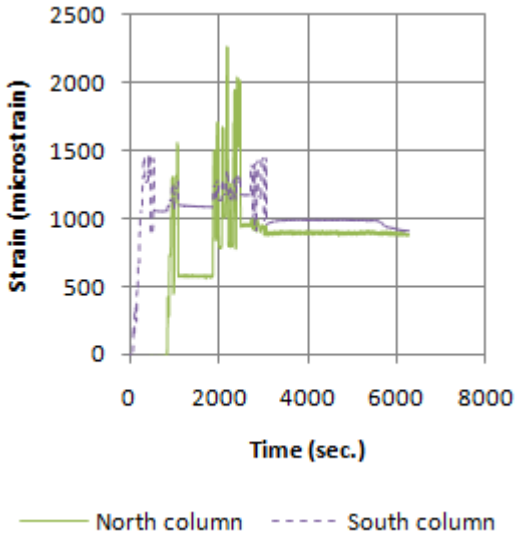

Figure 5.7.2: Post-tensioning specimen F-FRP3

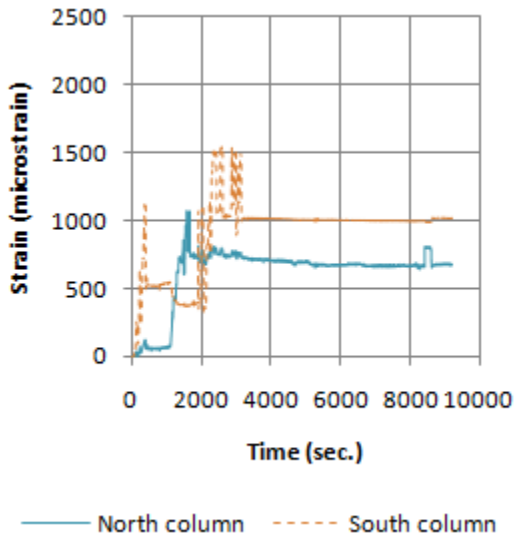

Figure 5.7.3: Post-tensioning specimen F-FRP3-R

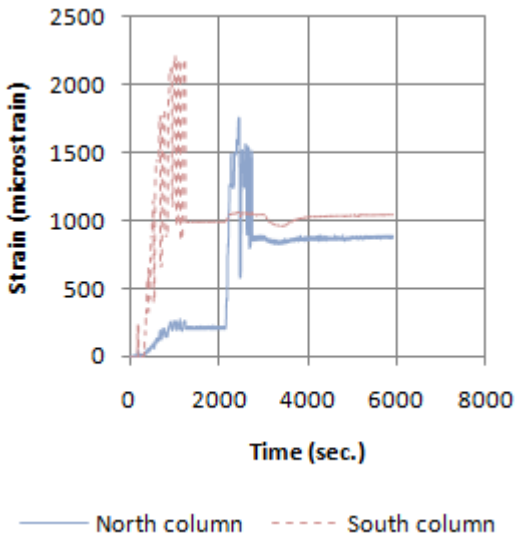

Figure 5.7.4: Post-tensioning specimen F-FRP3-S

As described in chapter 3, the procedure of post-tensioning the two columns of each of the four specimens involved several steps, starting with post-tensioning the first column to the target strain using the hydraulic ram. Immediate losses in post-tensioning stress appeared following turning off the hydraulic ram after tightening the top nut, which was performed manually.

Tightening the ram manually is highly variable and the losses that follow that step were also widely variable depending on the degree of tightening performed by the operator. One reason for such losses is that the nut will slip into the anchorage plate as soon as the hydraulic ram stops supporting it when it is turned off, leading to losses, which are inversely proportional to the degree of tightening the nut performed by the operator. For example, the initial attempt in specimen F-RC suffered immediate losses of 47%. By trial and error, the steel bar was then post-tensioned to a higher strain, the top nut tightened, and the hydraulic ram turned off to observe the final strain value. The procedure was repeated until both columns reached the target strain.

5.7.2 Bar stress while testing

The rocking mechanism was observed during testing specimens of F-FRP1, F-FRP3, F-FRP3-R, and F-FRP3-S. Gap openings formed at interfaces were described in section 5.2. These gaps led to elongation of the steel-bar, resulting in stressing the steel bars beyond the initial post-tension. Figures 5.7.3 to 5.7.5 show displacement graphed against the steel bar strain values during testing of specimens F-FRP1, F-FRP3, and F-FRP3-S. Negative displacements indicate displacement to the south direction. The strain gages attached to the north column of specimen F-FRP1 failed after displacement values of 3.57 in. and -3.43 in. and therefore only the strain readings prior to reaching the displacement levels of 3.57 in and -3.43 were included in the

figure. The strain gages attached to the steel bars of specimen F-FRP3-R failed early during testing and their results were therefore omitted.

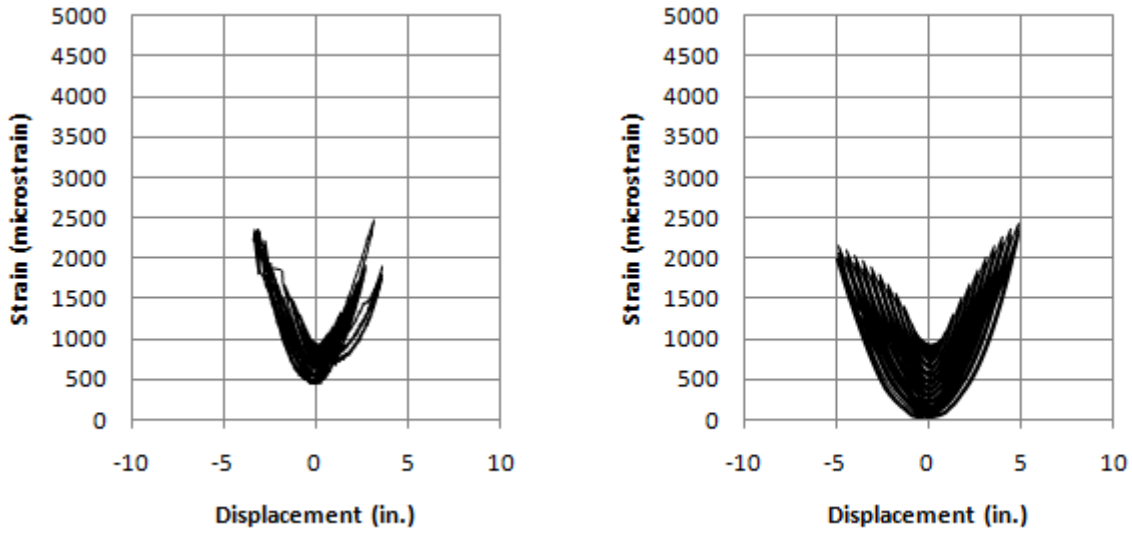

(a): North Column (b): South Column

Figure 5.7.5: Specimen F-FRP1 displacement vs. steel bar strain

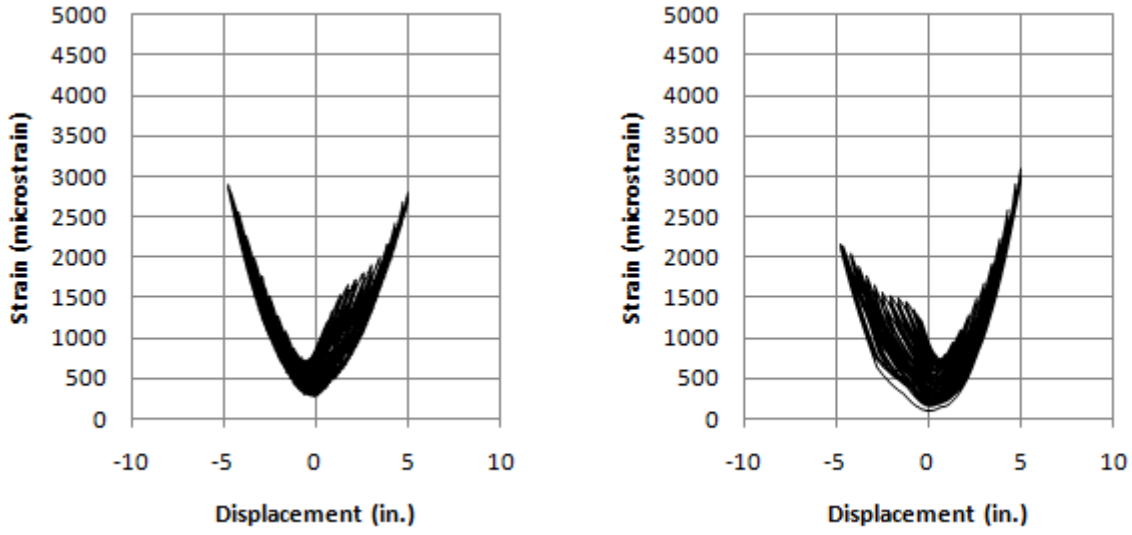

(a): North Column (b): South Column

Figure 5.7.6: Specimen F-FRP3 displacement vs. steel bar strain

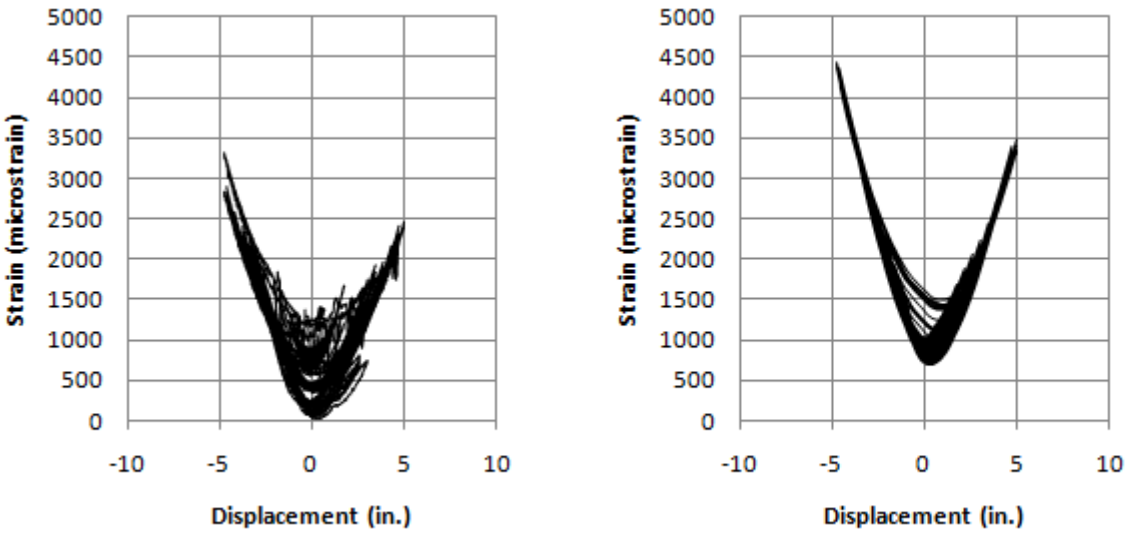

(a): North Column (b): South Column

Figure 5.7.7: Specimen F-FRP3-S displacement vs. steel bar strain

Table 5.7.1 shows a summary of the maximum and minimum bar strains and the displacements at which they occurred for the above specimens. It also shows the percentage that the maximum bar stresses reached compared to the nominal strength of the bars (150 ksi).

Specimen	North Column					South Column				
	Lateral disp. at min. strain (in)	Min. strain (micro-strain)	Lateral disp. at max. strain	Max. strain (micro-strain)	% max. bar stress of nominal bar strength	Lateral disp. at min. strain (in)	Min. strain (micro-strain)	Lateral disp. at max. strain	Max. strain (micro-strain)	% max. bar stress of nominal bar strength
F-FRP1	-0.36	455	3.12	2473	49	-0.53	11	4.90	2426	48
F-FRP3	-0.11	269	-4.80	2893	57	-0.06	91	4.95	3089	61
F-FRP-S	0.16	20	-4.80	3329	66	0.37	703	-4.80	4443	88

Table 5.7.1: Summary of post-tensioning bars strain values

As mentioned in chapter 3, the ultimate strength of the post-tensioning steel bar is 150 ksi corresponding to a force of 187.5 kips. Also, the post-tensioning steel bar complies with ASTM A722 which states that the minimum yield strength of the steel bar must exceed at least 80% of the ultimate strength. Comparing the maximum strain values, specimen F-FRP3-S had the highest strain of 3329 at the north column corresponding to a force of 124 kips which is 66% of the ultimate strength of the post-tensioning steel bar and is therefore less than the yielding strength of the bar; and 4443 micro-strain at the south column corresponding to a force of 165 kips which is 88% of the ultimate strength of the post-tensioning steel bar, i.e. exceeded the yield strength of the steel bar (120 ksi or 150 kips). Given that, none of the bars reached the yielding stress (which was one of the design provisions) except for the bar at the south column of specimen F-FRP3-S, which exceeded the yielding force by 5.9%, mostly due to the unexpected failure in the steel angle at the northern corner of the beam.

The columns of all specimens lost various amount of post-tension. One reason is loosening of the anchor nut of the post-tensioning bar during the test. Other reasons are related to permanent deformation to the columns due to creep and permanent shortening due to radial expansion as a result of high axial loads (Poisson's effect). For specimen F-FRP1, the north column lost 51.9% of its initial post-tensioning stress before the strain gages attached to the bar failed after the 3.40 in. displacement level as mentioned previously in this section; while the south column lost 98.8% of its initial post-tensioning stress. For specimen F-FRP3, the north column lost 69.3% while the south column lost 90.0% of its initial post-tension. For specimen F-FRP3-S, the north column lost 97.7% while the south column lost 32.8% of its initial post-tension.

5.8 FRP tube strains

The FRP circumferential strains in north and south faces of each column of each FRP frame was measured at heights of 2, 4, 41, and 43 in.

The gages measuring longitudinal strain of every column of specimens F-FRP1, F-FRP3, F-FRP3-R, and F-FRP3-S were set at the west face of the column and at two heights: 4 in. and 41 in. More details are shown in Chapter 3.

Figures 5.8.1 to 5.8.4 show the FRP circumferential and longitudinal strains for North and south columns of each FRP specimen plotted against displacement. All the graphs of the FRP strain gages of each specimen are available in the appendix.

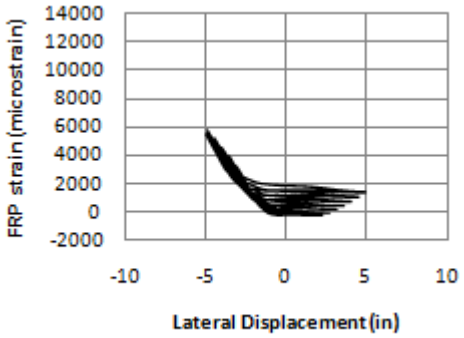

(a): Circumferential north gage at 43 in Column N

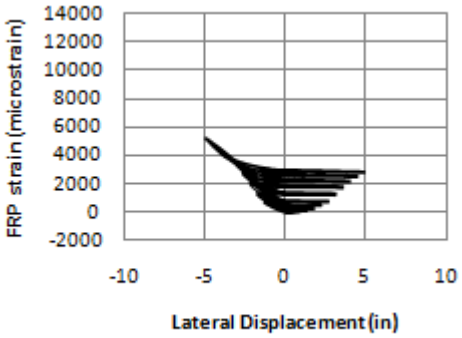

(b): Circumferential north gage at 43 in. Column S

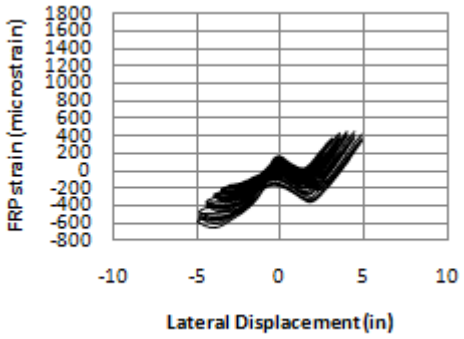

(c): Longitudinal strain at 41 in. Column N

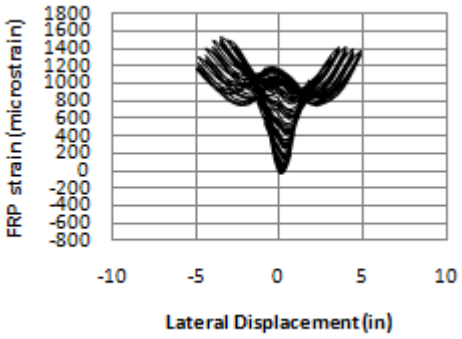

(d): Longitudinal strain gage at 41 in Column S

Figure 5.8.1: Specimen F-FRP1 FRP strain for North and South columns

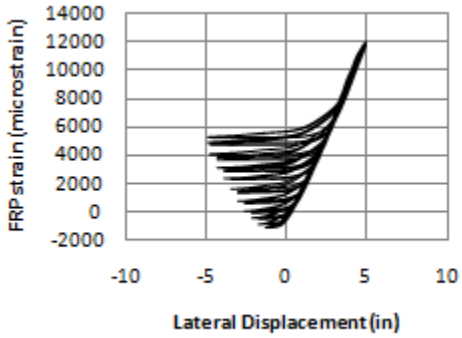

(a): Circumferential south gage at 43 in.
Column N

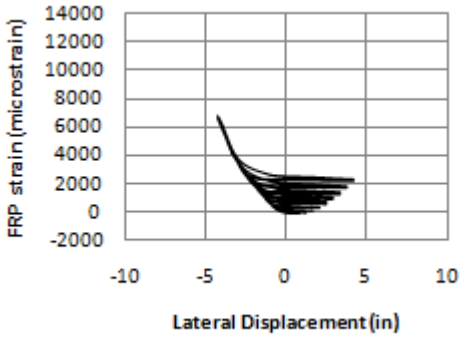

(b): Circumferential north gage at 43 in.
Column S

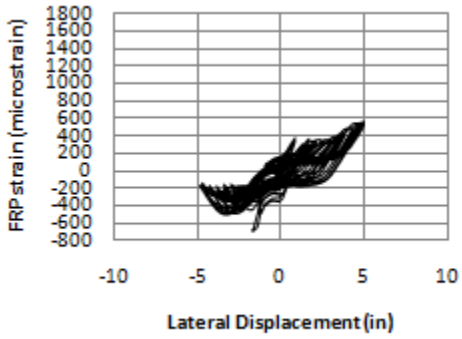

(c): Longitudinal strain gage at 41 in.
Column N

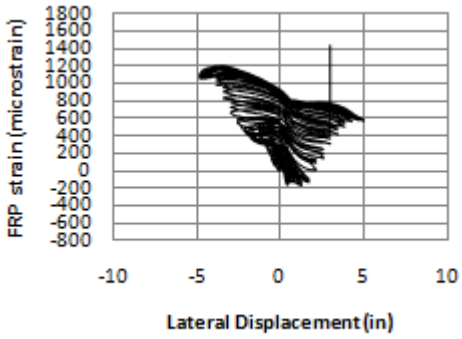

(d): Longitudinal strain at 4 in. height
Column S

Figure 5.8.2: Specimen F-FRP3 FRP strain for North and South columns

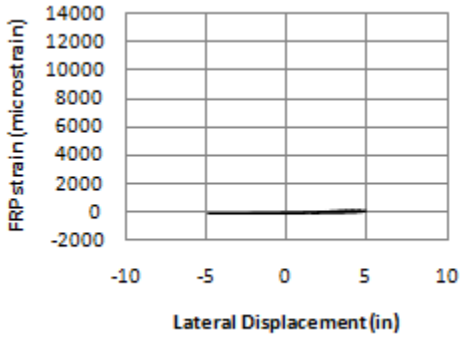

(a): Circumferential south gage at 43 in.
Column N

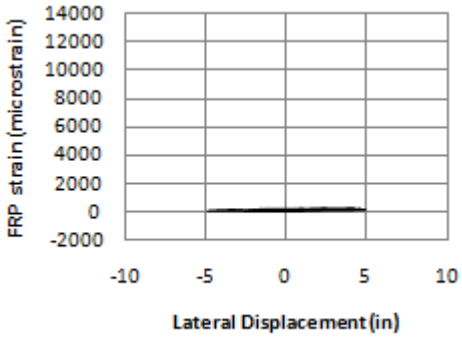

(b): Circumferential north gage at 2 in.
Column S

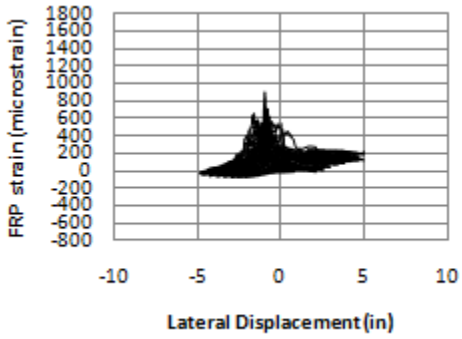

(c): Longitudinal strain gage at 4 in.
Column N

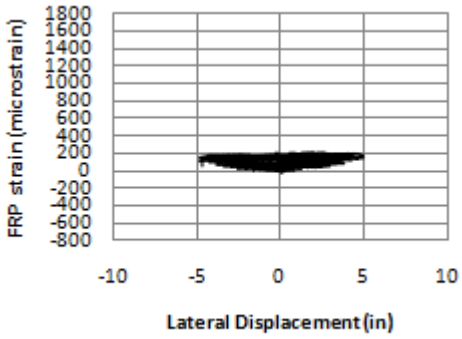

(d): Longitudinal strain gage at 4 in.
Column S

Figure 5.8.3: Specimen F-FRP3-R FRP strain for North and South columns

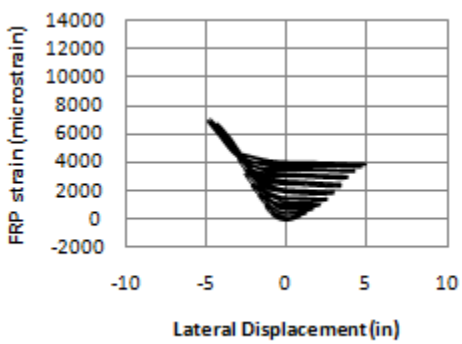

(a): Circumferential north gage at 43 in.

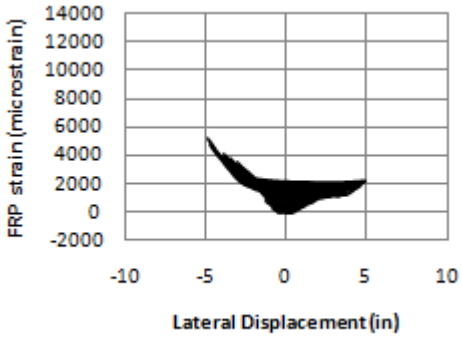

(b): Circumferential north gage at 2 in.

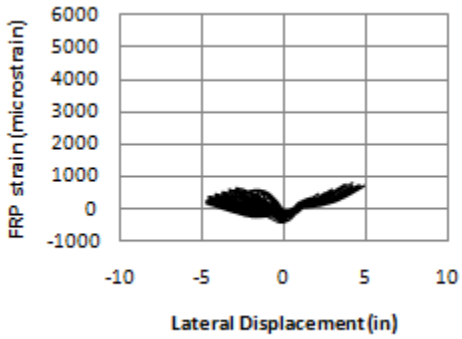

(c): Longitudinal strain gage at 4 in.

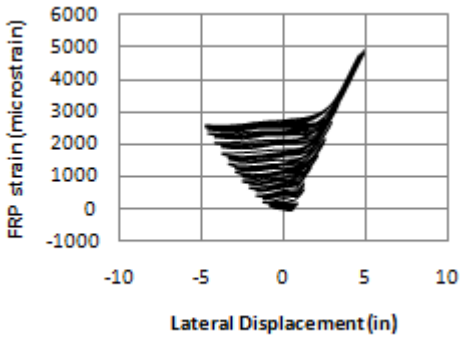

(d): Longitudinal strain gage at 4 in.

Figure 5.8.4: Specimen F-FRP3-S FRP strain

For circumferential FRP strain, it can be seen from the figures that the values reach higher magnitudes in one direction of displacement but not the other. This is explained by the rocking mechanism. Each of the circumferential strain gages was attached at either the north face or the south of the column. When the frame is laterally displaced, the columns undergo rocking. This leads to a gap opening at one side of the column while the other undergoes increasing compression due to the rotation of the interface which is blocked by the support interface (i.e. the beam if at the top interface or the footing at the bottom interface). The strain readings reach maximum values depending on whether the circumferential strain gage is at the north or south face of the column and on the direction of lateral loading.

The circumferential FRP strain depends mainly on the axial stress applied in the column, hence, the post-tensioning force influences the strain readings. Initial post-tension as well as losses in post-tension therefore affect FRP strain readings.

All the above explanations assume flat interfaces of the columns that are perpendicular to column longitudinal axis. The column segments interfaces were not perfectly flat or perpendicular to the column segment longitudinal axis due to errors in the cut of the FRP tube and to errors that occurred while casting which include minor tilting of the column segments and sagging of the wooden supports holding the column segments. Wheel grinding of the interfaces was conducted to create flat and smooth surfaces, but that did not assure interfaces that are perpendicular to the column's longitudinal axis. As a result of such imperfections, the stresses were not evenly distributed on the column interface which is another reason of differences in circumferential FRP strain values.

Specimen F-FRP3-R had the lowest circumferential strain due to the presence of the rubber layers. These layers acted as buffer layers preventing high compression in the columns as they were expanding radially.

5.9 Section rotations

For each of the five specimens, sixteen string potentiometers were installed for measuring rotations, as described in Chapter 3. Rotations were measured for each column of the five specimens at four sections. Readings from each string potentiometer was multiplied by correction factors which were found by calibration.

For specimen F-RC, the test was completed over two separate time periods. No rotations readings were taken at the top joints of the North or South columns. Also, the rods attached to the columns (with adhesives) were detached when the concrete cover was compromised during testing and therefore the rotation readings were stopped when that occurred. Figure 5.9.1 shows graphs of time against rotations measured at different heights of the North and South columns of specimen F-RC.

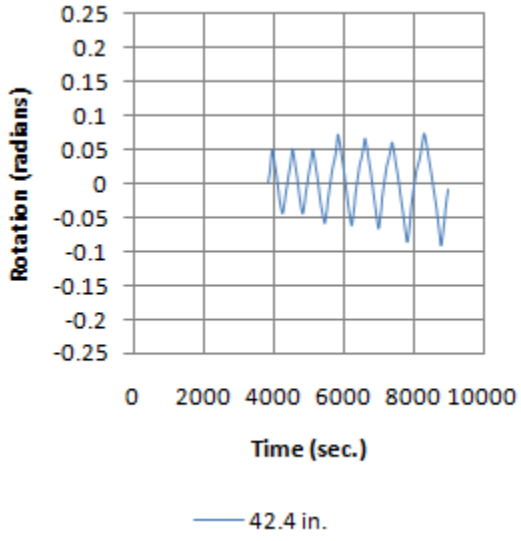

(a): North Column top joint

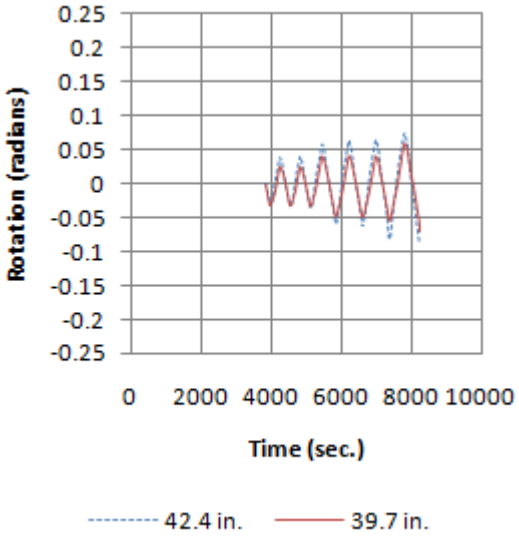

(b): South Column top joint

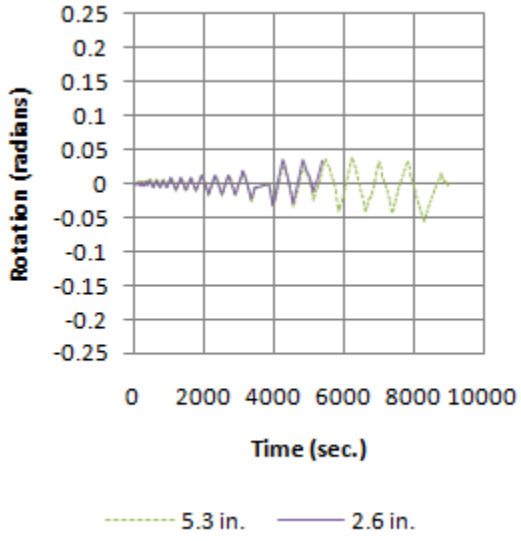

(c): North Column bottom joint

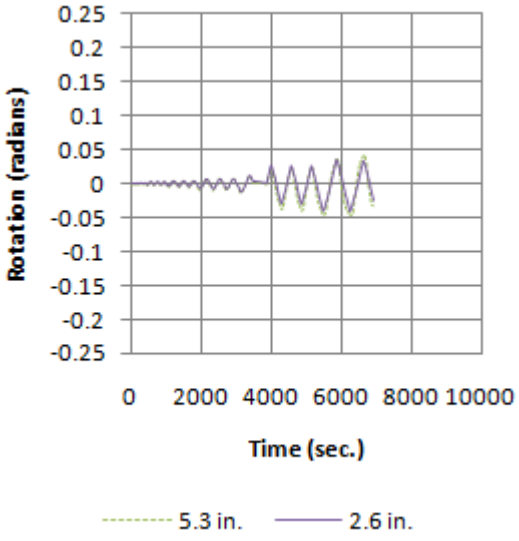

(d): South Column bottom joint

Figure 5.9.1: Time vs. rotation of specimen F-RC at different column heights

The applied lateral load applied to the specimen increased as time increased, which explains why rotations increased with time. Also, each displacement level was repeated for three cycles, which explains why rotations were close every three cycles. However, since the resistance of the specimen to the applied lateral load decreases slightly when the cycle is repeated for the same

displacement level (due to damage of the specimen after each loading cycle), the magnitudes of the rotations at the same displacement level are not exactly equal in magnitude.
Rotations at the top joints of both columns are higher than those at the bottom joints. This can be explained by the fact the footing is relatively much stiffer to rotations than the beam, and since the columns joints are fixed, larger magnitude of rotation occurred at the top joints.

Figure 5.9.2 shows graphs of time against rotations measured at different heights of the North and South columns of specimen F-FRP1.

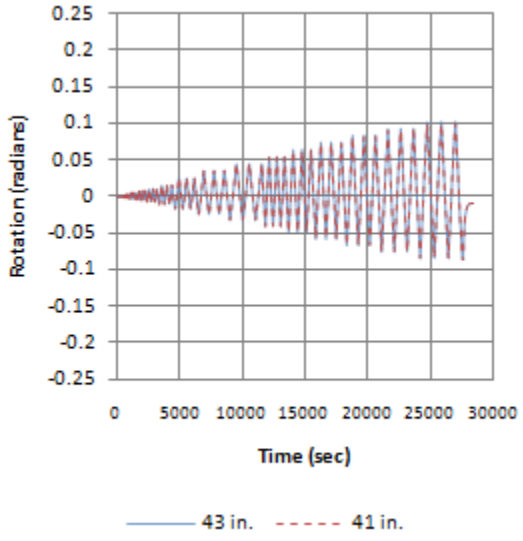

(a): North Column top joint

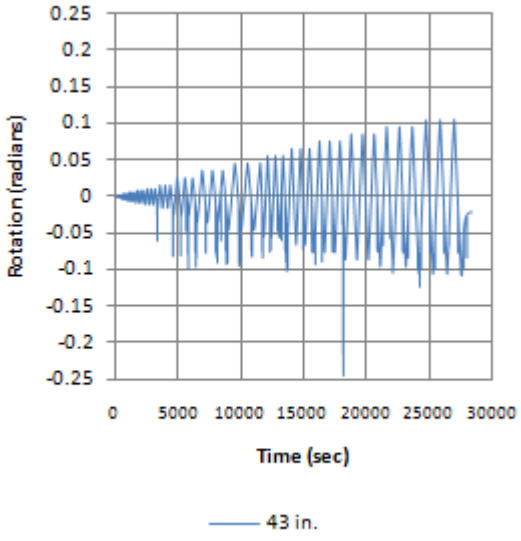

(b): South Column top joint

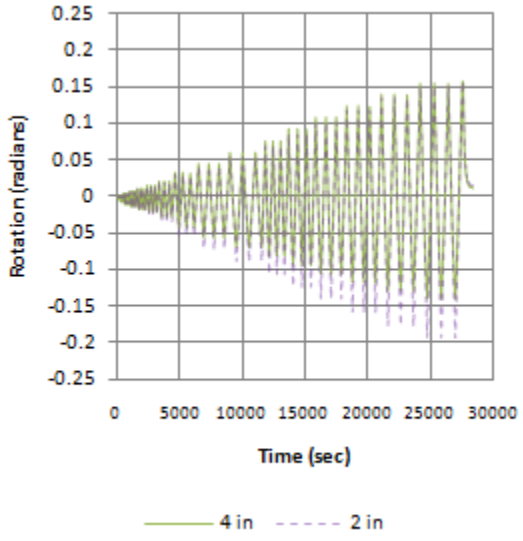

(c): North Column bottom joint

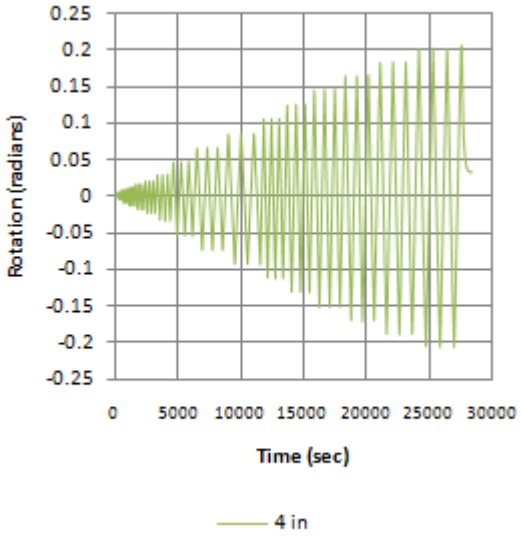

(d): South Column bottom joint

Figure 5.9.2: Time vs. rotation of specimen F-FRP1 at different column heights

Compared to specimen F-RC, rotation values of specimen F-FRP1 are higher in magnitude. This can be explained by the occurrence of rocking mechanism in specimen F-FRP1, which lead to the joints of the columns acting as pins rather than being fixed as in specimen F-RC. The joints

with specimen F-FRP1 have lower rotational stiffness than those of specimen F-RC, and therefore rotated to higher magnitudes.

Comparing the rotations of the top joints of specimen F-FRP1 to the bottom joints, the top joints have lower rotation magnitudes. This can be explained by the fact that the beam is more flexible to rotation than the footing, which led to the upper joints undergoing less rocking with smaller gaps opening, leading to the top joints acting less as pins than the lower joints.

Figure 5.9.3 shows graphs of time against rotations measured at different heights of the North and South columns of specimen F-FRP3.

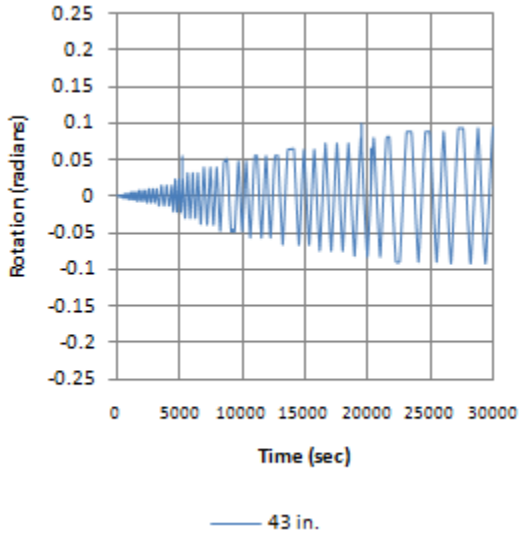

(a): North Column top joint

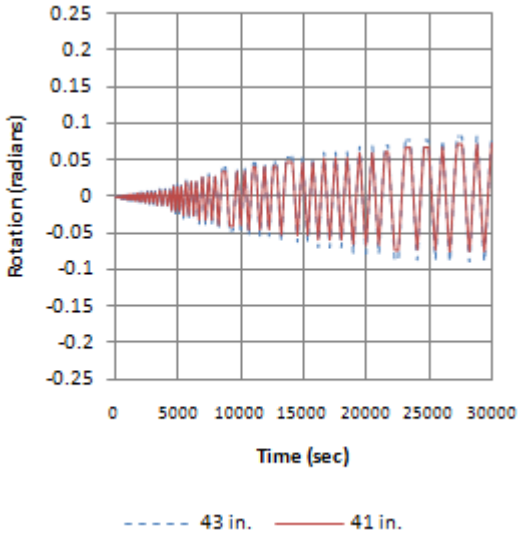

(b): South Column top joint

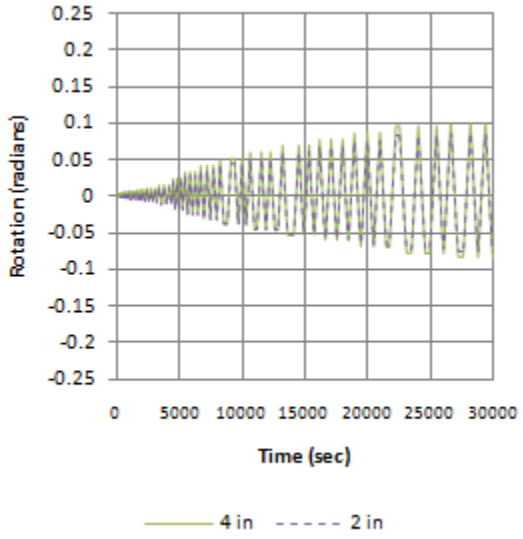

(c): North Column bottom joint

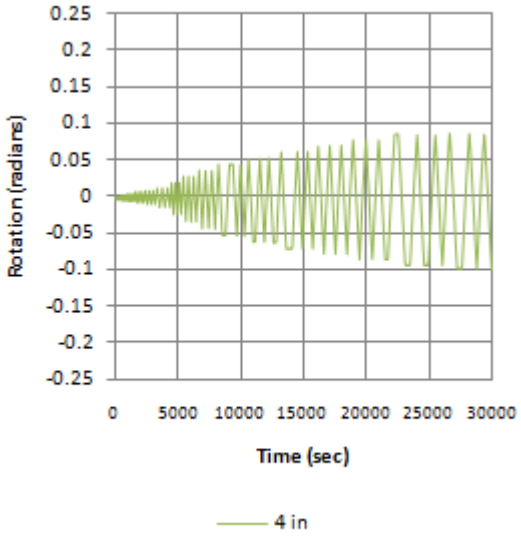

(d): South Column bottom joint

Figure 5.9.3: Time vs. rotation of specimen F-FRP3 at different column heights

Compared to specimen F-FRP1, the rotation values of specimen F-FRP3 are lower. This can be explained by the fact that the columns of specimen F-FRP3 are segmented. This leads to less rotation of the upper and lower segments since rocking and gap opening may occur at the middle segment. Although such gaps were not visible due to their small magnitudes as well as the fact

that the surfaces of the column segments were not perfectly flat and perpendicular to the longitudinal axes of column segments stacked on top of each other.

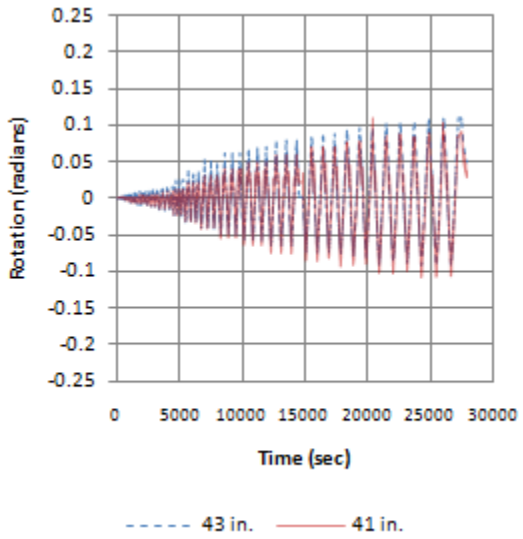

(a): North Column top joint

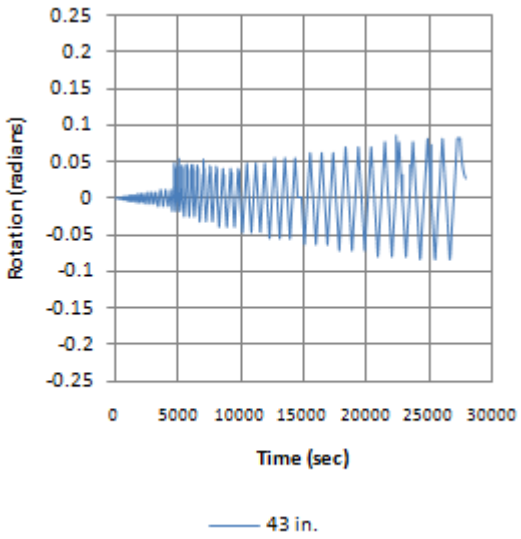

(b): South Column top joint

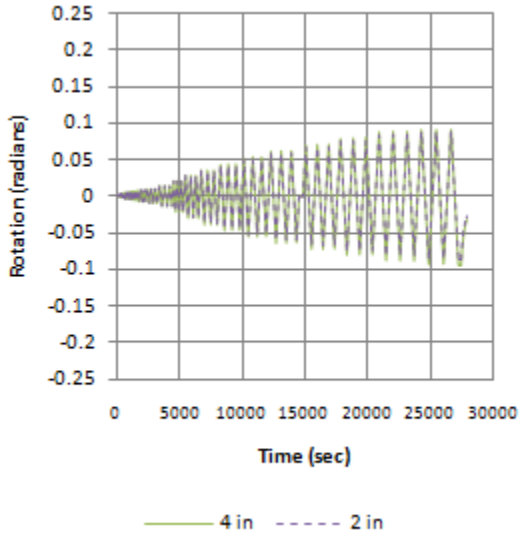

(c): North Column bottom joint

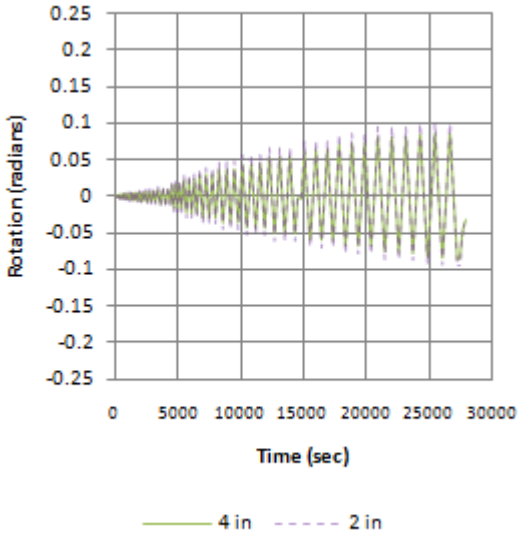

(d): South Column bottom joint

Figure 5.9.4: Time vs. rotation of specimen F-FRP3-R at different column heights

Rotations values for specimen F-FRP3-R were close in magnitude to those of specimen F-FRP3, which means that the rubber layer does not appear to affect rotation values at the same lateral displacements.

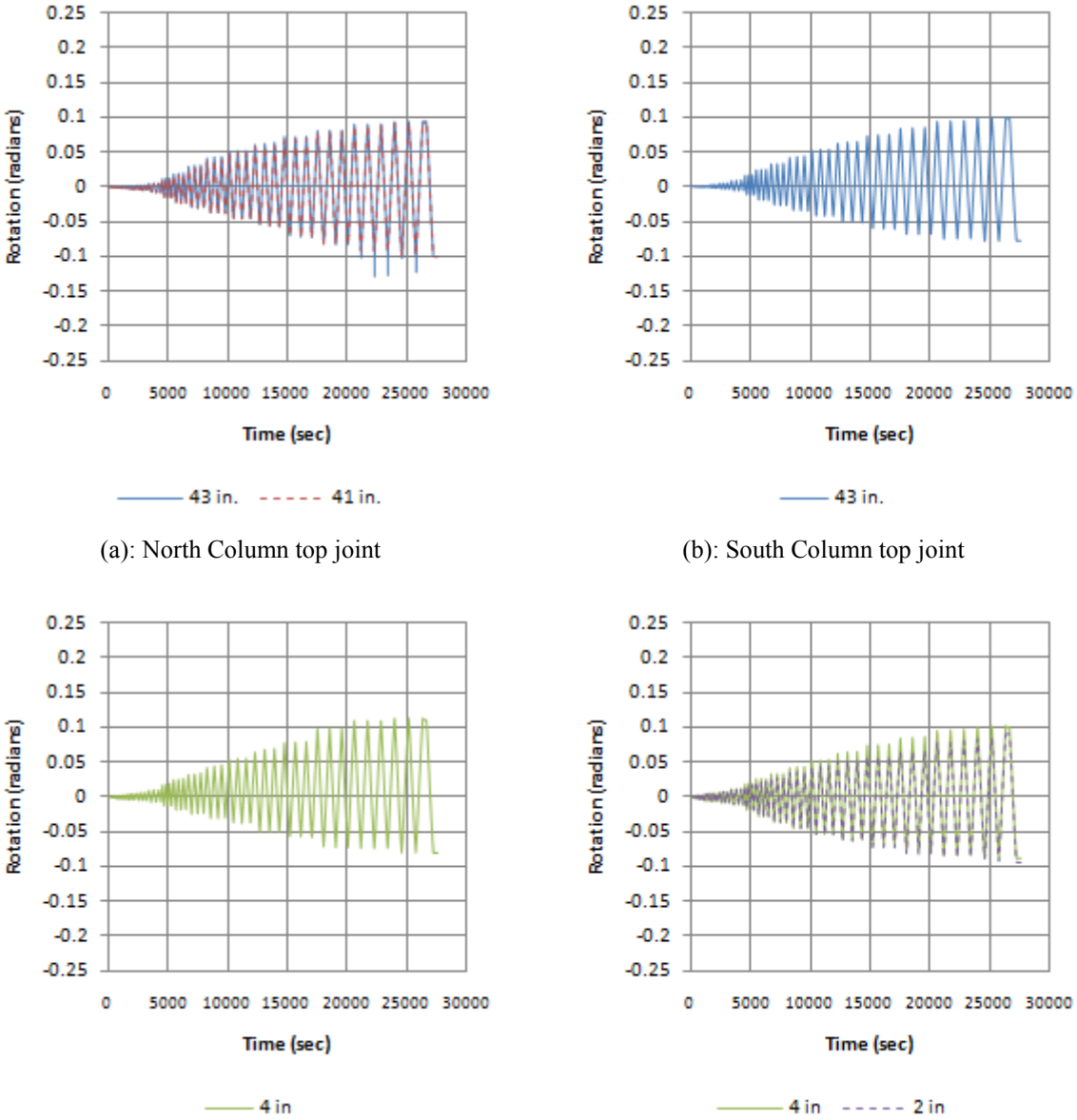

(a): North Column top joint

(b): South Column top joint

(c): North Column bottom joint

(d): South Column bottom joint

Figure 5.9.5: Time vs. rotation of specimen F-FRP3-S at different column heights

Rotation values of specimen F-FRP3-S were close in magnitude to the other segmented FRP frames. With specimen F-FRP3-S, the top and bottom segments were more restricted to rocking due to the attached sacrificial steel angles at the corners. The values of rotations of the other segmented specimens were close in magnitude to those of specimen F-FRP3-S, which means that the top and bottom segments of those other segmented specimens (i.e. specimen F-FRP3 and F-FRP3-R) also did not rotate as each of the single segmented columns of specimen F-FRP1 did.

A general observation related to all the FRP specimens is that the columns rotated more in a rigid way with joints resembling pins rather than undergoing double curvature as the monolithic columns of specimen F-RC did. This can be seen by the almost equal rotation angles measured at different points of the top joint of a column or the rotation angles measured at different points at the bottom joint of a column.

5.10 Curvature

Curvature was computed for each section at which rotations were calculated in the previous section as discussed in Chapter 3. Curvature was calculated at the first peak displacement value of each displacement level. Figure 5.10.1 shows graphs of displacement against curvature at different sections of the north and south columns of specimen F-RC.

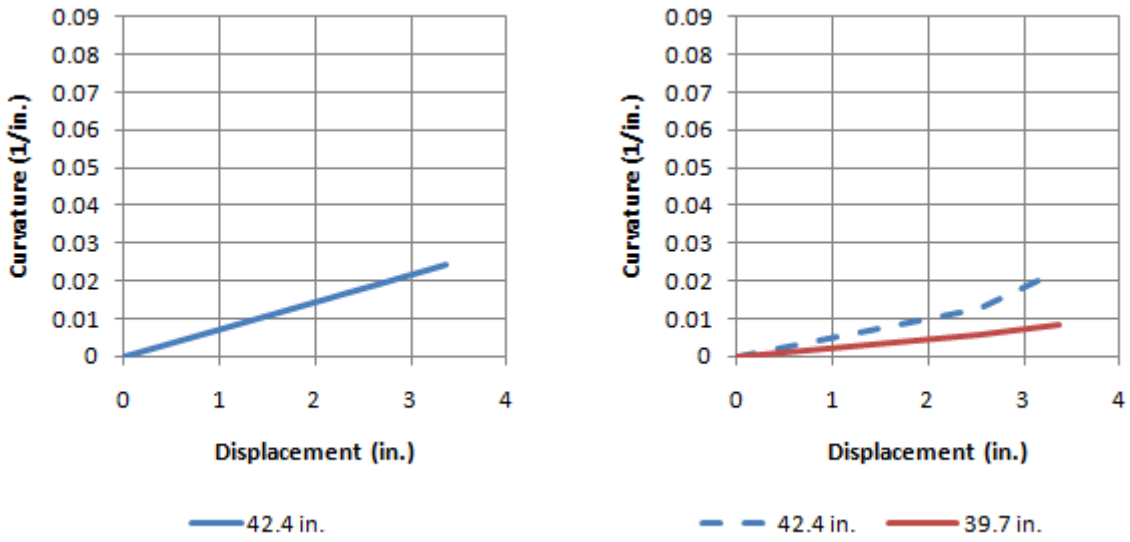

(a): North Column top joint

(b): South Column top joint

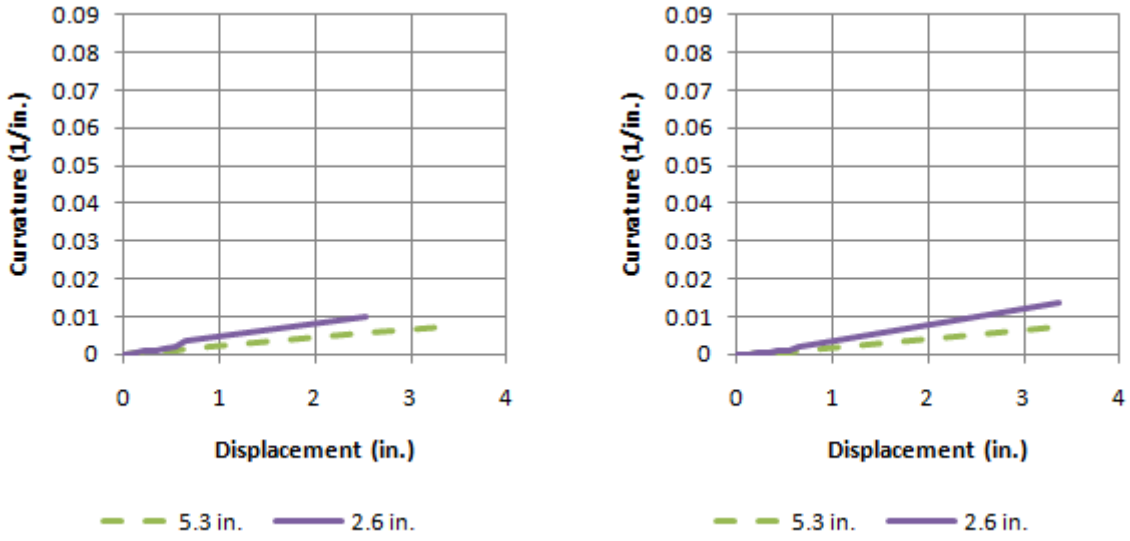

(c): North Column bottom joint

(d): South Column bottom joint

Figure 5.10.1: Displacement vs. curvature of specimen F-RC

Figure 5.10.2 shows graphs of displacement against curvature at different sections of the north and south columns of specimen F-FRP1

.

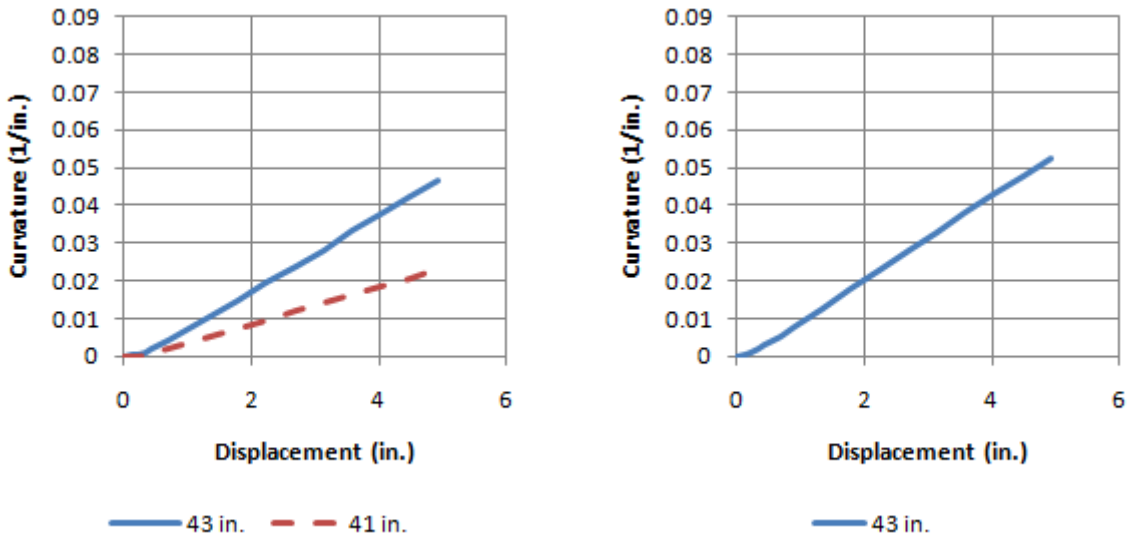

(a): North Column top joint

(b): South Column top joint

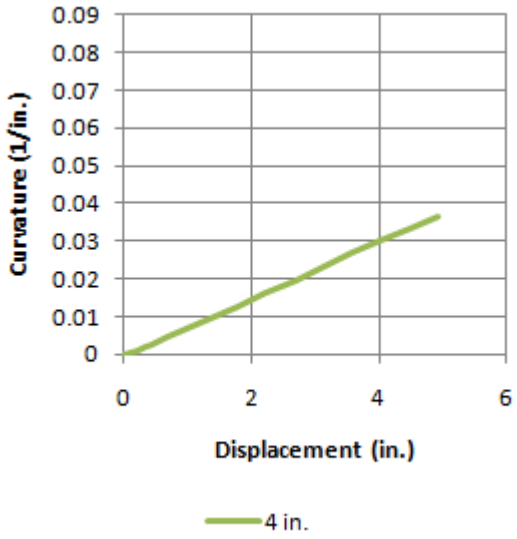

(c): North Column bottom joint

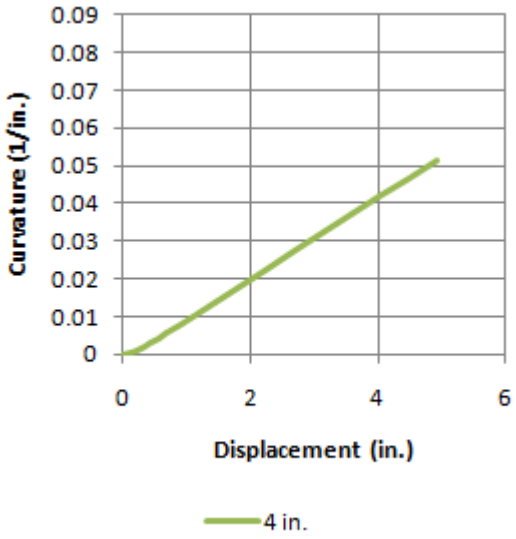

(d): South Column bottom joint

Figure 5.10.2: Displacement vs. curvature of specimen F-FRP1

Figure 5.10.3 shows graphs of displacement against curvature at different sections of the north and south columns of specimen F-FRP3.

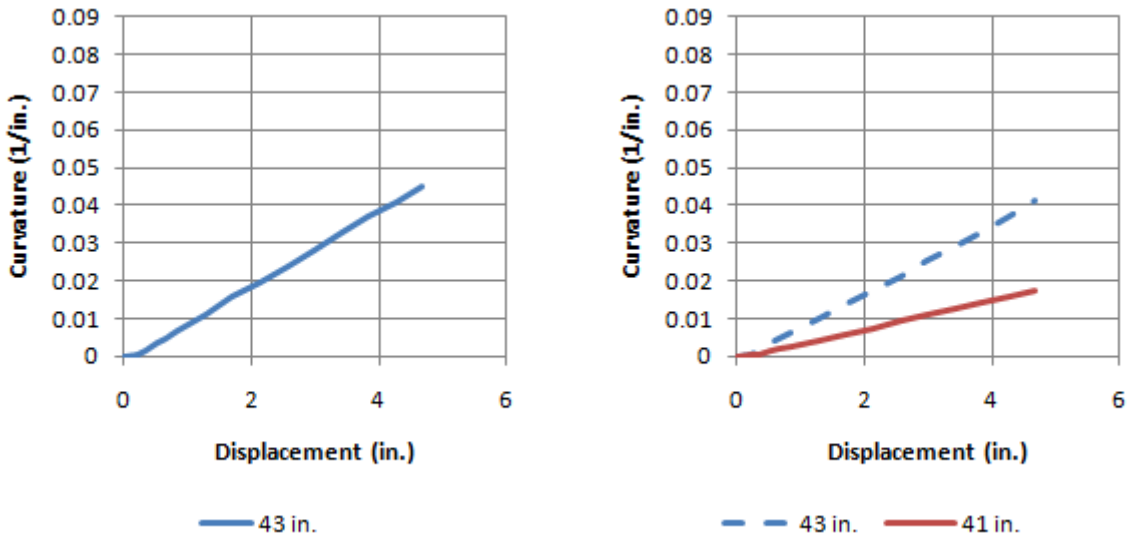

(a): North Column top joint

(b): South Column top joint

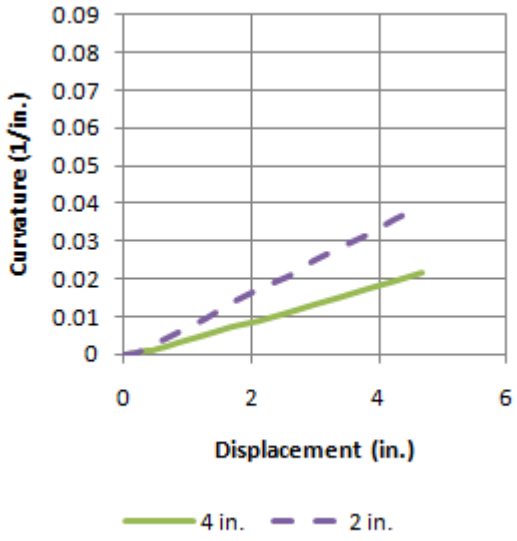

(c): North Column bottom joint

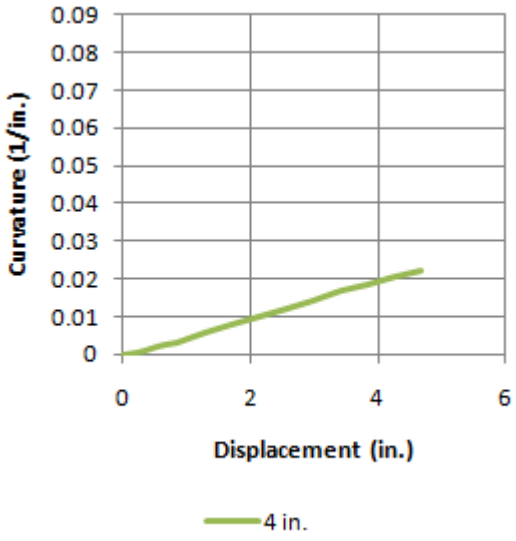

(d): South Column bottom joint

Figure 5.10.3: Displacement vs. curvature of specimen F-FRP3

Figure 5.10.4 shows graphs of displacement against curvature at different sections of the north and south columns of specimen F-FRP3-R.

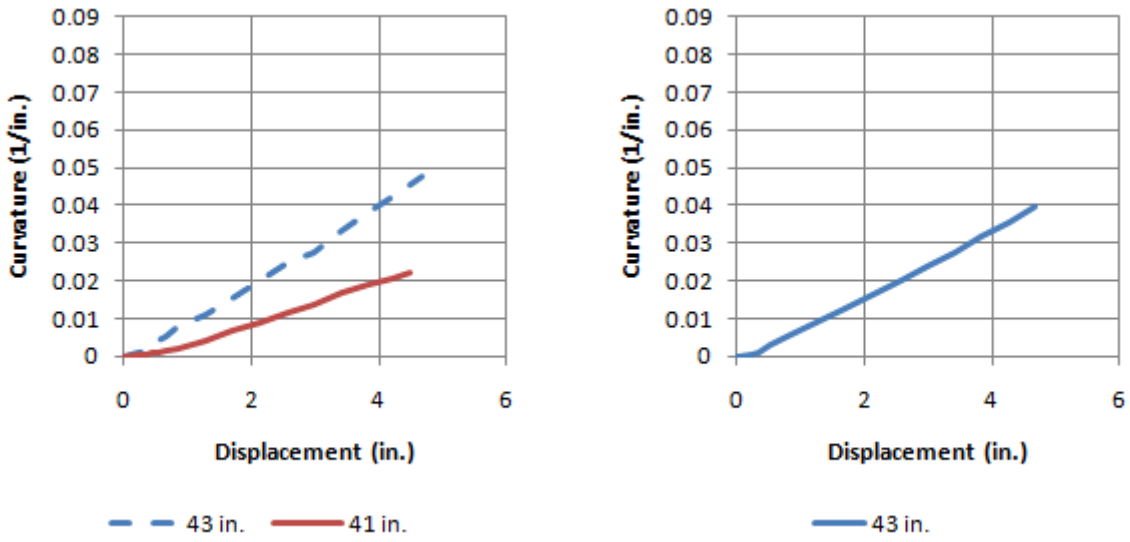

(a): North Column top joint

(b): South Column top joint

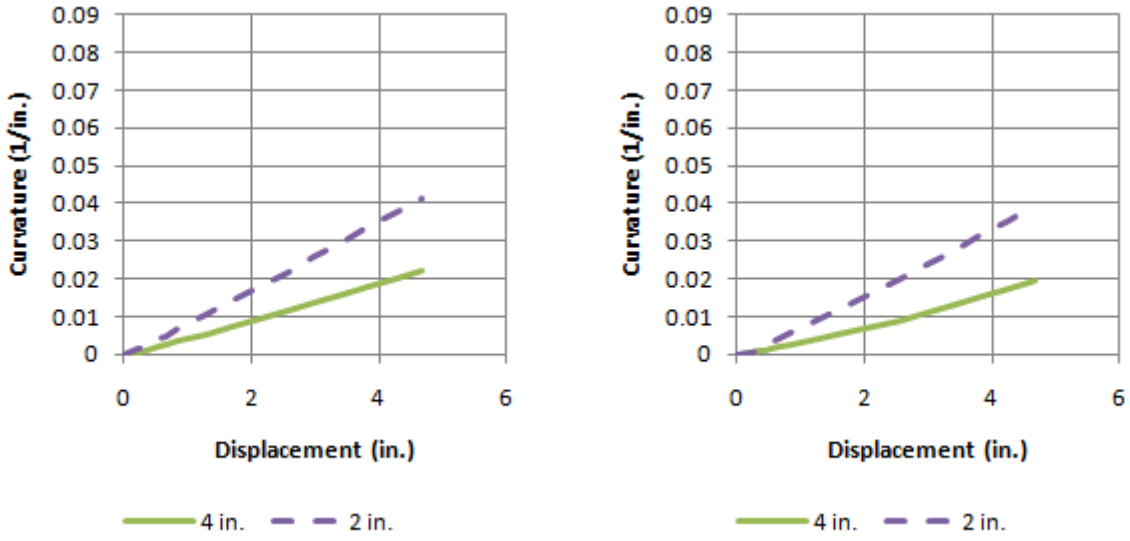

(c): North Column bottom joint

(d): South Column bottom joint

Figure 5.10.4: Displacement vs. curvature of specimen F-FRP3-R

Figure 5.10.5 show graphs of displacement against curvature at different sections of the north and south columns of specimen F-FRP3-S.

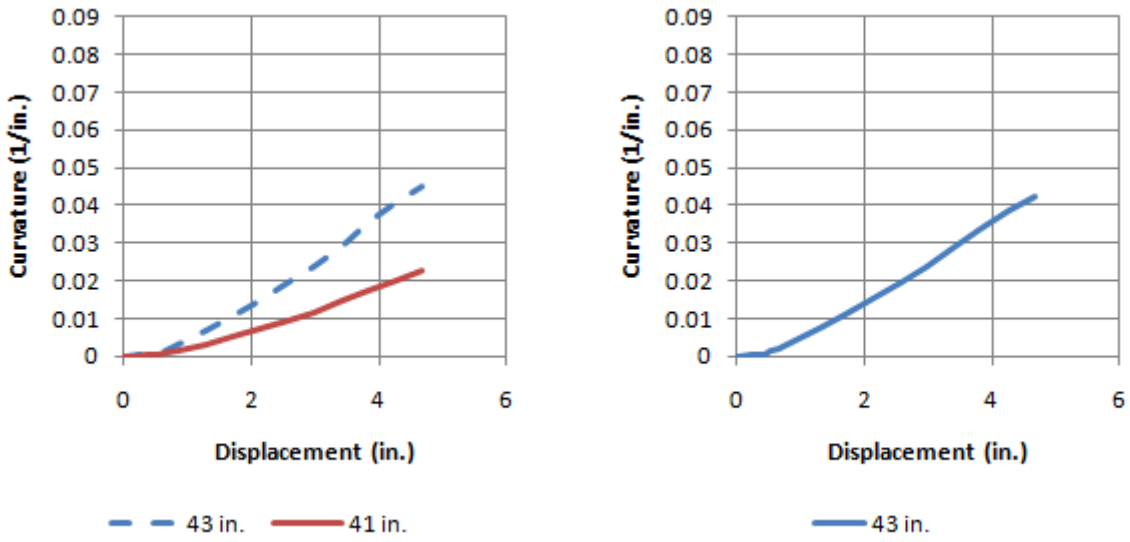

(a): North Column top joint

(b): South Column top joint

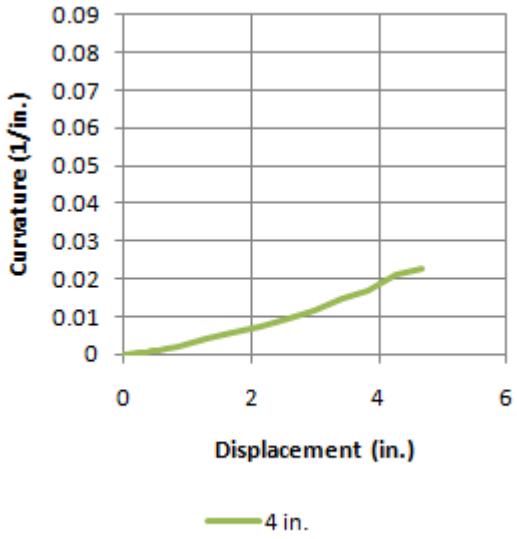

(c): North Column bottom joint

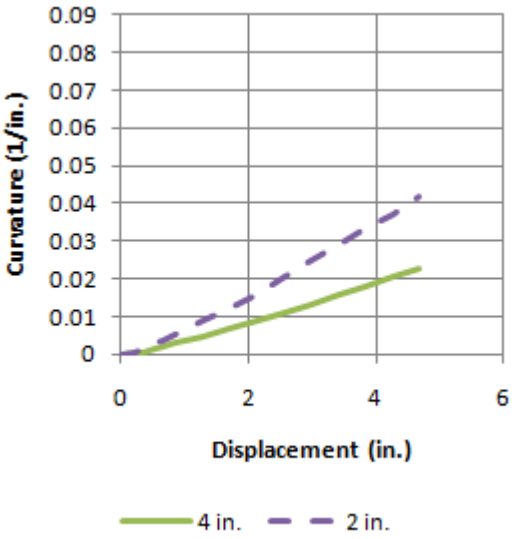

(d): South Column bottom joint

Figure 5.10.5: Displacement vs. curvature of specimen F-FRP3-S

The curvature data depended on the rotation data. In concept, if two sections rotate with similar angles then no curvature has occurred between them. However, in this case, the curvature at each

section was calculated without reference to the rotation of the previous section. Therefore, the height of the section by which the value of rotation was divided becomes the key factor. The rotation of the FRP columns was discussed in the previous section and can be described as rigid rotation. Therefore, it can be seen here that the curvature values calculated for the sections at height of 43 in. are lower in magnitude than those at height of 41 in. The same applies for the lower joints. The reason is that curvature is inversely proportional to the height of the section.

Chapter 6

Pushover Analysis

6.1 Introduction

Pushover models were constructed to anticipate the performance of specimens. In this chapter, the backbone curves measured during testing of specimens F-RC and F-FRP1 are compared to the force-displacement response predicted using pushover models.

6.2 Pushover of specimen F-RC

SAP2000 was used to construct a pushover model to simulate the performance of the monolithic reinforced concrete frame (specimen F-RC). The model required several key variables to define its properties. These include material properties, geometric properties, boundary conditions, and moment-curvature relationships.

Initially, moment curvature relationships were computed using the software package XTRACT. Concrete strength and reinforcement details mentioned in Chapter 3 were input in XTRACT. Moments and curvature at initial yield as well as at ultimate capacity, then the effective yield moment and curvature values were determined using the idealized bilinear moment-curvature envelope obtained from XTRACT. Figure 6.2.1 shows the idealized bilinear moment-curvature envelope obtained from XTRACT for the as-built monolithic RC frame.

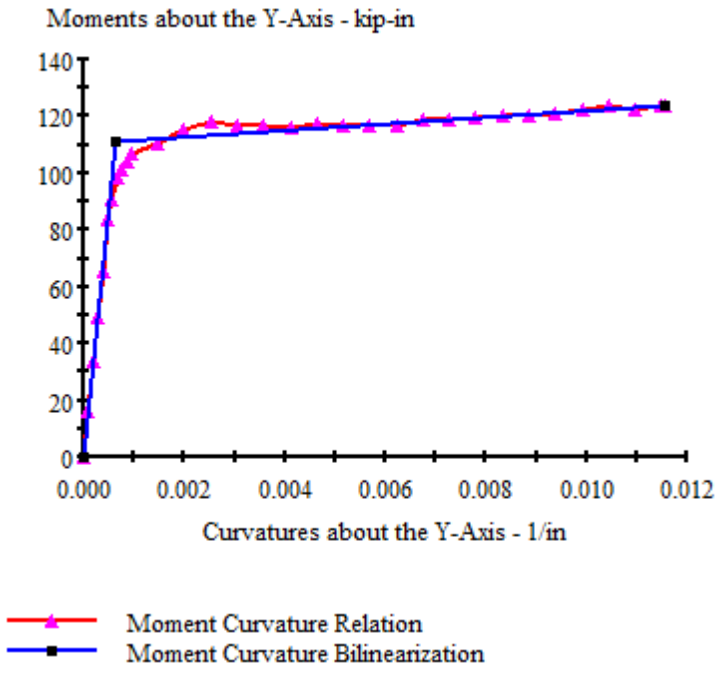

Figure 6.2.1: Moment-curvature relationship of the RC column-section from XTRACT

SAP2000 is then used to conduct pushover analysis of the monolithic frame. Columns and beam cross sections were modeled with the same values as those in Chapter 3. The height of the columns was input as the height from the surface of the footing to the beam center, which is 52.5 in. Effective EI (obtained from XTRACT) was input into SAP2000.

SAP2000 uses the material properties mentioned above during the elastic stage of pushover analysis. To model the frame in the nonlinear inelastic stage, plastic hinges were defined and assigned to the frame. The type of plastic hinge selected was M2 which is a plastic hinge rotating about axis 2 and is non-interacting to axial load. Using an interactive plastic hinge would be more accurate, but due to relatively low changes in axial stresses, using this type of hinge is adequate. The plastic hinge was defined using ductility factors obtained from XTRACT. The

analysis report from XTRACT is available in the Appendix. The plastic hinge length was calculated as discussed in Chapter 4 (Equation 4.1.12). Plastic hinges were assigned at the top and bottom of each column since the columns underwent double bending. Each plastic hinge location was assigned with its center a distance $\frac{L_p}{2}$ above the surface of the base for lower joints and below the bottom surface of the beam for upper joints. The reason for this assumption is that the base and the beam were much stiffer to rotation than the columns due to their geometric properties, and therefore the plastic hinges form in the column's clear height.

Figure 6.2.2 shows the load-drift response of the monolithic RC frame model in SAP2000 (specimen F-RC) compared with actual backbone curves obtained from experiments.

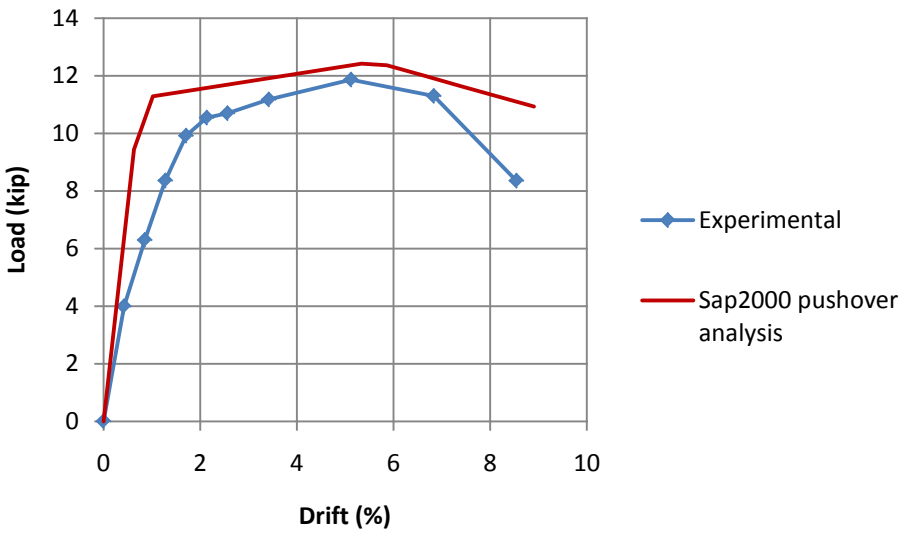

Figure 6.2.2: Specimen F-RC SAP2000 pushover model comparison

6.3 Pushover of specimen F-FRP1

SAP2000 was used to construct a pushover model to simulate the performance of the FRP frame (specimen F-FRP1). The model required several key variables to define its properties. These include material properties, geometric properties, boundary conditions, and moment-curvature relationships.

Initially, a stress-strain model is required to obtain a moment-curvature relationship. The model developed by Samaan et al. (1998) was selected, and the material properties (concrete compressive strength , concrete modulus of elasticity, FRP tensile strength, and FRP modulus of elasticity) presented in Chapter 3 were used to define the stress-strain function. Figure 6.3.1 shows the stress strain model of the FRP column-section.

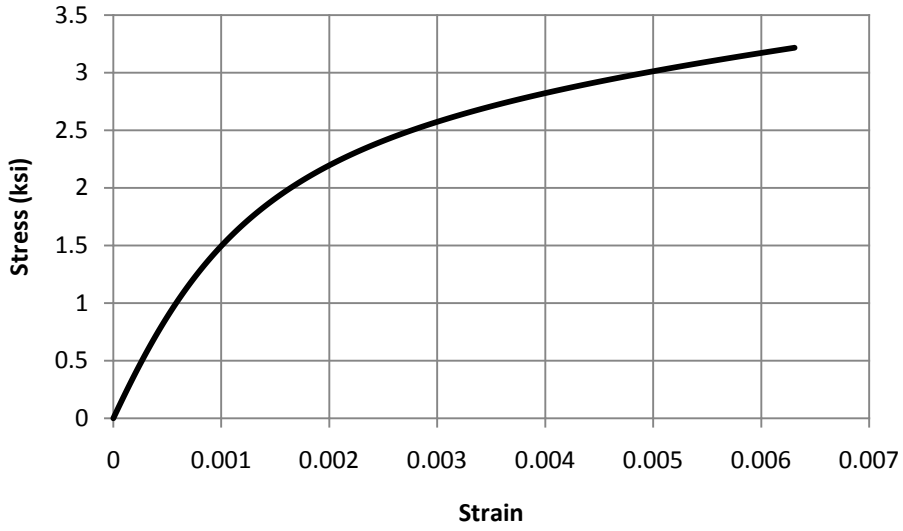

Figure 6.3.1: Stress-strain model of FRP column-section

The stress-strain function is then used to develop the moment-curvature relationship as described in Chapter 4 after Hewes and Priestley (2002). Figure 6.3.2 shows the resulting moment-curvature envelopes for FRP column.

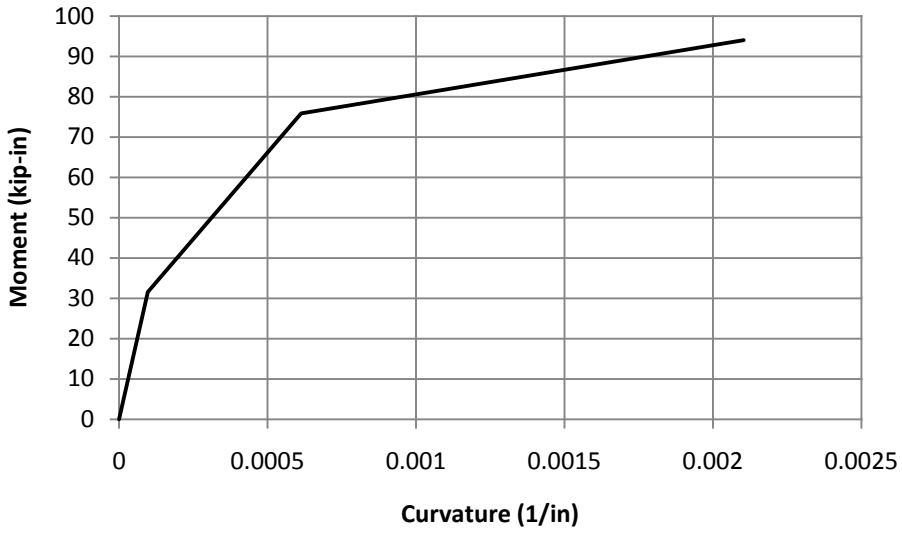

Figure 6.3.2: Moment-curvature relationship of FRP column-section

Pushover analysis is then conducted using the same procedure stated in the previous section. The same type of plastic hinge was selected (M2). The plastic hinge length was calculated as discussed in Chapter 4 and assigned. Figure 6.3.3 shows the results of the pushover analysis of the FRP frame compared with the experimental results.

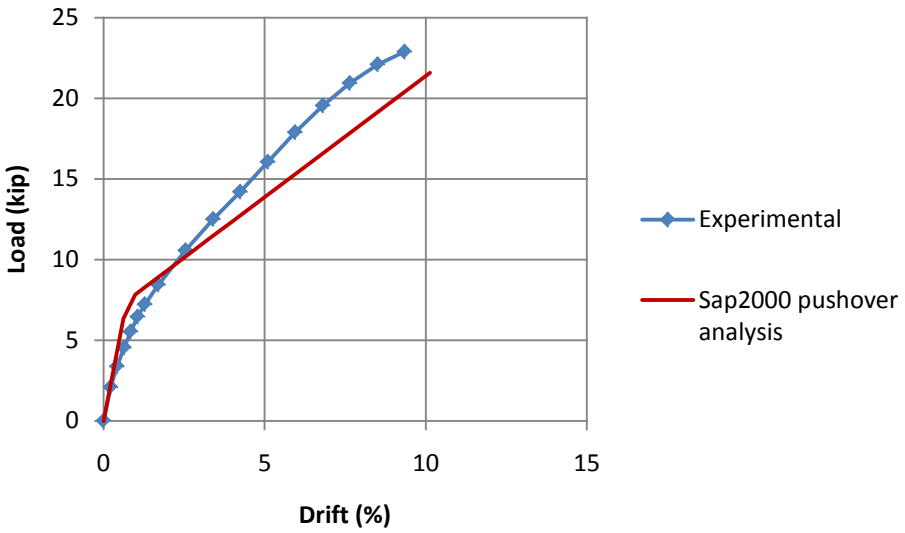

Figure 6.3.3: Specimen F-FRP1 SAP2000 pushover model comparison

6.4 Interpretation of analyses

The pushover models results using SAP2000 predicted a close approximation to the actual experimental response. It should be noted that the concrete compressive strength, concrete modulus of elasticity, FRP tensile strength, and FRP modulus of elasticity values were vital in predicting the results. They affect both the elastic portion and the inelastic portion of the response. One observation is that the equation for calculating E_c in section 8.5.1 of ACI318-05 overestimates the modulus of elasticity of concrete. The actual values were 75% of the values calculated using the ACI318-05 equation. Also, SAP2000 does not take into account the cracked section moment of inertia, and therefore effective values must be input into the material properties to account for that.

The SAP2000 pushover model of specimen F-RC overestimated the ultimate force by 4.6%, which is relatively a good approximation. The drift at which the ultimate load occurred for specimen F-RC was 5.1% in the actual tests compared to 5.3% from the pushover model, which

was also over estimated by 4.2% of the actual drift. One reason for that is that the pushover model does not into account the cyclic nature of the tests. Successive cycles weaken the frames stiffness due to damage such as micro-crack in concrete, cover spalling, and possibly rebar yielding.

The SAP2000 pushover model depended primarily on the stress-strain model that was selected. This model affects almost all the parameters of response of the model including: effective section modulus, moment and curvature at yield, moment and curvature at the ultimate loading stage. The pushover model slightly underestimated the ultimate load by 5.7% although that anticipated load was calculated at a drift 8.4% higher than the experimental ultimate drift. It should be noted that the experimental test did not lead to failure of specimen F-FRP1 which suggests that the actual behavior might differ at higher drifts, and therefore failure should be investigated to have a better understanding of the behavior the FRP frames, and to compare the results with the actual model. It should be noted that in this pushover model, the pushover load case was defined to be displacement controlled and the ultimate lateral displacement was set to be the same as the ultimate lateral drift with which the experimental tests were limited.

Chapter 7

Summary and Conclusions

7.1 Summary

Bridge construction using conventional reinforced concrete poses several disadvantages including the long period of time for construction, high susceptibility to damage during seismic events, the difficulty of repair after seismic events, and the harmful effects on local surroundings in close proximity to bridge construction projects. This research was conducted with objectives aimed to resolve the above issues along with other improvements.

In this research, the precast system was used to offer solutions to some of the above problems. Construction using the precast system is much faster than conventional reinforced concrete construction. The effect on local surroundings is much lower when the precast system is utilized since mostly the members are only to be assembled on site and no building formwork or concrete pouring occurs at the construction site. Using the precast system also offers additional advantages in terms of higher efficiency and quality control of the production of structural members due to production at specialized plants.

The concept of confinement of concrete was then applied to improve strength (compressive and shear) capabilities of bridge columns. Tubes fabricated from fiber reinforced polymers were used because they proved to offer better confinement than steel jackets due to their higher strength

properties, with the advantages of lower density (which is important for decreasing seismic force attraction to the structure) as well as not being susceptible to corrosion as steel is.

Post-tensioning was utilized in this research to provide a solution to the high residual displacements of bridges after seismic events. Unbonded post-tensioning resolved the problem of local yielding of post-tensioning steel bars and maintained them in their elastic phase of response.

Energy dissipation mechanisms were also added to the proposed systems to improve energy dissipation while maintaining damage in easily replaceable parts of the structure to facilitate the ease of repair. Different energy dissipation mechanisms were applied and evaluated.

7.2 Conclusions

Several key points can be concluded from the results of this study, these include:

- Lateral load resistance
- Damage and residual drift
- Energy dissipation

7.2.1 Lateral Load resistance

Although the conventional monolithic reinforced concrete specimen (specimen F-RC) shared the same geometric properties as that of other four proposed specimens (where the same dimensions of the footings, columns, and beam of each specimen were used for all the other specimens), the specified unconfined concrete strength was constant for all the columns, and the columns were

all designed with the same theoretical yielding moment, the monolithic frame (specimen F-RC) showed significantly lower lateral load resistance than all the other specimens. The maximum lateral load resisted by specimen F-RC was about 50% of the maximum lateral load of specimens F-FRP1, F-FRP3, and F-FRP-S. Specimen F-FRP3-R, however, showed poor response; where the lateral load resistance was significantly lower than that of all the other specimens due to the presence of rubber pads which softened the column interfaces leading to a reduction in rotational stiffness. Previous studies showed that using rubber pads at frame joints reduced the period of vibration. Due to the quasistatic nature of the cyclic testing in this study, the effect of using rubber at joints on the period of the structure was not investigated. However, more detailed results regarding this issue may be deduced by applying a ground motion to the specimens using a shaking table. Overall, the proposed systems (excluding specimen F-FRP3-R) have the advantage of higher lateral load resistance, i.e. higher strength. One downside that was observed is the loss of initial post-tension after the end of the test. For specimen F-FRP3-S, post-tensioning bar yielding was partially attributed to the loss of the initial-post-tensioning stress. However, that was not that case for the other three specimens (F-FRP1, F-FRP3, and F-FRP-R), since the bar stresses did not overcome their yielding strength, according to strain gage readings. Two reasons are suggested: Permanent axial plastic deformation of concrete as a result of lateral dilation due to high axial stresses that the columns undergo during the test which can go up to more than double the initial post-tensioning axial compressive stress. Another reason could have been the loosening of the nut that was initially tightened to the anchorage plate after successive loading cycles. The cyclic nature of the test has several effects on the system which are suggested to be further investigated.

Also, the results of the pushover analysis for the control specimen (F-RC) and specimen F-FRP1 provided close values to the experimental load-drift results. This indicates that the response of the FRP specimens may be anticipated using the parameters discussed in Chapter 6.

7.2.2 Damage and residual drift

The conventional monolithic reinforced concrete frame (specimen F-RC) suffered the highest overall damage which was concentrated in its major structural members (the columns and the beam). Plastic hinges formed, as expected, at the four corners of the frame, and damage was highest at those locations. One steel reinforcement rebar fractured at later stages of the test. The high degree of damage suggests the high difficulty or even impossibility of repair of the structural member, which can be disastrous in actual bridges.

All the other specimens, which were mainly based on the proposed system of unbonded post-tensioned precast structural members, suffered much lower damage and residual drift when compared to the monolithic specimen (specimen F-RC). The re-centering mechanism proved to be effective in the proposed systems. Damage was limited to local FRP tube locations due to interlocking while rotating, which does not affect the performance of the confined concrete column segment. This problem can be simply resolved by using FRP tubes that are little shorter than the column segments to prevent any interaction of two adjacent tubes while the column-segments are rotating.

Except for specimen F-FRP3-S, none of the post-tensioning steel bars yielded due to the carefully selected initial post-tensioning stress. The maximum post-tensioning steel bar stress

was close to the predicted values, which were designed not to exceed 60% of the ultimate strength of the bar. The attachment of the modified steel angles to specimen F-FRP-S led to higher lateral stiffness of the frame and caused the post-tensioning bar to undergo higher stresses than in the other specimens at similar drifts. Therefore, the effect of attaching energy dissipating devices must be accounted for while analyzing the frame to better predict the maximum stresses at the steel bars and other locations. Specimen F-FRP3-R was almost free from any kind of damage due to the presence of rubber pads which prevented the FRP tubes from interacting at interlocking interfaces while rotating, and also provided a buffer zone preventing significant increase in bar stresses.

7.2.3 Energy dissipation

Conventional monolithic reinforced concrete frames dissipate most of the input seismic energy applied to them via permanent damage and deformation in the form of reinforcement yielding as well as concrete crushing, leading to the formation of plastic hinges. As expected, the monolithic frame (specimen F-RC) exhibited higher energy dissipation than the post-tensioned system whether the columns of the frame were of a single segment (as with specimen F-FRP) or with multiple specimens (F-FRP3). To overcome this challenge, energy dissipation mechanisms were developed. The main criterion was to attach additional parts to the frame that can dissipate more energy through permanent deformation while being easily replaced after damage. This was implemented by attaching modified steel angles. Previous research showed that adding such angles to the frame can absorb some energy, but cease to perform efficiently after certain drifts due to the relatively small part of the angle undergoing permanent deformation (i.e. local yielding at the corner of the steel angle). The steel angle was therefore modified to improve its

energy dissipation. As expected, the specimen with the modified steel angles (specimen F-FRP-S) dissipated more energy than all the other proposed post-tensioned specimens and overcame the magnitude of energy dissipation of the conventional monolithic frame (specimen F-RC) as well, which is one important goal of this study.

Specimen F-FRP3-R showed the lowest energy dissipation, proving that the use of rubber pads does not offer a good energy dissipation alternative.

7.3 Overall performance

The goal of this research was achieved: a better proposed system sharing similar geometric, dimensional, and concrete properties with a conventional monolithic bridge moment resisting frame was created. The proposed system has the advantages of:

- higher strength in terms of lateral load resistance
- lower damage post lateral loading
- easier repair post lateral loading
- faster, easier, and cleaner construction

The proposed system offers a feasible and efficient alternative to the conventional reinforced concrete system. The loss of post-tension however still poses a significant problem that has to be addressed, since it can affect a key property of the proposed system - re-centering - and hinder its effect. One improvement to that would be bonding the nut which is tightened to the anchorage plate with the post-tensioning bar (such as by the use of adhesives or by welding). Further research is recommended regarding this issue.

7.4 Recommendations for future studies

The stress-strain model used for the FRP confined concrete in this study did not account for the cyclic nature of the test. Future research may include models that include unloading pathways of stress-strain relationships of FRP confined concrete columns. These can then be incorporated to find better predictions of the moment-curvature relationships, which are key values to finding the design initial post-tension. Accurately predicting the initial post-tension is important also so that design values can prevent the post-tensioning bars/tendons from yielding and hence, preventing permanent damage as well as re-centering the bridges more efficiently.

The sources of loss of post-tension may be further investigated since loss of post tension poses a serious threat to the performance of the bridge columns after a seismic event, and could be cumbersome to resolve. Loss of post-tension may prevent re-centering, which is one of the key goals of using the proposed system.

Also, designing more efficient energy dissipation devices can be an advantageous topic for future research. The modified steel angles used in this study as energy dissipation mechanisms were based on simple design criteria: a tension member was added to the steel angle with a "fuse" section where damage can be directed to and concentrated while having better efficiency than unmodified steel angles. Incorporating both modified steel angles and rubber pads can also be studied since rubber pads offer buffer zones and may therefore better control the specimen's overall stresses as well as limit the degree of local damage at locations where the steel angles are anchored.

References

M.J.N. Priestley, G.M. Calvi, M.J. Kowalsky, “Displacement-based seismic design of structures:, IUSS Press, Pavia, Italy, 2007

Chung-Che Chou, Yu-Chih Chen, "Cyclic tests of post-tensioned precast CFT segmental bridge columns with unbonded strands", Earthquake Engineering and Structural Dynamics, 35:159–175, 2006.

Junichi Sakai, Hyungil Jeong, Stephen A. Mahin, “Reinforced concrete bridge columns that re-center following earthquakes”, Proceedings of the 8th U.S. National Conference on Earthquake Engineering April 18-22, 2006, San Francisco, California, USA, Paper No. 1421

Building Code Requirements for Structural Concrete (ACI 318-05) and Commentary, American Concrete Institute, 2005.

Carlos Andres Blandon, M. J. N. Priestley, “Equivalent viscous damping equations for direct displacement based design”**,** Journal of Earthquake Engineering Vol. 9, Special Issue 2 (2005) 257–278

David G. Hieber, Jonathan M. Wacker, Marc O. Eberhard, John F. Stanton. "State-of-the-Art Report on Precast Concrete Systems for Rapid Construction of Bridges", Washington State Transportation Center (TRAC), University of Washington, 2005.

David G. Hieber, Jonathan M. Wacker, Marc O. Eberhard, John F. Stanton, " Precast Concrete Pier Systems for Rapid Construction of Bridges in Seismic Regions", Washington State Transportation Center (TRAC) ,University of Washington, 2005.

Yu-Chen Ou, Methee Chiewanichakorn, Il-Sang Ahn, Amjad J. Aref, Stuart S. Chen, Andre Filiatrault, George C. Lee, "Cyclic Performance of Precast Concrete Segmental Bridge Columns", University at Buffalo, State University of New York, 2005.

L.P Ye, K. Zhang, S.H. Zhao, P.Feng. “Experimental study on seismic strengthening of RC columns with wrapped CFRP sheets”. Elsevier, Construction and Building Materials 17 (2003) 499-506.

Joshua T. Hewes, M.J. Nigel Priestly, "Seismic Dsesign and Performance of Precast Concrete Segmental Bridge Columns", University of California, San Diego, 2002.

NIST Workshop on Standards Development for the Use of Fiber Reinforced Polymers for the Rehabilitation of Concrete and Masonry Structures, January 7-8, 1998, Tucson, Arizona.

Michel Samaan, Amir Mirmiran, Mohsen Shahawy. “Model of Concrete confined by fiber composites”. Journal of Structural Engineering / September 1998, p. 1025-1031.

John B. Mander, Chin-Tung Cheng. "Seismic Resistance of Bridge Piers Based on Damage Avoidance Design", NCEER-97-0014, 1997.

M. J. N. Priestley, g. M. Calvi, "Seismic design and retrofit of bridges", John Wiley & Sons, Inc., 1996.

Mander, M. J., Priestley, M. J. & Park, R. (1988, August). Theoretical Stress-Strain Model for Confined Concrete. *Journal of Structural Engineering , 114* (8).

Note:
Some material tests (discussed in Chapter 3) were performed in collaboration with Dawood, Haitham who was preparing a thesis with a preliminary title of "Numerical modeling of self-centering concrete bridge piers and bents under seismic loads", but was not complete at the time of completing this thesis.

Appendix A

XTRACT Analysis Results

XTRACT Analysis Report - Educational

Washington State University

For use only in an academic or research setting.

Section Name: Section1

Loading Name: L0y

Analysis Type: Moment Curvature

Section Details:

X Centroid:	-.2401E-15 in
Y Centroid:	-.6323E-16 in
Section Area:	88.49 in^2

Loading Details:

Incrementing Loads:	MyyOnly
Number of Points:	31
Analysis Strategy:	Displacement Control

Analysis Results:

Failing Material:	Confined1
Failure Strain:	20.00E-3 Compression
Curvature at Initial Load:	0 1/in
Curvature at First Yield:	.4763E-3 1/in
Ultimate Curvature:	11.57E-3 1/in
Moment at First Yield:	83.61 kip-in
Ultimate Moment:	124.0 kip-in
Centroid Strain at Yield:	.7714E-3 Ten
Centroid Strain at Ultimate:	18.47E-3 Ten
N.A. at First Yield:	1.620 in
N.A. at Ultimate:	1.597 in
Energy per Length:	1.322 kips
Effective Yield Curvature:	.6350E-3 1/in
Effective Yield Moment:	111.5 kip-in
Over Strength Factor:	1.112
EI Effective:	175.5E+3 kip-in^2
Yield EI Effective:	1144 kip-in^2
Bilinear Herding Slope:	.6514 %
Curvature Ductility:	18.22

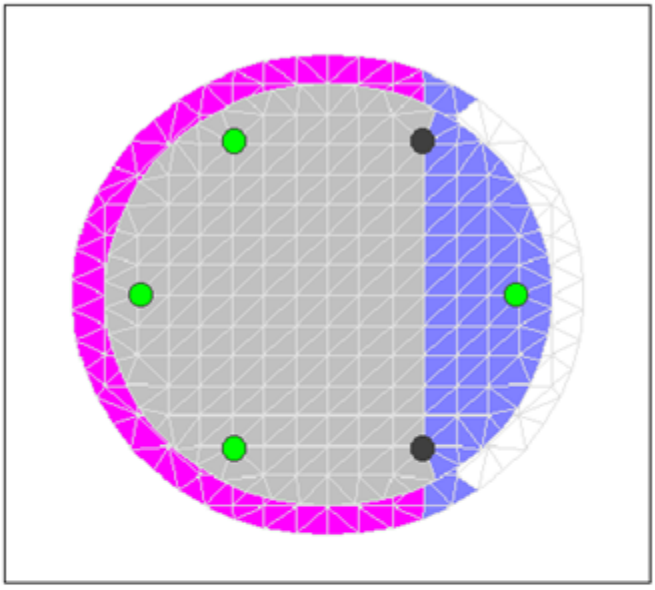

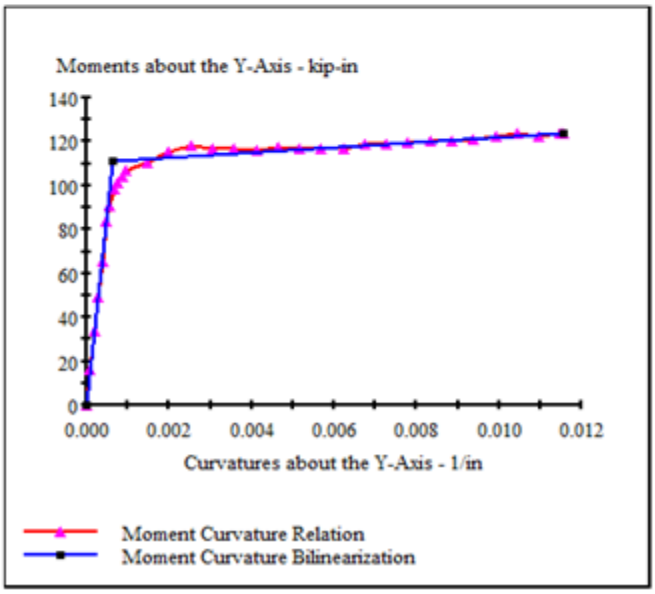

Appendix B

FRP Strain

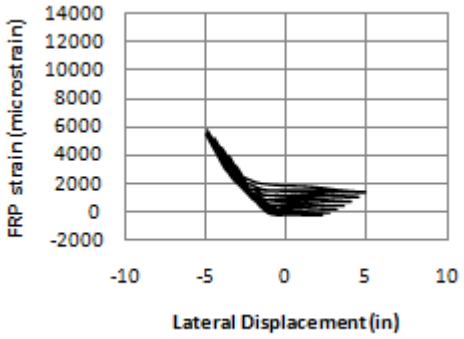

(a): Gage C1

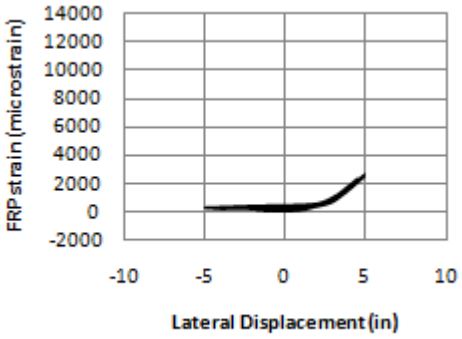

(b): Gage C2

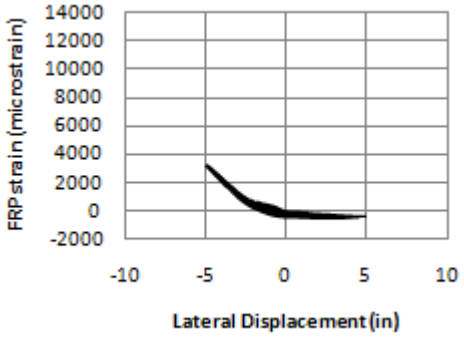

(c): Gage C3

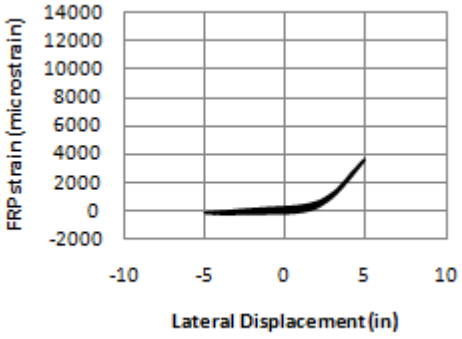

(d): Gage C4

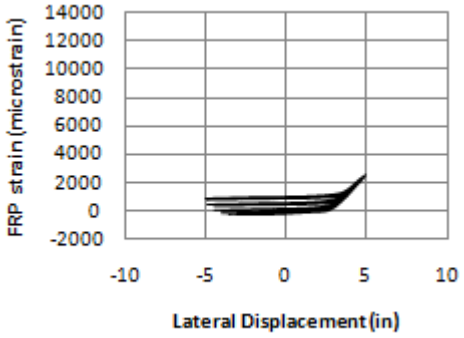

(e): Gage C5

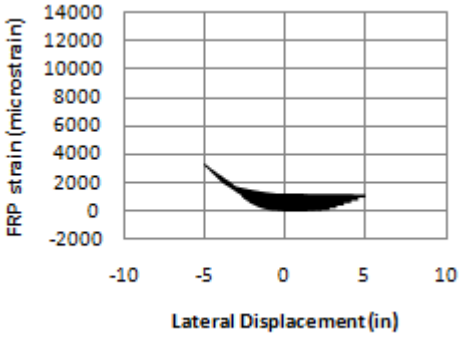

(f): Gage C6

Figure B.1: North column of Specimen F-FRP1 circumferential strain

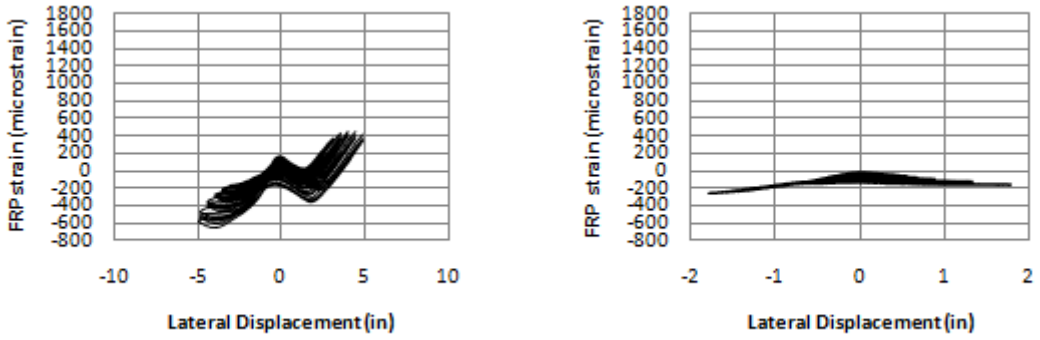

(a): Gage L1 (b): Gage L2

Figure B.2: North column of Specimen F-FRP1 longitudinal strain

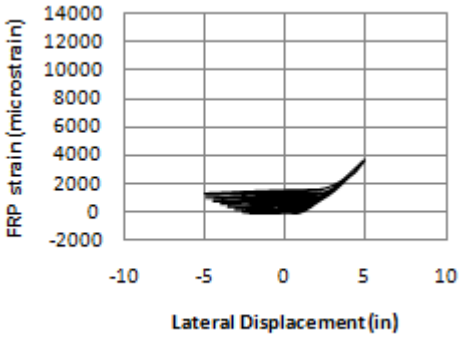

(a): Gage C8

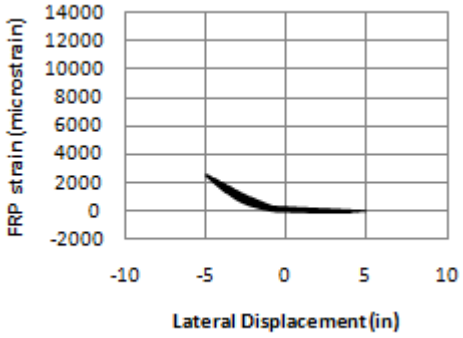

(b): Gage C9

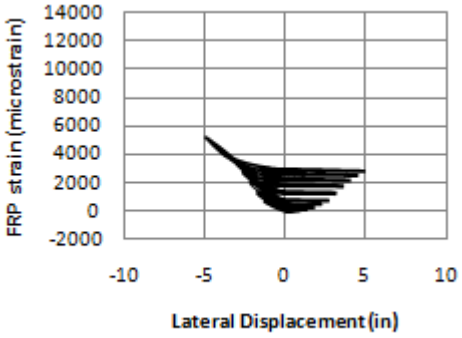

(c): Gage C10

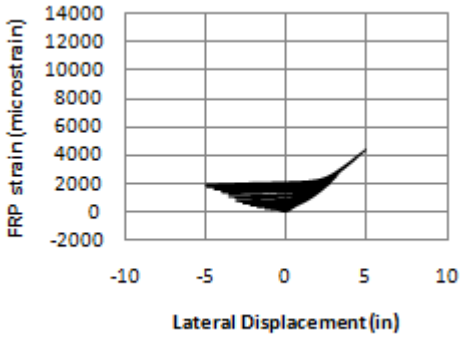

(d): Gage C11

Figure B.3: South column of Specimen F-FRP1 circumferential strain

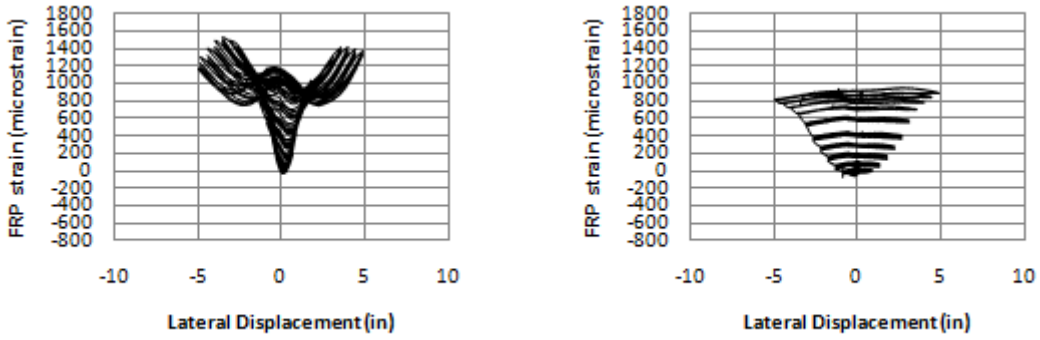

(a): Gage L3 (b): Gage L4

Figure B.4: South column of Specimen F-FRP1 longitudinal strain

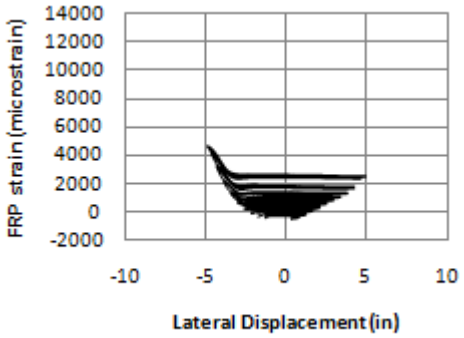

(a): Gage C1

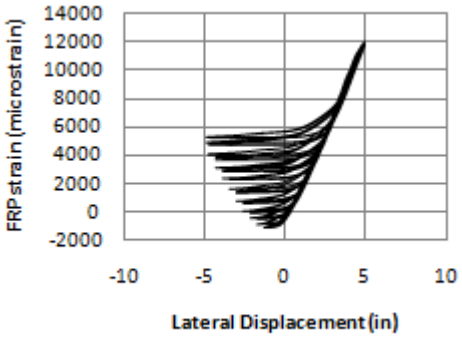

(b): Gage C2

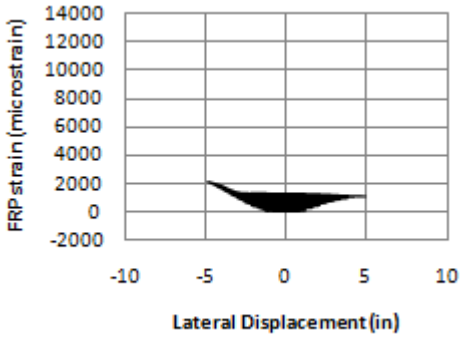

(c): Gage C3

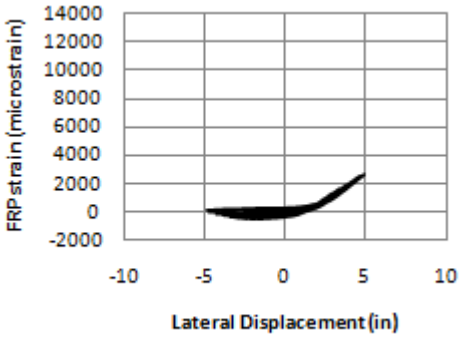

(d): Gage C4

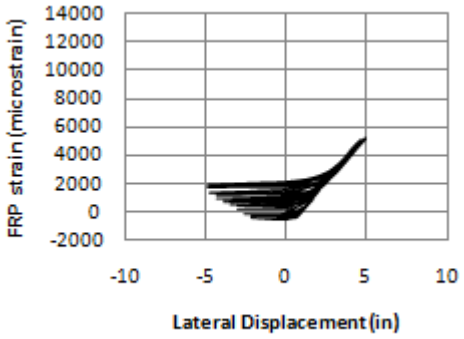

(e): Gage C5

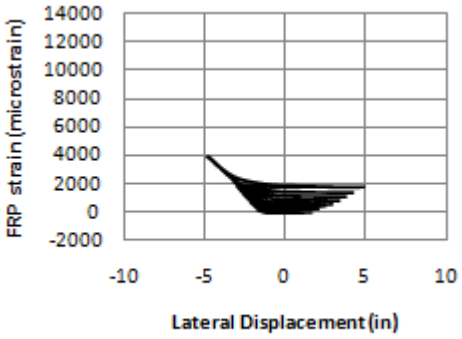

(f): Gage C6

Figure B.5: North column of Specimen F-FRP3 circumferential strain

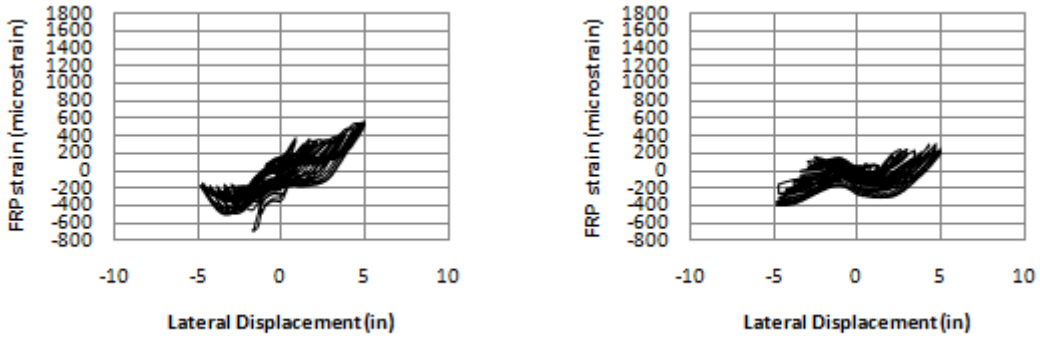

(a): Gage L1 (b): Gage L2

Figure B.6: North column of Specimen F-FRP3 longitudinal strain

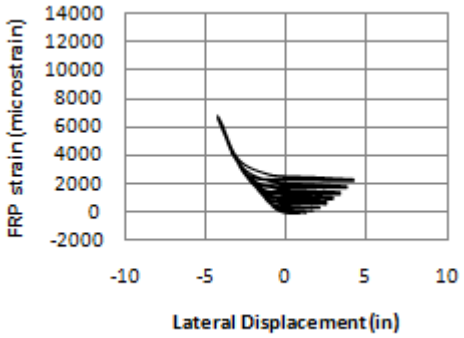

(a): Gage C7

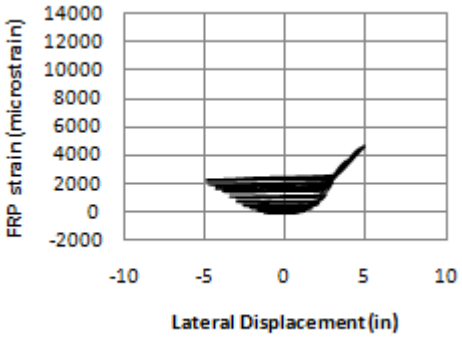

(b): Gage C8

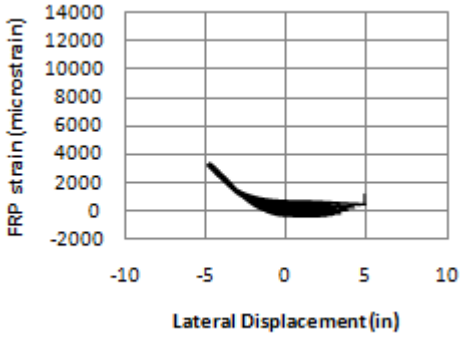

(c): Gage C9

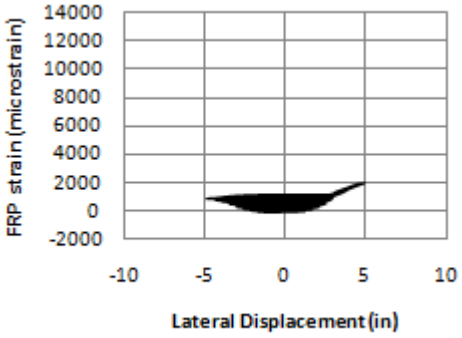

(d): Gage C10

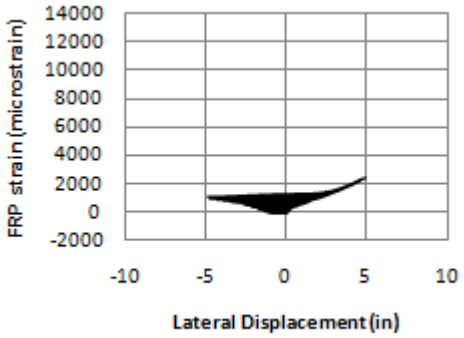

(e): Gage C11

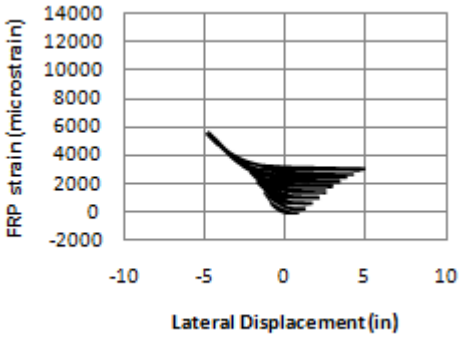

(f): Gage C12

Figure B.7: South column of Specimen F-FRP3 circumferential strain

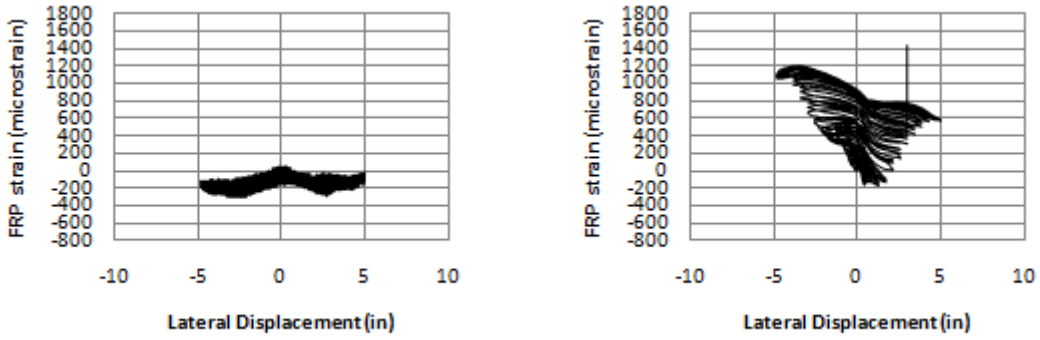

(a): Gage L3 (b): Gage L4

Figure B.8: South column of Specimen F-FRP3 longitudinal strain

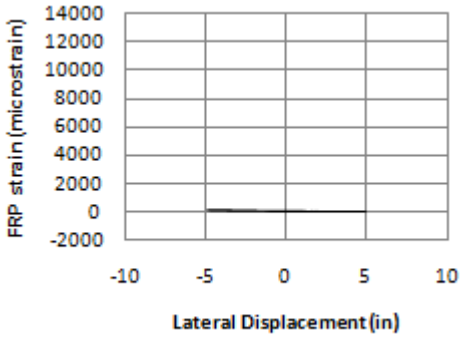

(a): Gage C1

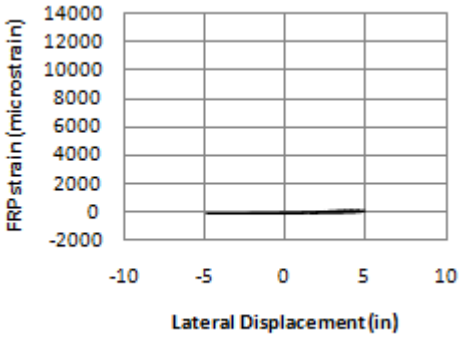

(b): Gage C2

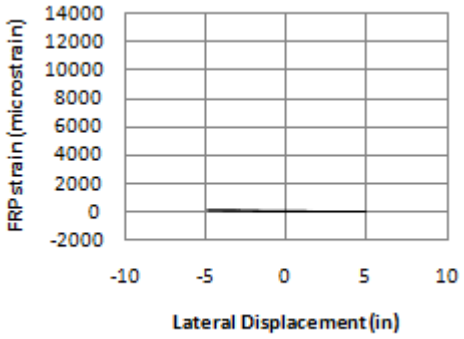

(c): Gage C3

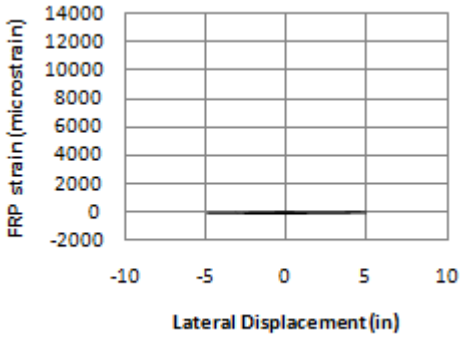

(d): Gage C5

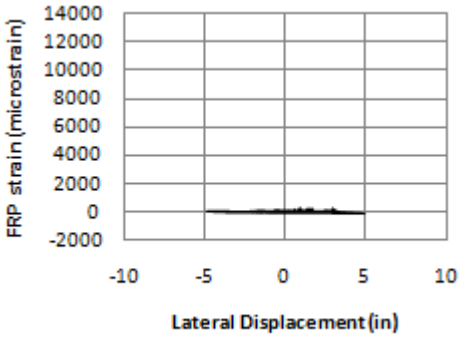

(e): Gage C6

Figure B.9: North column of Specimen F-FRP3-R circumferential strain

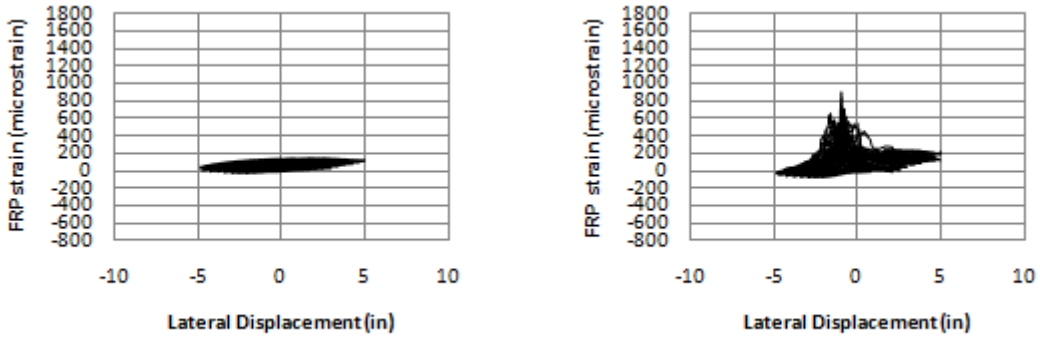

(a): Gage L1 (b): Gage L2

Figure B.10: North column of Specimen F-FRP3-R longitudinal strain

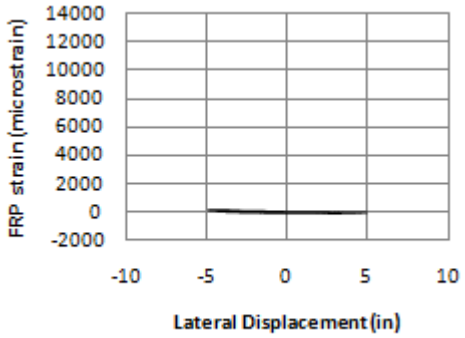

(a): Gage C9

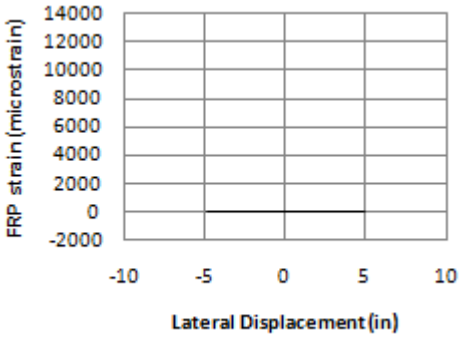

(b): Gage C10

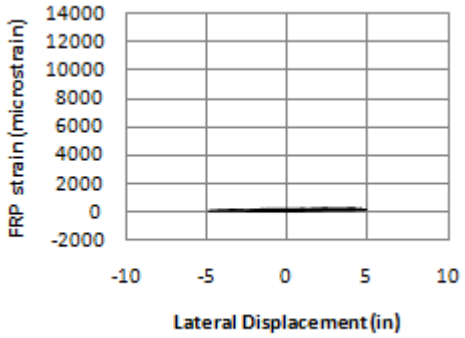

(c): Gage C11

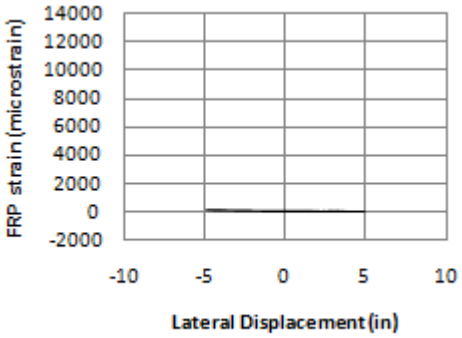

(d): Gage C12

Figure B.11: South column of Specimen F-FRP3-R circumferential strain

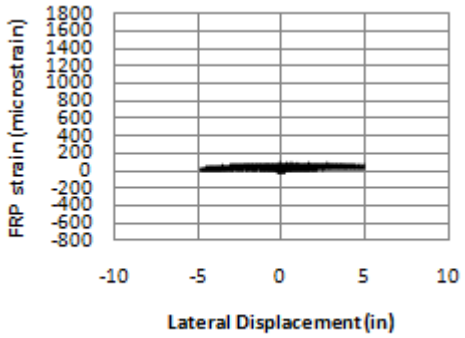

(a): Gage L3

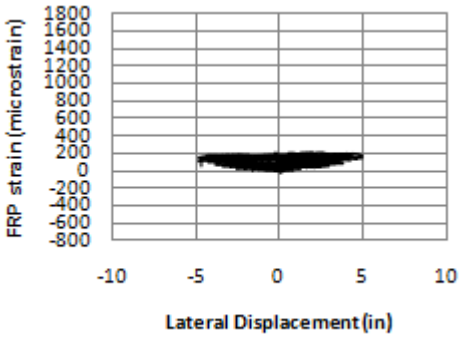

(b): Gage L4

Figure B.12: South column of Specimen F-FRP3-R longitudinal strain

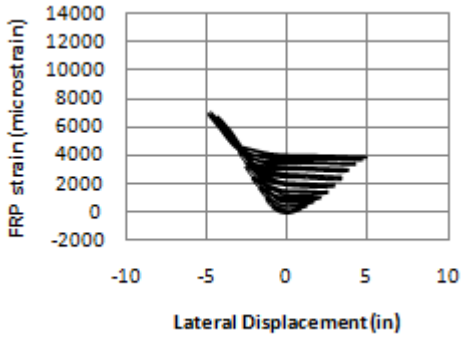

(a): Gage C1

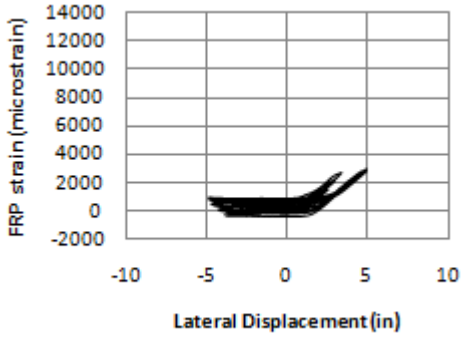

(b): Gage C5

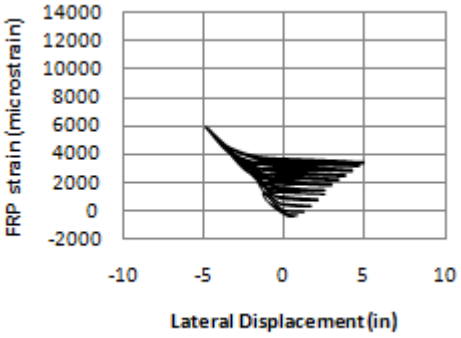

(c): Gage C6

Figure B.13: North column of Specimen F-FRP3-S circumferential strain

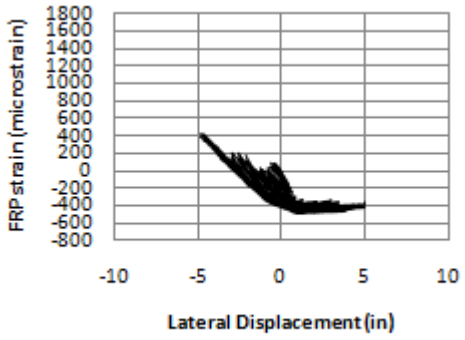

(a): Gage L1

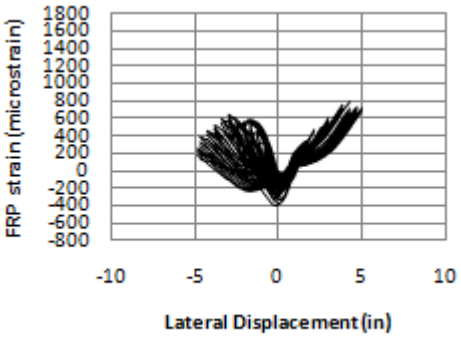

(b): Gage L2

Figure B.14: North column of Specimen F-FRP3-S longitudinal strain

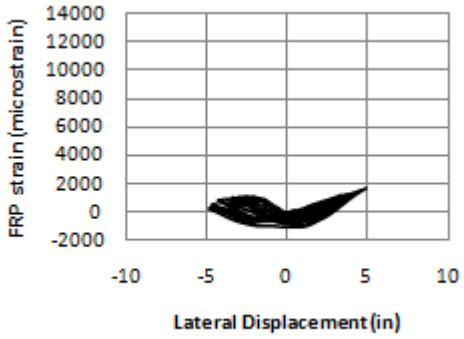

(a): Gage C10

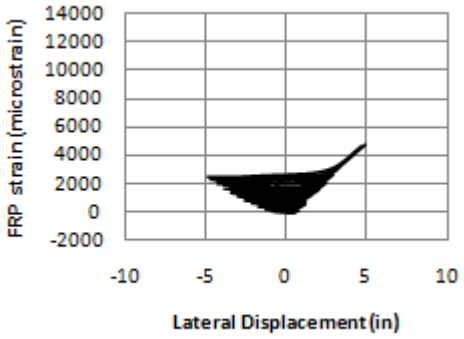

(b): Gage C11

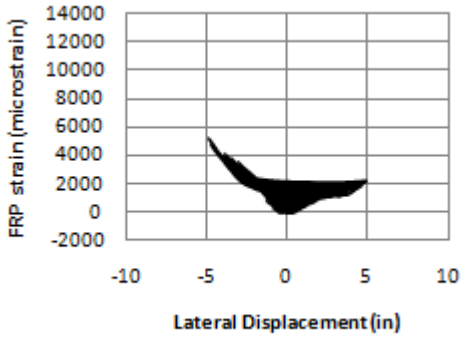

(c): Gage C12

Figure B.15: South column of Specimen F-FRP3-S circumferential strain

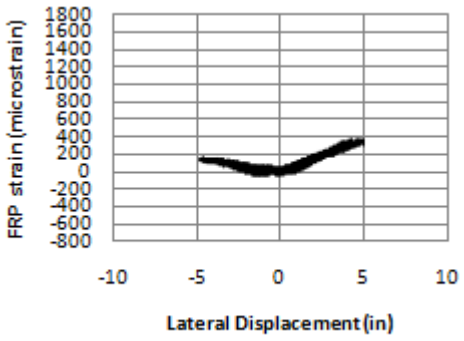

(a): Gage L3

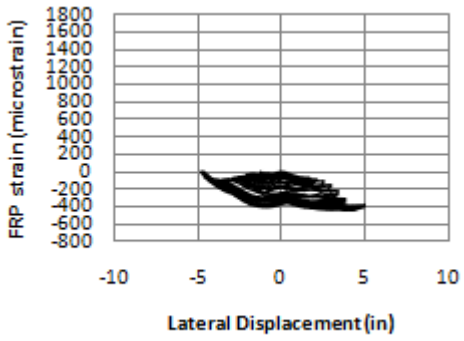

(b): Gage L4

Figure B.16: South column of Specimen F-FRP3-S longitudinal strain

Appendix C

Moment-Curvature Analysis for FRP Column

$fc := 13.79$

$tj := \left(\frac{1}{8}\right)\cdot 25.4 = 3.175$

$D := 203.2$

$Ej := 2008\cdot 6.895 = 1.385 \times 10^{4}$

$n := 1.5$

$fj := 9.2\cdot 6.895 = 63.434$

$fr := 2\cdot fj\cdot\frac{tj}{D}$

$f0 := 0.872\cdot fc + 0.371\cdot fr + 6.258$

$E1 := 1975\cdot 6.895$

$E2 := 245.61\cdot fc^{0.2} + 1.3456\cdot Ej\cdot\frac{tj}{D}$

$$fc1(\varepsilon c) := \left[\frac{(E1 - E2)\cdot\varepsilon c}{\left[1 + \left[(E1 - E2)\cdot\frac{\varepsilon c}{f0}\right]^{n}\right]^{\frac{1}{n}}}\right] + E2\cdot\varepsilon c$$

$fcu := fc + 6\cdot fr^{0.7}$

$\varepsilon cu := \frac{fcu - f0}{E2}$

$\mu max := -0.977\cdot\ln\left(\frac{2\cdot Ej\cdot tj}{fc\cdot D}\right) + 3.938 = 0.571$

$\mu u := -0.187\cdot\ln\left(\frac{2\cdot Ej\cdot tj}{fc\cdot D}\right) + .881 = 0.237$

$D := 203.2$

$fc := 2 \cdot 6.89475728 = 13.79$

$fu := 150 \cdot 6.895 = 1.034 \times 10^{3}$

$As := 806.45$

$Esteel := 29700 \cdot 6.89475728$

initial post-tensioning strain:

$pt0n := 945.367 \cdot 10^{-6}$ $\quad$ $pt0s := 918.6583 \cdot 10^{-6}$

$$\alpha := \frac{\frac{pt0n + pt0s}{2} \cdot Esteel}{fu} = 0.185$$

$Ps := \alpha \cdot fu \cdot As$

$$Ac := \left(\frac{\pi}{4}\right) \cdot D^{2}$$

$R := 0 \quad kN$

Stage 1:

$$x := \frac{0D}{10}$$

$$\varepsilon 2 := .000779$$

$$\varepsilon 1(y) := \frac{\varepsilon 2 \cdot \left[\left(\frac{D}{2}\right) - x + y\right]}{D - x}$$

$$\varepsilon 1\left(\frac{-D}{2} + x\right) = 0$$

$$C := \int_{-\left[\left(\frac{D}{2}\right)-x\right]}^{\frac{D}{2}} fc1(\varepsilon 1(y)) \cdot 2 \cdot \sqrt{\left(\frac{D^2}{4}\right) - y^2}\, dy$$

$$ybar := \frac{\displaystyle\int_{-\left[\left(\frac{D}{2}\right)-x\right]}^{\frac{D}{2}} fc1(\varepsilon 1(y)) \cdot \left(y - x + \frac{D}{2}\right) \cdot 2 \cdot \sqrt{\left(\frac{D^2}{4}\right) - y^2}\, dy}{\displaystyle\int_{-\left[\left(\frac{D}{2}\right)-x\right]}^{\frac{D}{2}} fc1(\varepsilon 1(y)) \cdot 2 \cdot \sqrt{\left(\frac{D^2}{4}\right) - y^2}\, dy}$$

$C = 1.539 \times 10^5$ $\qquad$ $Ps + R \cdot 1000 = 1.539 \times 10^5$

$$ybar + x - \frac{D}{2} = 23.198221$$

$$\frac{C}{fu \cdot As} = 0.1846$$

$M1 := C \cdot \left(ybar + x - \frac{D}{2} \right)$ $M1 = 3.570889 \times 10^{6}\ N - mm$

$\varepsilon 1\left(\frac{D}{2}\right) = 7.79 \times 10^{-4}$ $fc1\left(\varepsilon 1\left(\frac{D}{2}\right)\right) = 8.647$ MPa

$\phi 1 := \frac{\varepsilon 1\left(\frac{D}{2}\right)}{D - x}$ $\phi 1 = 3.833661 \times 10^{-6}\ mm^{-1}$

Stage 2:

$x := \frac{5D}{10}$

$\varepsilon 2 := .00245$

$\varepsilon 1(y) := \frac{\varepsilon 2 \cdot \left[\left(\frac{D}{2}\right) - x + y\right]}{D - x}$

$\varepsilon 1\left(\frac{-D}{2} + x\right) = 0$

$C := \int_{-\left[\left(\frac{D}{2}\right)-x\right]}^{\frac{D}{2}} fc1(\varepsilon 1(y)) \cdot 2 \cdot \sqrt{\left(\frac{D^2}{4}\right) - y^2}\, dy$

$$ybar := \frac{\int_{-\left[\left(\frac{D}{2}\right)-x\right]}^{\frac{D}{2}} fc1(\varepsilon 1(y))\cdot\left(y - x + \frac{D}{2}\right)\cdot 2\cdot\sqrt{\left(\frac{D^2}{4}\right) - y^2}\, dy}{\int_{-\left[\left(\frac{D}{2}\right)-x\right]}^{\frac{D}{2}} fc1(\varepsilon 1(y))\cdot 2\cdot\sqrt{\left(\frac{D^2}{4}\right) - y^2}\, dy}$$

$C = 1.539 \times 10^5$ $\quad$ $Ps + R\cdot 1000 = 1.539 \times 10^5$

$$\frac{C}{fu\cdot As} = 0.1845$$

$$ybar + x - \frac{D}{2} = 55.654958$$

$M2 := C\cdot\left(ybar + x - \frac{D}{2}\right)$ $\quad$ $M2 = 8.565 \times 10^{(}\,N - mm$

$\varepsilon 1\left(\frac{D}{2}\right) = 2.45 \times 10^{-3}$ $\quad$ $fc1\left(\varepsilon 1\left(\frac{D}{2}\right)\right) = 16.46\ MPa$

$\phi e := \frac{\varepsilon 1\left(\frac{D}{2}\right)}{D - x}$ $\quad$ $\phi e = 2.411417 \times 10^{-}\ mm^{-1}$

Stage 3:

$Es := 29700\cdot 6.89475728$

$Ps2 := Ps$

$Lp := \frac{D}{2}$

$Lt := 2133.6$

$$x := \frac{6.247 \cdot D}{10}$$

$$c := D - x$$

$$\varepsilon 2 := \varepsilon cu = 6.313 \times 10^{-3}$$

$$\varepsilon 1(y) := \frac{\varepsilon 2 \cdot \left[\left(\frac{D}{2}\right) - x + y\right]}{D - x}$$

$$\varepsilon 1\left(\frac{-D}{2} + x\right) = 0$$

$$\phi t := \frac{\varepsilon 1\left(\frac{D}{2}\right)}{c} \qquad \phi t = 8.278 \times 10^{-5}$$

$$\phi p := \phi t - \phi e \qquad \phi p = 5.867 \times 10^{-5}$$

$$\theta p := \phi p \cdot Lp$$

$$\Delta \varepsilon s := \theta p \cdot \frac{\left(\frac{D}{2}\right) - c}{Lt} \qquad \Delta \varepsilon s = 7.079 \times 10^{-5}$$

$$\Delta fs := \Delta \varepsilon s \cdot Es \qquad \Delta fs = 14.496$$

$$\Delta Ps := \Delta fs \cdot As \qquad \Delta Ps = 1.169 \times 10^{4}$$

$$Ps := Ps2 + \Delta Ps \qquad Ps = 1.656 \times 10^{5}$$

$$C := \int_{-\left[\left(\frac{D}{2}\right) - x\right]}^{\frac{D}{2}} fc1(\varepsilon 1(y)) \cdot 2 \cdot \sqrt{\left(\frac{D^2}{4}\right) - y^2}\, dy$$

$$ybar := \frac{\int_{-\left[\left(\frac{D}{2}\right)-x\right]}^{\frac{D}{2}} fc1(\varepsilon1(y))\cdot\left[y+\left(\frac{D}{2}\right)-x\right]\cdot 2\cdot\sqrt{\left(\frac{D^2}{4}\right)-y^2}\,dy}{\int_{-\left[\left(\frac{D}{2}\right)-x\right]}^{\frac{D}{2}} fc1(\varepsilon1(y))\cdot 2\cdot\sqrt{\left(\frac{D^2}{4}\right)-y^2}\,dy}$$

$C = 1.656 \times 10^5$ $\quad$ $Ps + R\cdot 1000 = 1.656 \times 10^5$

$$\frac{Ps}{fu\cdot As} = 0.199$$

$ybar = 38.787$

$$ybar + x - \frac{D}{2} = 64.126$$

$$M1 := C\cdot\left(ybar + x - \frac{D}{2}\right) \qquad M1 = 1.062 \times 10^7$$

$$\varepsilon1\left(\frac{D}{2}\right) = 6.313 \times 10^{-3} \qquad fc1\left(\varepsilon1\left(\frac{D}{2}\right)\right) = 22.17$$

$$\phi := \frac{\varepsilon1\left(\frac{D}{2}\right)}{D - x} \qquad \phi = 8.278242 \times 10^{-5}$$

Appendix D

MATLAB M-Files for Analyses

M-File 1: Hysteresis, Energy and Viscous Damping Calculations

```
clear all
clc
a=xlsread('demo data.xls');
b=size(a(:,1));
c=0;
d=0;
e=0;

% loop for finding the max disp and loads of each load cycle.
for i=1:b-2
    if a(i,2) < 0
       % i.e. if under x axis
        if a(i+1,1) == a(i,1) && a(i,1)< a(i-1,1)
            % in case there are redundant displacements
            f=i;
            while a(f,1)== a(i,1)
                if f+1<b(1)
                    f=f+1;
                end
                if f+1==b(1)
                    f=b(1);
                    break
                end
            end
            if a(f,1)>a(i,1)
                c=c+1;
                neg(c)=i;
            end
        end

        if a(i+1,1) < a(i,1)
            if a(i+2,1) > a(i+1,1)
                c=c+1;
                neg(c)=i;
            end
        end
    end

    if a(i,2) > 0                   % i.e. if above x axis

        if a(i+1,1) == a(i,1) && a(i,1)> a(i-1,1)
            f=i;
            while a(f,1)== a(i,1)
                f=f+1;
```

```
            end
            if a(f,1) < a(i,1)
                d=d+1;
                pos(d)=i;
            end
        end

        if a(i+1,1) > a(i,1)
            if a(i+2,1) < a(i+1,1)
                d=d+1;
                pos(d)=i;
            end
        end
    end
end

%% loop for finding the begining of each load cycle
for i=1:b-1
    if a(i+1,1).*a(i,1) <= 0 && a(i+1,1)<a(i,1) && a(i+1)<0
        e=e+1;
        g(e)=i;
    end
end

%loop for finding locations of given zero-diplacemnts
j=1;
for i=1:b(1)
    if a(i,1)==0
        zerodisp(j)=i;
        j=j+1;
    end
end



% interploating zeroload displacements
h=1;

for i=1:b(1)-1

    if a(i,2).*a(i+1,2)>=0
        aa(h,1)=a(i,1);
        aa(h,2)=a(i,2);
        h=h+1;
    end

    if a(i,2).*a(i+1,2)<0
        aa(h,1)=a(i,1);
        aa(h,2)=a(i,2);
        q=a(i,2).*(a(i+1,1)-a(i,1))./(a(i+1,2)-a(i,2));
        aa(h+1,1)=a(i,1)-q;
        aa(h+1,2)=0;
        h=h+2;
    end
end
```

```
%%loop for calculating absorbed energy for each load cycle (i.e area under
%%graph)

% first, find when load is zero (depending on actual and/or interpolated
% zero-load values

r=1;

for i=1:b(1)
    if aa(i,2)==0
        zeroload(r)=i;
        r=r+1;
    end
end

% to find energy abosrbed, calculate area under graph between the elements of
"zeroload"
s=size(zeroload);
for i=1:s(2)-1

    area1(i)=0;
    for j=zeroload(i):zeroload(i+1)
        area2(j)=0.5.*(aa(j,2)+aa(j+1,2)).*(aa(j+1,1)-aa(j,1));
        area1(i)=area1(i)+area2(j);
    end
end


%%loops for preparing the x and y values for a plot of energy vs drift (first
cycle of each disp level)
% loop for disp-level (cycle 1 of each 3)

% The following loops are for "negative displacements" then "positive
% displacements" respectively.

counter1=1;
for i=1:3:c
    displevelneg1(counter1)=a(neg(i)+1,1);
    peakloadneg1(counter1)=a(neg(i)+1,2);
    %these values will be used in EVD calculations
    counter1=counter1+1;
end




counter1pos=1;
for i=1:3:d
    displevelpos1(counter1pos)=a(pos(i)+1,1);
```

```
    peakloadpos1(counter1pos)=a(pos(i)+1,2);
    counter1pos=counter1pos+1;
end
%}

% loop for energy absorbed corresponding to each of displevel1

s2=size(area1);
counter2=1;
for i=1:6:s2(2)
    energyneg1(counter2)=area1(i);
    counter2=counter2+1;
end



%
counter2pos=1;
for i=2:6:s2(2)
    energypos1(counter2pos)=area1(i);
    counter2pos=counter2pos+1;
end
%}


%Now we can calculate Equivalent Viscous Damping (EVD) for each disp level1

for i=1:counter1-1
    EVD1(i)=energyneg1(i)./(2.*pi.*peakloadneg1(i).*displevelneg1(i));
    EVDpos1(i)=energypos1(i)./(2.*pi.*peakloadpos1(i).*displevelpos1(i));
end




% loop for calculating cumulative energy for energy in negative then
% positive direction respectively
% cycle one of each three
s3=size(energyneg1);
cumenergyneg1(1)=energyneg1(1);

for i=1:s3(2)-1
    cumenergyneg1(i+1)=cumenergyneg1(i)+energyneg1(i+1);
end



%
s3pos=size(energypos1);
cumenergypos1(1)=energypos1(1);
for i=1:s3pos(2)-1
    cumenergypos1(i+1)=cumenergypos1(i)+energypos1(i+1);
end
%}
```

```
% loop for disp-level (cycle 2 of each 3)

counter3=1;
for i=2:3:c
    displevelneg2(counter3)=a(neg(i)+1,1);
    peakloadneg2(counter3)=a(neg(i)+1,2);
    counter3=counter3+1;
end


%
counter3pos=1;
for i=2:3:d
    displevelpos2(counter3pos)=a(pos(i)+1,1);
    peakloadpos2(counter3pos)=a(pos(i)+1,2);
    counter3pos=counter3pos+1;
end
%}

% loop for energy absorbed corresponding to each displevelneg2

counter4=1;
% the area undergraph i.e. energy abosrbed correspomding to the 2nd cycle
% in negative disp. level is area 3 then 9,...,etc
for i=3:6:s2(2)
    energyneg2(counter4)=area1(i);
    counter4=counter4+1;
end


% loop for energy absorbed corresponding to each displevelpos2

counter4pos=1;
for i=4:6:s2(2)
    energypos2(counter4pos)=area1(i);
    counter4pos=counter4pos+1;
end


%loop for calculating EVD2
for i=1:counter3-1
    EVD2(i)=energyneg2(i)./(2.*pi.*peakloadneg2(i).*displevelneg2(i));
end


%loop for EVDpos2

for i=1:counter3pos-1
    EVDpos2(i)=energypos2(i)./(2.*pi.*peakloadpos2(i).*displevelpos2(i));
end
```

```
% loop for calculating cumulative energy for energy in negative and pos
% direction respectivley, cycle two of each three

s3=size(energyneg2);
cumenergyneg2(1)=energyneg2(1);
for i=1:s3(2)-1
    cumenergyneg2(i+1)=cumenergyneg2(i)+energyneg2(i+1);
end

s3pos=size(energypos2);
cumenergypos2(1)=energypos2(1);
for i=1:s3pos(2)-1
    cumenergypos2(i+1)=cumenergypos2(i)+energypos2(i+1);
end


% loop for disp-level 3 (cycle 3 of each 3)
counter5=1;
for i=3:3:c
    displevelneg3(counter5)=a(neg(i)+1,1);
    peakloadneg3(counter5)=a(neg(i)+1,2);
    counter5=counter5+1;
end

counter5pos=1;
for i=3:3:d
    displevelpos3(counter5pos)=a(pos(i)+1,1);
    peakloadpos3(counter5pos)=a(pos(i)+1,2);
    counter5pos=counter5pos+1;
end


% loop for energy absorbed corresponding to each displevel2 (neg then pos)
% the area undergraph i.e. energy abosrbed correspomding to the 3rd cycle
% in negative disp. level is area 5 then 11,...,etc
counter6=1;
for i=5:6:s2(2)
    energyneg3(counter6)=area1(i);
    counter6=counter6+1;
end

counter6pos=1;
for i=6:6:s2(2)
    energypos3(counter6pos)=area1(i);
    counter6pos=counter6pos+1;
end



%loop for calculating EVD3
for i=1:counter5-1
    EVD3(i)=energyneg3(i)./(2.*pi.*peakloadneg3(i).*displevelneg3(i));
end
```

```
for i=1:counter5pos-2
    %(because last loop is not complete - does not return to zero)
    EVDpos3(i)=energypos3(i)./(2.*pi.*peakloadpos3(i).*displevelpos3(i));
end


% loop for calculating cumulative energy for energy in negative direction
% cycle three of each three
s3=size(energyneg3);
cumenergyneg3(1)=energyneg3(1);
for i=1:s3(2)-1
    cumenergyneg3(i+1)=cumenergyneg3(i)+energyneg3(i+1);
end

s3=size(energypos3);
cumenergypos3(1)=energypos3(1);
for i=1:s3(2)-1
    cumenergypos3(i+1)=cumenergypos3(i)+energypos3(i+1);
end


figure(1)
plot(abs(displevelneg1)./0.525,energyneg1,'b--')
hold on
plot(abs(displevelneg2)./0.525,energyneg2,'r--')
plot(abs(displevelneg3)./0.525,energyneg3,'g--')
plot(displevelpos1./0.525,energypos1,'b')
plot(displevelpos2./0.525,energypos2,'r')
plot(displevelpos3(1:16)./0.525,energypos3,'g')
legend('energyneg1','energyneg2','energyneg3','energypos1','energypos2','ener
gypos3')
xlabel('Drift (%)')
ylabel('Abosrbed Energy (lb.in)')
title('Lateral drift vs. Absorbed energy')


figure(2)
plot(abs(displevelneg1)./0.525,cumenergyneg1,'--b')
hold on
plot(abs(displevelneg2)./0.525,cumenergyneg2,'--r')
plot(abs(displevelneg3)./0.525,cumenergyneg3,'--g')
plot(displevelpos1./0.525,cumenergypos1,'b')
plot(displevelpos2./0.525,cumenergypos2,'r')
plot(displevelpos3(1:16)./0.525,cumenergypos3,'g')
legend('cumenergyneg1','cumenergyneg2','cumenergyneg3','cumenergypos1','cumen
ergypos2','cumenergypos3')
xlabel('Drift (%)')
ylabel('Cumulative absorbed energy (lb.in)')
title('Lateral drift vs. cumulative absorbed energy')
```

```
figure(3)
plot(abs(displevelneg1)./0.525,EVD1,'--b')
hold on
plot(abs(displevelneg2)./0.525,EVD2,'--r')
plot(abs(displevelneg3)./0.525,EVD3,'--g')
plot(displevelpos1./0.525,EVDpos1,'b')
plot(displevelpos2./0.525,EVDpos2,'r')
plot(displevelpos3(1:16)./0.525,EVDpos3,'g')
legend('EVDneg1','EVDneg2','EVDneg3','EVDpos1','EVDpos2','EVDpos3')
xlabel('Drift (%)')
ylabel('EVD')
title('Lateral drift vs. EVD')

energypos3(1,17)=nan;
cumenergypos3(1,17)=nan;
EVDpos3(1,17)=nan;

energyspreadsheet=[abs(displevelneg1'),energyneg1',cumenergyneg1',EVD1',displ
evelpos1',energypos1',cumenergypos1',EVDpos1',abs(displevelneg2'),energyneg2'
,cumenergyneg1',EVD2',displevelpos2',energypos2',cumenergypos2',EVDpos2'
,abs(displevelneg3'),energyneg3',cumenergyneg3',EVD3',displevelpos3',energypo
s3',cumenergypos3',EVDpos3'];
```

M-File 2: Curvature Calculations – Part 1

```
clear all
clc
a=xlsread('rotationsdemodatanew.xls');
s1=size(a);
c1=0;
h=2;

for i=1:s1(1)
    c1=c1+1;
    curv(c1)=a(i,2)./h;
end

c1=0;
for i=1:s1(1)
    c1=c1+1;
    disp0(c1)=a(i,1);
end

c2=2;
i1=35;
i2=i1+1;
sign(1)=i1;
for i=i2:s1(1)-1
    if disp0(i+1).*disp0(i)<=0 && disp0(i).*disp0(i+2)<0
        sign(c2)=i;
        c2=c2+1;
    end
end
sign(c2)=s1(1);
c3=1;
c3neg=1;
s2=size(sign);
interval=disp0(sign(1):sign(2));
    [localmax,lml]=max(interval);
    if localmax>0.0003
        localmax1(c3,1)=lml+sign(1)-1;
        localmax1(c3,2)=localmax;
        c3=c3+1;
    end
for i=2:s2(2)-1
    intervalb4=disp0(sign(i-1):sign(i));
    [localmaxb4,lmlb4]=max(intervalb4);
    [localminb4,lminlb4]=min(intervalb4);
    interval=disp0(sign(i):sign(i+1));
    [localmax,lml]=max(interval);
    if localmax>0.0003 && localmax>localmaxb4
        localmax1(c3,1)=lml+sign(i)-1;
        localmax1(c3,2)=localmax;
        c3=c3+1;
    end
    [localmin,lminl]=min(interval);
    if localmin<-.0003 && localmin<localminb4
        localmin1(c3neg,1)=lminl+sign(i)-1;
        localmin1(c3neg,2)=localmin;
```

```
        c3neg=c3neg+1;
    end
end



s3=size(localmax1);
c4=1;
for i=1:1:s3(1)
    localmax2(c4,1)=localmax1(i,1);
    localmax2(c4,2)=localmax1(i,2);
    c4=c4+1;
end

s3neg=size(localmin1);
c4neg=1;
for i=1:1:s3neg(1)
    localmin2(c4neg,1)=localmin1(i,1);
    localmin2(c4neg,2)=localmin1(i,2);
    c4neg=c4neg+1;
end

s4=size(localmax2);
c5=1;
for i=1:s4(1)
    disp(c5)=disp0(localmax2(i,1));
    curv1(c5)=curv(localmax2(i,1));
    c5=c5+1;
end

s4neg=size(localmin2);
c5neg=1;
for i=1:s4neg(1)
    dispneg(c5neg)=a(localmin2(i,1),1);
    curv1neg(c5neg)=curv(localmin2(i,1));
    c5neg=c5neg+1;
end


M=[disp',curv1'];
Mneg=[dispneg',curv1neg'];
% xlswrite('curvature frame x joint x pos',M)
% xlswrite('curvature frame x joint x neg',Mneg)
```

M-File 3: Curvature Calculations – Part 2

```
aa=xlsread('curvdemodata.xls');
s5=size(aa);
c6=1;

for i=1:3:s5(1)
    curv2(c6,1)=(aa(i,1)+aa(i+1,1)+aa(i+2,1))./3;
    curv2(c6,2)=(aa(i,2)+aa(i+1,2)+aa(i+2,2))./3;
    c6=c6+1;
end

% xlswrite('curvature frame x joint x refined',curv2)
```